



**UNIVERSITY OF  
BIRMINGHAM**

**Development and Processing of Solid  
Oxide Fuel Cell Materials**

By

**Thomas William Pike**

Primary Supervisor: Professor Peter R. Slater

Secondary Supervisor: Professor Robert Steinberger-Wilckens

A thesis submitted to The University of Birmingham for the degree of

**Doctor of Philosophy**

Chemical Engineering

Engineering and Physical Sciences

University of Birmingham

UNIVERSITY OF  
BIRMINGHAM

**University of Birmingham Research Archive**

**e-theses repository**

This unpublished thesis/dissertation is copyright of the author and/or third parties. The intellectual property rights of the author or third parties in respect of this work are as defined by The Copyright Designs and Patents Act 1988 or as modified by any successor legislation.

Any use made of information contained in this thesis/dissertation must be in accordance with that legislation and must be properly acknowledged. Further distribution or reproduction in any format is prohibited without the permission of the copyright holder.

Rian, for helping me find the light in my day

## **ii. Abstract**

The work presented within this thesis focuses on the synthesis, characterisation and processing of novel materials for use within solid oxide fuel cells.

A range of perovskite materials, previously shown to have potential for solid oxide fuel cell applications, were selected for further studies. These included  $\text{LaMnO}_3$ ,  $\text{SrFeO}_{3-\delta}$  and  $\text{Sr}_{0.8}\text{Ti}_{0.6}\text{Nb}_{0.4}\text{O}_{3-\delta}$ . These materials were doped with various dopants, including cations such as  $\text{V}^{5+}$  and  $\text{Ti}^{4+}$  and also  $\text{SiO}_4^{4-}$  oxyanions. Once doped, the materials were analysed by X-ray powder diffraction and underwent testing to ascertain their suitability for use as solid oxide fuel cell electrodes. This included identifying structural stability in anode conditions alongside thermal expansion studies. Overall, improvements over undoped samples were noted, especially for  $\text{Sr}_{0.8}\text{Ti}_{0.6}\text{Nb}_{0.4}\text{O}_{3-\delta}$  samples doped with  $\text{V}^{5+}$  and  $\text{SrFeO}_{3-\delta}$  samples doped with  $\text{SiO}_4^{4-}$ , although  $\text{LaMnO}_3$  doped with  $\text{Ti}^{4+}$  proved less successful.

Production methods for the formation of microtubular solid oxide fuel cells were also investigated. Powder processing for paste formation was examined, for subsequent use in extrusion. The extrusion process was also investigated, alongside debinding and sintering studies. The development of a reliable and repeatable process for cell production proved difficult, especially on a smaller scale necessary to facilitate the testing of novel materials.

### **iii. Acknowledgements**

I would like to thank Prof. Peter Slater for all of his help, encouragement and instruction for all of the work carried out under his tutelage. I would also like to extend my thanks to Prof. Kevin Kendall, Prof. Robert Steinberger-Wilckens, Dr. Waldemar Bujalski, Dr. Aman Dhir and Dr. Jose Porras for their input and assistance.

To all of the CDT members, I thank you for your company, help and distraction over the past 4 years. I'd like to thank EPSRC for funding this work, and countless people for helping me carry it out; Carl Meggs, Jackie Deans, Bob Sharpe and the rest of the workshop staff, Artur Majewski, John Hooper, Lynn Draper and the rest of the office staff, Cathryn Hancock, Scott Taylor and Prof. Stuart Blackburn amongst others.

I'd like to thank my family for their unwavering support and encouragement and for pushing me to pursue a PhD. To Rian, you've been a rock through all of this, keeping me motivated and not letting me give in or give up. To the pool players, I congratulate each and every one of you for being just as abysmal after at least two years of practise as you were when we started having a quick break - and continuing to blame poor skill on the cleft of doom.

To the Slater group and the rest of floor 5, thanks for all of the assistance over the years. Much of this work would have been impossible had it not been for your help.

## iv. Table of Contents

i. Title.....	i
ii. Abstract.....	iii
iii. Acknowledgements .....	iv
iv. Table of Contents.....	v
v. List of Figures .....	viii
vi. List of Tables .....	xii
vii. List of Equations.....	xiv
viii. List of Abbreviations.....	xvi
Chapter 1. Introduction.....	1
1.1. Clean Energy Generation .....	1
1.2 Solar Power .....	3
1.3. Wind Power.....	3
1.4. Geothermal.....	4
1.5. Fuel Cells .....	5
1.5.1. Hydrogen as a Fuel.....	6
1.5.2. Methane as a Fuel.....	7
1.5.3. Fuel Cell Material Requirements .....	8
1.5.4. Types of Fuel Cell .....	10
Chapter 2. Solid Oxide Fuel Cell Materials.....	17
2.1. Anode Materials .....	20
2.1.1. Current Material Limitations .....	20
2.1.2. Novel Material Research .....	25
2.2. Cathode Materials .....	33
2.3. Electrolyte Materials .....	35
2.4. Project Aims.....	38
Chapter 3. Experimental Techniques.....	39
3.1. Synthesis Techniques .....	39
3.1.1. Solid State Synthesis .....	39
3.1.2. Co-Precipitation.....	40

3.1.3. Sol-Gel.....	41
3.1.4. Hydrothermal synthesis .....	41
3.2. Pellet Production for Conductivity and Dilatometry Experiments .....	43
3.3. X-Ray Diffraction (XRD) .....	44
3.4. Crystal Symmetry .....	47
3.5. Point Groups and Space Groups .....	51
3.6. Rietveld Refinement .....	51
3.7. Thermogravimetric Analysis coupled to Mass Spectrometry (TGA-MS).....	54
3.8. Dilatometry .....	55
3.9. Electrical Testing .....	57
3.9.1. Four Probe D. C. Conductivity.....	58
3.9.2. Electrochemical Impedance Spectroscopy (EIS) .....	59
3.9.3. Fuel Cell Testing .....	67
3.10. Microtube Manufacture.....	73
3.10.1. Powder Preparation .....	74
3.10.2. Paste Formation .....	75
3.10.3. Cold Extrusion.....	77
3.10.4. Hot Extrusion .....	82
3.10.5. Debinding and Sintering.....	82
3.10.6. Layering.....	83
3.11. Scanning Electron Microscope (SEM) .....	87
Chapter 4. Extrusion and Fabrication of Microtubular SOFCs .....	91
4.1. Introduction.....	91
4.2. Experimental and Results.....	93
4.2.1. Paste Formation.....	93
4.2.2. Extrusion .....	95
4.2.3. Re-Machined Die Set Samples.....	102
4.2.4. Hot Extrusion Samples.....	102
4.2.5. Cell Testing .....	104
4.2.6. SEM Imaging .....	109
4.2.7. Further Extrusion Work.....	113
4.8. Further Work and Conclusions .....	118

Chapter 5. Synthesis and characterisation of Si doped SrFeO <sub>3-δ</sub> for both cathode and anode applications .....	119
5.1. Introduction .....	119
5.2. Experimental .....	121
5.3. Results and Discussion.....	123
5.3.1. Synthesis and Structure Determination .....	123
5.3.2. Electrical Conductivity Measurements .....	127
5.3.3. Area Specific Resistance .....	131
5.3.4. Dilatometry.....	135
5.3.5. Fuel Cell Testing .....	138
5.4. Conclusions .....	140
Chapter 6. Synthesis and characterisation of V doped Sr <sub>0.8</sub> Ti <sub>0.6</sub> Nb <sub>0.4</sub> O <sub>3-δ</sub> for SOFC Applications .....	141
6.1. Introduction .....	141
6.2. Experimental .....	143
6.3. Results and Discussion.....	145
6.3.1. Synthesis and Structure Determination .....	145
6.3.2. 4-Probe DC Conductivity .....	151
6.3.3. Area Specific Resistance .....	153
6.3.4. Reoxidation Studies.....	156
6.3.6. Dilatometry.....	158
6.4. Conclusions and Further Work .....	161
Chapter 7. Synthesis and characterisation of La <sub>1-x</sub> Mn <sub>x</sub> Mn <sub>1-x</sub> Ti <sub>x</sub> O <sub>3-δ</sub> for SOFC applications .....	162
7.1. Introduction .....	162
7.2. Experimental .....	164
7.3. Results and Discussion.....	165
7.3.1. Synthesis and Structure Determination .....	165
7.3.2. Conductivity Measurements.....	168
7.4. Conclusions .....	173
Chapter 8. Conclusions and Further Work .....	174
Chapter 9. Publications .....	178
Chapter 10. References .....	178

## **v. List of Figures**

Figure 1. Diagram of the most common types of fuel cell, the fuel and oxidising agents required, typical operating temperatures and the electrolyte ion transfer type and direction

Figure 2. Cubic and orthorhombic perovskite structures

Figure 3. An example of the triple phase boundary in a SOFC utilising a YSZ/NiO cermet as the anode

Figure 4. Two crystal planes with spacing 'd' showing reflection of X-rays

Figure 5. The 14 Bravais lattice unit cell types [106]

Figure 6. Miller Indices for several lattice planes [106]

Figure 7. Diffraction pattern undergoing refinement using the GSAS suite

Figure 8. Electrode configuration for 4-probe DC conductivity

Figure 9. Example of a Nyquist-plot for ionic conducting solids, demonstrating different physical phenomena.  $Z''$  = imaginary impedance,  $Z'$  = real impedance

Figure 10. Schematic diagram of the fuel cell test equipment used in this thesis

Figure 11. Schematic diagram of the pellet cell test setup used in this thesis

Figure 12. Example fuel cell polarisation curve showing the three main sources of voltage losses

Figure 13. Schematic of an anode-supported m-SOFC [111]

Figure 14. The Bridge twin roll mill used for this work

Figure 15. Diagram detailing a basic extrusion technique

Figure 16. Extrusion rod complete with mandrel, without and with extrusion die and alignment cylinder

Figure 17. Extrusion ram and mandrel with YSZ/NiO paste wrapped around it. (L) shows before insertion into extrusion barrel, (R) is setup complete with die as it would be inside the barrel

Figure 18. Instron 4467 with 30kN load cell and sample installed (L), close-up of sample ready to extrude (R)

Figure 19. Flow diagram for microtubular solid oxide fuel cell manufacture

Figure 20. Graph showing sintering profiles for NiO-only samples (batch 1A) and CuO-containing samples (batches 1B and 1C)

Figure 21. Voltages for cells moving from OCV to 0.05 A current demand

Figure 22. Voltages for cells moving from OCV to 0.01 A current demand

Figure 23. Voltages and currents for cells moving from OCV to 0.9 V voltage demand

Figure 24. SEM images of tubes extruded of various batches and in various states of production. a = YSZ-NiO-CuO as extruded, b = YSZ-CuO debound and sintered at 1100 °C, c = YSZ-NiO debound and sintered at 1400 °C, d = YSZ-CuO as extruded, e = YSZ-NiO debound and sintered at 1300 °C then YSZ electrolyte deposited and sintered at 1300 °C, f = YSZ-NiO debound and sintered at 1100 °C, g = YSZ-NiO as extruded

Figure 25. Voltages and currents for cells (extruded using the remanufactured die set) moving from OCV to 0.9 V voltage demand

Figure 26. XRD pattern for  $\text{SrFeO}_{3-\delta}$  in air (bottom) and annealed in 5%  $\text{H}_2/\text{N}_2$  at 600 °C for 24 hours (top)

Figure 27. XRD pattern for  $\text{SrFe}_{0.9}\text{Si}_{0.1}\text{O}_{3-\delta}$  in air (bottom) and annealed in 5%  $\text{H}_2/\text{N}_2$  at 600 °C for 24 hours (top)

Figure 28. Kröger-Vink notation showing silica incorporation causes oxygen vacancies and Fe reduction

Figure 29. Plot of conductivity against temperature for the series  $\text{SrFe}_{1-x}\text{Si}_x\text{O}_{3-\delta}$  in air

Figure 30. Plot of conductivity against temperature for the series  $\text{SrFe}_{1-x}\text{Si}_x\text{O}_{3-\delta}$  in 5% $\text{H}_2/\text{N}_2$

Figure 31. Nyquist plot for  $\text{SrFe}_{0.9}\text{Si}_{0.1}\text{O}_{3-\delta}$  at 800°C in air, including fitting

Figure 32. Nyquist plot for  $\text{SrFe}_{0.9}\text{Si}_{0.1}\text{O}_{3-\delta}$  at 600°C in 5% $\text{H}_2/\text{N}_2$ , including fitting

Figure 33. Dilatometry data for  $\text{SrFeO}_{3-\delta}$  from 20 - 1000 °C at 15 °C  $\text{min}^{-1}$  in air. Solid line is TEC profile, dashed line is temperature profile

Figure 34. Dilatometry data for  $\text{SrFe}_{0.95}\text{Si}_{0.05}\text{O}_{3-\delta}$  from 20 - 1000 °C at 15 °C  $\text{min}^{-1}$  in air. Solid line is TEC profile, dashed line is temperature profile

Figure 35. Dilatometry data for  $\text{SrFe}_{0.9}\text{Si}_{0.1}\text{O}_{3-\delta}$  from 20 - 1000 °C at 15 °C  $\text{min}^{-1}$  in air. Solid line is TEC profile, dashed line is temperature profile

Figure 36. Voltages and currents for symmetrical pellet cells of  $\text{SrFe}_{0.9}\text{Si}_{0.1}\text{O}_{3-\delta}$  on YSZ at 800°C moving from OCV to 0.85 V voltage demand

Figure 37. Graph showing unit cell volume ( $\text{\AA}^3$ ) for  $\text{Sr}_{0.8}\text{Ti}_{0.6}\text{Nb}_{0.4-x}\text{V}_x\text{O}_{3-\delta}$  against V content

Figure 38. XRD pattern for  $\text{Sr}_{0.8}\text{Ti}_{0.6}\text{Nb}_{0.2}\text{V}_{0.2}\text{O}_{3-\delta}$  in air (bottom) and annealed in 5% $\text{H}_2/\text{N}_2$  at 600 °C for 24 hours (top)

Figure 39. XRD pattern for  $\text{Sr}_{0.8}\text{Ti}_{0.6}\text{Nb}_{0.15}\text{V}_{0.25}\text{O}_{3-\delta}$  in air (bottom) and annealed in 5% $\text{H}_2/\text{N}_2$  at 600 °C for 24 hours (top)

Figure 40. XRD pattern for  $\text{Sr}_{0.8}\text{Ti}_{0.6}\text{V}_{0.4}\text{O}_{3-\delta}$  in air (bottom) and annealed in 5% $\text{H}_2/\text{N}_2$  at 600 °C for 24 hours (top)

Figure 41. XRD pattern for  $\text{Sr}_{0.75}\text{Ti}_{0.5}\text{V}_{0.5}\text{O}_{3-\delta}$  in air showing single phase purity

Figure 42. Graph showing unit cell volume ( $\text{\AA}^3$ ) for  $\text{Sr}_{0.8}\text{Ti}_{0.6}\text{Nb}_{0.4-x}\text{V}_x\text{O}_{3-\delta}$  (unreduced and reduced at 930 °C) against V content

Figure 43. Plot of conductivity against temperature for the series  $\text{Sr}_{0.8}\text{Ti}_{0.6}\text{Nb}_{0.4-x}\text{V}_x\text{O}_{3-\delta}$  in 5%  $\text{H}_2/\text{N}_2$

Figure 44. ASR Nyquist plot for  $\text{Sr}_{0.8}\text{Ti}_{0.6}\text{Nb}_{0.2}\text{V}_{0.2}\text{O}_{3-\delta}$  at 800°C in air, including fitting

Figure 45. ASR Nyquist plot for  $\text{Sr}_{0.8}\text{Ti}_{0.6}\text{Nb}_{0.2}\text{V}_{0.2}\text{O}_{3-\delta}$  at 800°C in 5%  $\text{H}_2/\text{N}_2$ , including fitting

Figure 46. Conductivity against time for samples of  $\text{Sr}_{0.8}\text{Ti}_{0.6}\text{Nb}_{0.4-x}\text{V}_x\text{O}_{3-\delta}$  exposed to air post reduction in 5%  $\text{H}_2/\text{N}_2$

Figure 47. Dilatometry data for  $\text{Sr}_{0.8}\text{Ti}_{0.6}\text{Nb}_{0.4}\text{O}_{3-\delta}$  from 20 - 1000 °C at 15 °C  $\text{min}^{-1}$  in air. Solid line is TEC profile, dashed line is temperature profile

Figure 48. Dilatometry data for  $\text{Sr}_{0.8}\text{Ti}_{0.6}\text{Nb}_{0.2}\text{V}_{0.2}\text{O}_{3-\delta}$  from 20 - 1000 °C at 15 °C  $\text{min}^{-1}$  in air. Solid line is TEC profile, dashed line is temperature profile

Figure 49. XRD pattern for  $\text{La}_{0.8}\text{MnTi}_{0.2}\text{O}_{3-\delta}$  in air (bottom) and annealed in 5%  $\text{H}_2/\text{N}_2$  at 800 °C for 24 hours (top)

Figure 50. XRD pattern for  $\text{La}_{0.7}\text{MnTi}_{0.3}\text{O}_{3-\delta}$  in air (bottom) and annealed in 5%  $\text{H}_2/\text{N}_2$  at 800 °C for 24 hours (top)

Figure 51. XRD pattern for  $\text{La}_{0.6}\text{MnTi}_{0.4}\text{O}_{3-\delta}$  in air (bottom) and annealed in 5%  $\text{H}_2/\text{N}_2$  at 800 °C for 24 hours (top)

Figure 52. Variation in the conductivities of the series  $\text{La}_{1-x}\text{Mn}_x\text{Mn}_{1-x}\text{Ti}_x\text{O}_{3-\delta}$  in air and 5%  $\text{H}_2/\text{N}_2$  at 850 °C

Figure 53.  $\text{Log}_{10} \sigma$  vs  $1000/T$  for the series  $\text{La}_{1-x}\text{Mn}_x\text{Mn}_{1-x}\text{Ti}_x\text{O}_{3-\delta}$  in air

Figure 54. Graph of  $\text{Log}_{10} \sigma$  vs  $1000/T$  of series  $\text{La}_{1-x}\text{Mn}_x\text{Mn}_{1-x}\text{Ti}_x\text{O}_{3-\delta}$  in 5%  $\text{H}_2/\text{N}_2$

## **vi. List of Tables**

Table 1. Unit cell symmetries, side lengths and angles

Table 2. Quantities of powders used to make up the cermet for different samples

Table 3. Binder materials used for paste formation

Table 4. Firing Profile for sample 1A

Table 5. Firing Profile for samples 1B and 1C

Table 6. Initial composition of electrolyte slurry used for dip coating

Table 7. Composition of cathode inks 1 and 2

Table 8. Composition of electrolyte slurry used for manual deposition

Table 9. Unit cell parameters and volumes (per formula unit) for the series  $\text{SrFe}_{1-x}\text{Si}_x\text{O}_{3-\delta}$

Table 10. Oxidation state and oxygen deficiencies for the series  $\text{SrFe}_{1-x}\text{Si}_x\text{O}_{3-\delta}$

Table 11. Conductivity data for  $\text{SrFe}_{1-x}\text{Si}_x\text{O}_{3-\delta}$  in air

Table 12. Conductivity data for  $\text{SrFe}_{1-x}\text{Si}_x\text{O}_{3-\delta}$  in 5%  $\text{H}_2/\text{N}_2$

Table 13. ASR values for the series  $\text{SrFe}_{1-x}\text{Si}_x\text{O}_{3-\delta}$  in air

Table 14. ASR values for the series  $\text{SrFe}_{1-x}\text{Si}_x\text{O}_{3-\delta}$  in 5%  $\text{H}_2/\text{N}_2$

Table 15. TEC data for the series  $\text{SrFe}_{1-x}\text{Si}_x\text{O}_{3-\delta}$

Table 16. Unit cell size and cell volume for  $\text{Sr}_{0.8}\text{Ti}_{0.6}\text{Nb}_{0.4-x}\text{V}_x\text{O}_{3-\delta}$

Table 17. Unit cell size and cell volume for  $\text{Sr}_{0.8}\text{Ti}_{0.6}\text{Nb}_{0.4-x}\text{V}_x\text{O}_{3-\delta}$  reduced at 930 °C in 5%  $\text{H}_2/\text{N}_2$

Table 18. 4-probe DC conductivity data for the series  $\text{Sr}_{0.8}\text{Ti}_{0.6}\text{Nb}_{0.4-x}\text{V}_x\text{O}_{3-\delta}$  in 5%  $\text{H}_2/\text{N}_2$  post reduction at 930 °C

Table 19. ASR data for the material  $\text{Sr}_{0.8}\text{Ti}_{0.6}\text{Nb}_{0.2}\text{V}_{0.2}\text{O}_{3-\delta}$  in both air and 5%  $\text{H}_2/\text{N}_2$

Table 20. Conductivity ( $\text{S cm}^{-1}$ ) against time (s) for samples of  $\text{Sr}_{0.8}\text{Ti}_{0.6}\text{Nb}_{0.4-x}\text{V}_x\text{O}_{3-\delta}$  exposed to air post reduction in 5%  $\text{H}_2/\text{N}_2$

Table 21. TEC data for the materials  $\text{Sr}_{0.8}\text{Ti}_{0.6}\text{Nb}_{0.4}\text{O}_{3-\delta}$  and  $\text{Sr}_{0.8}\text{Ti}_{0.6}\text{Nb}_{0.2}\text{V}_{0.2}\text{O}_{3-\delta}$

Table 22. Unit cell parameters and cell volumes for the series  $\text{La}_{1-x}\text{Mn}_x\text{Mn}_{1-x}\text{Ti}_x\text{O}_3$

Table 23. Conductivity data in air for the series  $\text{La}_{1-x}\text{Mn}_x\text{Mn}_{1-x}\text{Ti}_x\text{O}_3$

Table 24. Conductivity data in 5%  $\text{H}_2/\text{N}_2$  for the series  $\text{La}_{1-x}\text{Mn}_x\text{Mn}_{1-x}\text{Ti}_x\text{O}_3$  in 5%  $\text{H}_2/\text{N}_2$

## **vii. List of Equations**

Equation 1. Steam reformation of methane

Equation 2. Goldschmidt's tolerance factor calculation for perovskite stability (where  $t$  = tolerance factor,  $r_A/r_B/r_O$  = ionic radius of the A-site/B-site/O-site)

Equation 3. Sulphur poisoning of nickel within SOFC anodes

Equation 4. Partial oxidation of methane

Equation 5. Dry reformation of methane

Equation 6. Bragg's law, where  $n$  = integer,  $d$  = crystal plane spacing,  $\lambda$  = wavelength of X-rays used and  $\theta$  = angle of the X-rays in relation to the plane

Equation 7. Expression for calculation of linear thermal expansion coefficients, where  $\alpha$  = TEC,  $L_i$  = initial length,  $L_f$  = final length,  $T_i$  = initial length and  $T_f$  = final length

Equation 8. Calculation for 4 probe DC conductivity (where  $\sigma$  = conductivity,  $L$  = distance between electrodes 2 and 3,  $A$  = pellet cross-sectional area,  $I$  = current passed between electrodes 1 and 4,  $V$  = voltage difference between electrodes 2 and 3)

Equation 9. Expression for a sinusoidal voltage, where  $e$  = observed voltage at time  $t$ ,  $E$  = input voltage and  $\omega$  = frequency (in Hz) times  $2\pi$

Equation 10. Expression for the phase shift between input voltage and output current, where  $i$  = current,  $I$  = the maximum amplitude of the current and  $\phi$  = phase angle between input and output

Equation 11. Expression for the capacitive resistance  $X_c$  for a pure capacitor, where  $X_c = 1/\omega C$

Equation 12. Expression for the current of a pure resistor, where  $R$  = resistance

Equation 13. Expression for the voltage-current relationship for a pure capacitor, where  $\bar{E}$  = voltage amplitude,  $j = \sqrt{-1}$  and  $\bar{I}$  = current amplitude

Equation 14. Capacitance and resistance components in series

Equation 15. Expression defining impedance  $Z$

Equation 16. Expression showing the two components of the impedance, where  $Z_{Re}$  = real part ( $R$ ) and  $Z_{Im}$  = imaginary part ( $X_c$ )

Equation 17. Expression for the calculation of activation energy as a function of the properties of the sample and the temperature, where  $\sigma$  = conductivity,  $T$  = temperature,  $A$  = sample surface area,  $E_a$  = activation energy and  $R$  = resistance

Equation 18. Typical impedance ( $Z$ ) where  $Z'$  is the real part,  $j$  is the imaginary unit,  $\omega$  is the frequency and  $Z''$  is the imaginary part

Equation 19. Calculation to determine the ASR from the intercept points on a Nyquist plot, where  $I_H$  = high intercept,  $I_L$  = low intercept,  $n$  = number of sides (in the case of a pellet, always 2) and  $A$  = area of one face

Equation 20. Gibbs free energy change of the reaction of hydrogen and oxygen to form water

Equation 21. Gibbs free energy change for the reaction of hydrogen and oxygen to form water, with respect to partial pressure of gases

Equation 22. Calculation of electromotive force between anode and cathode in a fully reversible system

Equation 23. Nernst equation for the reaction of hydrogen and oxygen to form water

## **viii. List of Abbreviations**

AEMFC	Alkaline Exchange Membrane Fuel Cell
AFC	Alkaline Fuel Cell
ASR	Area Specific Resistance
BSCF	$\text{Ba}_{0.5}\text{Sr}_{0.5}\text{Co}_{0.8}\text{Fe}_{0.2}\text{O}_{3-\delta}$
BZCY	$\text{Ba}(\text{Zr/Ce})_{1-y}\text{Y}_y\text{O}_{2-y}$
CGO	Cerium Gadolinium Oxide
CVD	Chemical Vapour Deposition
EDX	Energy-Dispersive X-ray spectroscopy
EIS	Electrochemical Impedance Spectroscopy
FIT	Feed In Tariff
GDC	(See CGO)
GSAS	General Structure Analysis System
ICE	Internal Combustion Engine
IT-SOFC	Intermediate Temperature Solid Oxide Fuel Cell
LDC	$\text{La}_{0.4}\text{Ce}_{0.6}\text{O}_{2-\delta}$
LNF	$\text{LaNi}_{1-x}\text{Fe}_x\text{O}_3$
LSCF	$(\text{La/Sr})_{1-x}\text{Co}_y\text{Fe}_{1-y}\text{O}_{3-\delta}$
LSCM	$(\text{La/Sr})_{1-x}\text{Cr}_y\text{Mn}_{1-y}\text{O}_{3-\delta}$
LSF	$\text{La}_{0.6}\text{Sr}_{0.4}\text{FeO}_{3-\delta}$
LSGM	$\text{La}_{1-x}\text{Sr}_x\text{Ga}_{0.8}\text{Mg}_{0.2}\text{O}_{3-\delta}$
LSM	$\text{La}_{1-x}\text{Sr}_x\text{MnO}_{3-\delta}$
MCFC	Molten Carbonate Fuel Cell
MFC	Mass Flow Controller

m-CHP	micro Combined Heat and Power
MIEC	Mixed Ionic-Electronic Conductor
m-SOFC	microtubular Solid Oxide Fuel Cell
NASA	North American Space Agency
NiS	Nickel Sulphide
OCV	Open Cell Voltage
PAFC	Phosphoric Acid Fuel Cell
PEHD	High Density Polyethylene
PEMFC	Proton Exchange Membrane Fuel Cell
PFA	Pore Forming Agent
PMMA	Polymethylmethacrylate
PPM	Parts Per Million
PVA	Polyvinyl Alcohol
PVB	Polyvinyl Butaryl
PVD	Physical Vapour Deposition
SDC	Samaria-Doped Ceria
SEM	Scanning Electron Microscope
SOFC	Solid Oxide Fuel Cell
STP	Standard Temperature and Pressure (298K, 100kPa)
TEC	Thermal Expansion Coefficient
TGA-MS	Thermogravimetric Analysis - Mass Spectrometry
TPB	Triple Phase Boundary
TPO	Temperature Programmed Oxidation
XRD	X-Ray Diffraction
YSZ	Yttira-Stabilised Zirconia

# **Chapter 1. Introduction**

This Chapter introduces the concept of clean energy generation and the need for its implementation. It covers a broad view of the industry and relevant technologies, largely centred on fuel cells. It finishes with an in-depth look at solid oxide fuel cells (SOFCs) including the requirement for materials to be used within these systems.

## **1.1. Clean Energy Generation**

The UK is committed to reducing carbon emissions by 60% relative to 1990 emissions by 2050, a level which will be hard to achieve due to the continuing trend towards increasing energy consumption. In order to be on track to achieve this goal, the target of completely decarbonising the electricity system by 2030 has been identified as a key stage towards achieving the reduction in CO<sub>2</sub> emissions required. This can be achieved by replacing the generation capacity of older power station with high carbon emissions per gigawatt-hour (GWh), such as coal-fired plants, with renewable energy sources such as wind farms, geothermal power plants, nuclear power and various solar-based technologies. However, a major drawback preventing the large-scale uptake of many forms of renewable energy is the unreliable nature of generation. For example, the wind blows intermittently so power can be generated at times of low demand such as the middle of the night, and conversely at times of high demand the wind may be calm leading to low levels of power generation. This increases the difficulty of the task of grid balancing, the act of ensuring that the demands for electricity on the grid are matched to

the output of all generators attached to the grid, which must be carried out in real time. This is perceived to be a major obstacle to overcome before renewable generation can become a large proportion of the energy mix; indeed, it has been estimated that once renewables reach 30% of the total grid capacity the stability of the system will be compromised without large-scale capacity for energy storage [1].

A concept that has come to the fore in recent years is that of microgeneration. In the UK, this has largely been driven by feed-in tariffs (FITs) and is most noticeable by the uptake of solar photovoltaic installations. However microgeneration, like the FITs, is not limited to solar photovoltaic and covers a wide range of technologies such as small-scale wind turbines and Micro Combined Heat and Power (micro-CHP). Microgeneration has the advantage of having virtually no transmission losses as the electricity is usually consumed close to the source. It is also useful to allow communities to continue functioning if the national grid was to go down. However, the smaller scales involved generally leads to lower efficiencies, offsetting the transmission losses. In addition, it makes management of the national grid more difficult as the production sites are not centralised and controllable in the way that large-scale power stations are. Nevertheless, the lower average carbon footprint of power generated against traditional coal, gas or oil fired power stations is still reason enough for many governments to provide incentives to increase installations and capacity for microgeneration.

## **1.2 Solar Power**

Solar power harnesses the energy given off by the sun. This can be achieved in several ways; the most commonly seen is photovoltaics, and arguably the most simple is solar thermal hot water panels. The former is the conversion of electromagnetic radiation to electric current; while the latter involves the direct use of heat which is transported by a fluid medium, usually water. However there are a number of other technologies that make use of the sun's energy, including turbines driven by a heated fluid medium such as liquid sodium or supercritical steam [2]. Storage of this heated fluid can allow generation to take place at times of low solar flux, such as overcast periods of the day, or even at night, which can help to balance the load on the grid.

In the UK, the uptake of small-scale photovoltaic systems has greatly expanded since the introduction of the FITs, to the point where the value of the tariffs was reduced in 2011 to reflect the increase in installations and reduction in purchase and installation cost.

## **1.3. Wind Power**

Generating electricity from the power inherent in the wind generally involves the use of tall wind turbines. These have a series of blades that are driven by the wind and drive an alternator. The location of these turbines can vary but is greatly affected by land topography as this has a direct influence on wind speeds. It is for this reason that many banks of wind turbines are located in the seas and oceans close to the shoreline; this leads to their name, offshore wind farms. There are advantages to situating wind farms

onshore, however, as construction costs are typically much lower than those offshore. The World Wind Association has calculated that as of June 2013 the capacity of wind-generated electricity has surpassed 296 GW [3]. With total generation capacity in the region of 4900 GW, this represents 6% of worldwide power production, a huge increase even on 2005 levels where capacity was around 50 GW.

It is also becoming increasingly common to fit small turbines onto or into tall structures and within cities. These largely rely on winds being channelled between buildings to provide a stronger air flow, but can also harness the higher wind speeds present above the height of surrounding buildings. For example, the 'Strata' tower, located in the Elephant and Castle district of London, has 3 turbines rated at 19 kW each incorporated into its pinnacle which can produce up to 50 MWh of electricity every year [4].

#### **1.4. Geothermal**

Energy can also be extracted from bedrock where the temperature is great enough; this is referred to as geothermal energy production. There are several different methods used to extract the energy from the rock, each with their own advantages and disadvantages. These include the use of naturally occurring steam to drive turbines, pumping water down to extract the heat directly through powering a turbine, or by using a binary system where the heated water goes through a heat exchanger and heats a fluid medium in a closed system which drives a turbine. There is also the potential for heated water to be directly supplied to houses for heating purposes. Each variation on geothermal technologies is suited to certain geographical features and rock types and is reliant on

sufficient heat being present close enough to the earth's surface to warrant extraction. This generally hinges around a high temperature differential in the crust of the earth to provide a large potential heat capacity, without having to pump the heated fluid too far down into the ground. The geographic limitations of geothermal generation severely curtail the expansion of this technology, meaning that while it remains a valid contributor to a lower-carbon future it will likely struggle to be a primary source of power worldwide and will remain a viable source of power in a small number of locations only, such as Iceland and the Philippines [5].

## **1.5. Fuel Cells**

Fuel cells work on a similar principal to batteries, namely they convert chemical energy to electrical energy via electrochemical reactions. However, unlike a battery, a fuel cell requires an external supply of fuel such as hydrogen. While this makes the system more complex, it also dramatically increases the potential time that the cell can run for, as well as removing the lengthy recharge time inherent to batteries. Fuel cells can also be scaled in a similar way to batteries with a large range of power capacities possible, potentially able to power small devices only requiring a few milliwatts of power through to large scale applications generating megawatts of power. However, it should be stressed that fuel cells are not directly a green energy generation technology, as they require fuel to run and that fuel must be produced. They are most commonly linked with hydrogen, which doesn't exist naturally on earth as molecular hydrogen and must be obtained from other sources, such as splitting water into elemental oxygen and hydrogen. However, certain fuel cell systems such as SOFCs can theoretically run on a large range of fuels

including hydrocarbons, allowing them to bridge the technological gap between hydrocarbon fuels currently widely available and those available in the future such as hydrogen. One of the main advantages of fuel cell systems is that they are very efficient, often reaching over 50% system efficiencies, so when compared to other technologies such as the internal combustion engine (ICE), that typically reach peak efficiencies of 25%, the benefits can clearly be seen.

### **1.5.1. Hydrogen as a Fuel**

The case for hydrogen as a fuel has many positive points. When hydrogen reacts with oxygen, either through combustion or in an electrochemical cell, the only by-product is water. Hydrogen therefore has zero harmful emissions at the point of use. Unfortunately, elemental hydrogen is not present on earth and so hydrogen must be produced by other means. There are several means to produce hydrogen but all require an energy input of some kind; for example, electrolysis of water produces hydrogen and oxygen but requires a large electrical input, negating the cleanliness of the fuel at the point of use unless the energy input is also clean, e.g. from renewable energy sources.

The majority of the world's supply of hydrogen is currently captured as a by-product of hydrocarbon processing. This accounts for approximately 95% of hydrogen commercially available and clearly is not a suitable source for hydrogen if the purpose of utilising hydrogen is to reduce the carbon footprint of your fuel. It is therefore important to move towards renewable production of hydrogen.

In this respect, it may be possible to use the unpredictable nature of most renewable energy sources to the advantage of hydrogen production. This could be achieved through utilising the electricity to power hydrogen production, for example electrolysis, when there is excess being produced, and so use the production of hydrogen as a form of energy storage [6]. This production could be carried out anywhere with an electricity grid connection, but would need to be controlled as part of the grid in order to be most effective.

### **1.5.2. Methane as a Fuel**

As some fuel cells such as SOFCs can utilise hydrocarbons as fuels, another use for excess grid electricity could be the production of gas such as methane, again to act as a form of energy storage. Once again, production could be distributed and would not need to be local to electricity production. However, producing methane has a distinct advantage over the production of hydrogen, namely the natural gas grid network. This network could accept all of the methane produced and so minimise the need for local storage. If the methane was produced from renewable energy sources it could also contribute towards lowering the carbon footprint of the gas grid, and reduce the dependence on foreign fuel imports, so giving much greater energy security. This idea of using renewably-produced methane lends support for the continuing development of SOFCs since these have the fuel flexibility to take advantage of the gas grid while remaining electrically efficient.

In order for methane or other hydrocarbons to be utilised as a fuel within most cells, reformation must take place. This is most commonly carried out in the presence of water and is known as steam reformation, the endothermic reaction of water with methane to produce hydrogen and carbon monoxide, as seen in Equation 1.



*Equation 1. Steam reformation of methane*

Steam reformation of methane is necessary due to the requirement of hydrogen as a fuel for most types of fuel cell, and typically must be carried out before the fuel enters the cell. However, in the case of high temperature cells such as SOFCs the reformation can be performed within the cell itself as the high temperatures provide the energy required to drive the reaction towards hydrogen production.

### **1.5.3. Fuel Cell Material Requirements**

A fuel cell is a device that converts chemical energy to electrical energy by way of an electrochemical reaction, with heat as the main by-product. In the most basic analysis, a fuel cell has three distinct sections, the electrolyte, the anode and the cathode. Fuel is introduced on the anode side of the system, an oxygenating substance (typically oxygen in the air) is introduced at the cathode side, and they are separated by the electrolyte layer. This electrolyte layer allows ions to pass through it, with the type of ion determined by the type of fuel cell. The electrolyte material is also an electronic insulator

and so forces electrons to move around an external circuit where they do work, providing the electric output of the system.

#### **1.5.3.1. Electrolyte Layer**

The electrolyte layer sits between the anode and cathode layers, providing a boundary between them. It has different requirements of it depending on which fuel cell system is being analysed; however, certain general characteristics must be present. It should be an electrical insulator, forcing electrons to move separately around the system in order to generate an electrical potential. It should also be an ionic conductor; the type of ions conducted and the temperature of maximum conductivity depends on the type of fuel cell. The different types of fuel cell are named after their electrolyte material; for example, Proton Exchange Membrane cells rely on an electrolyte layer which conduction protons.

#### **1.5.3.2. Anode Layer**

The anode layer is generally where the fuel first contacts the cell. It must be stable under highly reducing conditions and provide some level of ionic conduction to allow ion transfer between the electrolyte and anode materials, as well as electronic conduction to allow the movement of electrons. In addition, it should be chemically inert with respect to the electrolyte material. It should also provide catalytic activity in order to enhance reactions taking place at the surface. These reactions will be detailed in upcoming sections.

### **1.5.3.3. Cathode Layer**

This must be stable in oxidising environments and is directly in contact with the oxidising agent, typically oxygen from the air. Similarly to the anode, it should provide some level of ionic and electronic conductivity in order to allow the movement of ions between cathode and electrolyte and the movement of electrons, as well as also not reacting with the electrolyte.

### **1.5.4. Types of Fuel Cell**

There are several types of fuel cell under development, all of which have different characteristics and potential uses. The most commonly studied are discussed below. Figure 1 shows a breakdown of the different fuel cell types, their operating temperatures and electrolyte types.

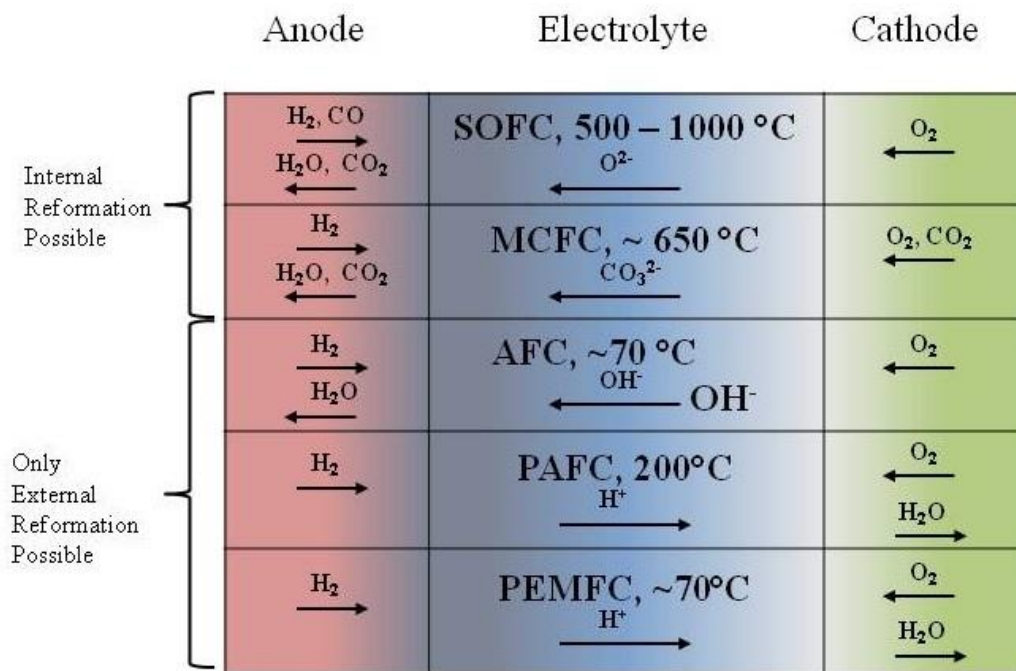


Figure 1. Diagram of the most common types of fuel cell, the fuel and oxidising agents required, typical operating temperatures and the electrolyte ion transfer type and direction

#### 1.5.4.1. Proton Exchange Membrane Fuel Cell (PEMFC)

Proton exchange membrane fuel cells, also known as polymer electrolyte membrane fuel cells, require high purity hydrogen to operate. They typically utilise carbon-supported electrodes containing noble metals with an electrolyte consisting of proton-conducting polymers such as Nafion®. Hydrogen enters the cell on the anode side and is broken down into protons, which flow through the electrolyte membrane, and electrons, which flow around the external circuit to the cathode. Here, the protons and electrons react with oxygen to form water as the only waste product. The high cost of the materials currently

used has led to much research focusing on alternatives to make these cells more financially viable. In addition, the metal catalysts used are susceptible to poisoning from contaminants present in the fuel supply. This stringent requirement for fuel purity mean that reformers intended to supply the cell with hydrogen from a hydrocarbon fuel source must have additional filters, or be more complex than if the cell was less susceptible to poisoning.

Operating temperatures are typically in the region of 50 - 150 °C, so PEMFCs are considered low temperature fuel cells. This low temperature requirement allows PEMFCs to start and stop operation rapidly, making them highly suited to mobile applications. However, it also means that they generally are unsuitable for combined heat and power applications as the heat output is too low.

#### **1.5.4.2. Alkaline Fuel Cell (AFC)**

Alkaline fuel cells are amongst the longest-proven fuel cells, having been used in the Apollo series of missions run by NASA. They are based around an electrolyte which is strongly alkaline, normally concentrated sodium or potassium hydroxide in liquid form with an inert porous solid support. Oxygen and water combine at the cathode to form hydroxide ions, drawing electrons from the external circuit. The hydroxide ions pass through the electrolyte substance and react with hydrogen at the anode to form water, releasing electrons which can flow around the external circuit back to the cathode. AFCs, like PEMFCs, are classified as low temperature fuel cells, with typical operating temperatures between 25 – 75°C.

Carbon dioxide must be removed from the gas coming into the cathode side as it poisons the cell by reacting with NaOH/KOH forming  $\text{Na}_2\text{CO}_3/\text{K}_2\text{CO}_3$  which can block the catalytic sites. As with PEMFCs, AFCs require high purity hydrogen. This gas processing at both the anode and cathode sides drive up system complexity and increases parasitic load, leading to lower overall system efficiencies. In addition, noble metals such as platinum are commonly used within the electrodes which also drive up cost. This, combined with the hazardous liquid electrolyte material used, is the reason that research into and demand for alkaline fuel cells has waned somewhat, with more interest being paid to PEMFCs. However, research is ongoing into cheaper, non-precious metal catalyst materials, which are believed possible due to the more favourable electrode processes in alkaline conditions, has recently reinvigorated research into AFCs.

#### **1.5.4.3. Alkaline Exchange Membrane Fuel Cell (AEMFC)**

Alkaline exchange membrane fuel cells are a relatively recent development, having first been discussed at length in 2005 [7]. These cells use a solid alkaline polymer as the electrolyte material which can tolerate operation in the presence of  $\text{CO}_2$ , therefore removing the requirement of cathode gas cleaning present in AFCs. The other advantages of AFCs are still present, such as the potential for non-precious metal low cost catalysts and low operating temperature. However, as with any new technology there are still many obstacles to be overcome, such as the development of an effective alkaline ionomer which is easily dispersed and maximises the ionic contact between the ion membranes and electrode layers.

#### **1.5.4.4. Phosphoric Acid Fuel Cell (PAFC)**

Utilising an electrolyte composed of phosphoric acid at high concentrations, these cells are much more tolerant to impurities than both PEMFCs and AFCs. The phosphoric acid is typically used at such high concentrations that it forms pyrophosphoric acid ( $\text{H}_4\text{P}_2\text{O}_7$ ), which freezes at room temperature; it is for this reason that the elevated operating temperatures (150 - 200 °C) are usually maintained for the life of the cell, making them ideally suited for uninterruptable power supply or continuous load applications. They are also suitable for use in vehicles that spend the majority, if not all of their time, requiring a power output, such as buses or ships.

Operation reactions are very similar to those in PEMFCs, however the electrolyte is a configuration more similar to AFCs, with a liquid conducting medium supported by a solid porous structure. However, similarly to AFCs, the hazardous electrolyte material and also the constant operation requirement make maintenance difficult, and the electrodes again typically also contain platinum, which drives the cost up.

#### **1.5.4.5. Molten Carbonate Fuel Cell (MCFC)**

Molten Carbonate Fuel Cells operate at a range of temperatures above 500°C, allowing non-precious metals to act as catalysts in order to keep costs down. The electrolyte is composed of a molten salt mixture which conducts carbonate ions, again within a porous inert solid support. Carbon dioxide must be present at the cathode in order to generate the  $\text{CO}_3^{2-}$ , and this is often achieved through recycling the exhaust gas to increase the

CO<sub>2</sub> partial pressure. MCFCs can operate on a wide range on fuels, including some that are poisons to other fuel cells, such as carbon monoxide. If running on hydrocarbons then internal reforming can occur, allowing the system to utilise them directly. This fuel flexibility grants the system a considerable advantage over many other fuel cells covered previously, as MCFCs could be run on widely available commercial fuels without the need for a change of infrastructure.

However, the high temperatures and hazardous electrolyte materials used do have their drawbacks. In this respect the durability of the cell is compromised due to the corrosion of components in the harsh chemical conditions. Significant current research is therefore concentrated on materials which can withstand this environment while maintaining high levels of efficiency. In addition, the high operating temperatures mean that a fast on-off cycle is difficult to achieve, rendering MCFCs unsuitable to a wide range of applications requiring temporary or intermittent power.

#### **1.5.4.6. Solid Oxide Fuel Cell (SOFC)**

Solid Oxide Fuel Cells have the highest operating temperature region, between 500 – 1000 °C. They make use of a solid gas-tight electrolyte, usually a ceramic, which can conduct oxide ions. Oxygen enters the cell at the cathode side and is reduced to oxide ions, which pass through the electrolyte layer. On reaching the anode they react with the fuel, releasing the electrons they gained on the cathode side, which can flow back around the external circuit. Developments have also been made for electrolyte materials which conduct protons in addition to oxide ions, such as Ba(Zr/Ce)<sub>1-y</sub>Y<sub>y</sub>O<sub>2-y</sub> (BZCY) [8];

however, this work is relatively new and requires considerably more research before a commercially viable system could be produced.

SOFCs can operate at high efficiencies, in the region of 50%, on a variety of fuels. A significant increase in this efficiency can be reached if the waste heat is also utilised. This makes SOFCs ideal for combining with turbines, or for use in Combined Heat and Power (CHP) systems. As for MCFCs, SOFCs are normally stable in the presence of carbon monoxide and dioxide and do not need to use precious metals as catalysts because of the high operating temperatures. Another similarity to MCFCs is that they can run on a variety of fuels and in most cases can internally reform hydrocarbons. However, there are still many issues to overcome to increase the performance and lifetime of SOFCs. Nickel is often used in the anode as a catalyst and electron conductor, and operates well on pure hydrogen, although when using hydrocarbons as the fuel it has drawbacks. Sulphur is present in most hydrocarbon fuels and this irreversibly binds with the nickel, reducing both catalytic activity and electronic conductivity in the anode, severely affecting performance. In addition, nickel is a catalyst towards the formation of carbon-carbon bonds which can lead to 'coking' at the anode. Coking involves the build-up of carbon on the surface of the anode, blocking the catalytically active sites and disrupting gas transfer, which significantly decreases cell performance, and will be discussed in further detail in Chapter 2

This thesis addresses the material aspects of SOFC systems, concentrating primarily on those which are exposed to reducing environments. The different materials used with SOFCs will also be discussed in Chapter 2.

## **Chapter 2. Solid Oxide Fuel Cell Materials**

There is much ongoing research into materials with potential applications in SOFCs. All materials used within SOFC systems must fulfil certain conditions; for example, the thermal expansion coefficients (TECs) for all materials within a single cell must be close in value, otherwise upon heating different layers would expand at different rates and cause cracking. In addition, chemical compatibility with other components and physical stability at the high operating temperatures is required. The current industry standards for SOFCs along with newer materials with the potential to replace the conventional ones will be discussed here. The aim for this project is to expand knowledge and understanding of current materials alongside the development of newer materials, in order to deliver the potential to overcome many of the issues detailed earlier in this thesis.

Much of the work presented within this thesis focuses on materials with the perovskite structure, general formula  $ABO_{3-x}$ , where A = larger cation, B = smaller cation. This structure was first discovered as adopted by  $CaTiO_3$  by Gustav Rose in 1839, and was named after the Russian scientist Lev Aleksevich von Perovski. The crystal structure was first described by Victor Moritz Goldschmidt in 1926, at which time he also determined an equation for calculating the structural stability of a perovskite material from the atomic radii of the ions involved [9]. This tolerance factor equation can be seen in Equation 2. The structure can be described as consisting of  $BO_6$  octahedra arranged in a corner-sharing arrangement with an A cation situated in the 12-coordination site in the

centre of a cube of 8 such octahedra. Examples of perovskite structures can be seen in Figure 2.

$$t = \frac{r_A + r_O}{\sqrt{2}(r_B + r_O)} \quad (2)$$

*Equation 2. Goldschmidt's tolerance factor calculation for perovskite stability (where  $t$  = tolerance factor,  $r_A/r_B/r_O$  = ionic radius of the A-site/B-site/O-site)*

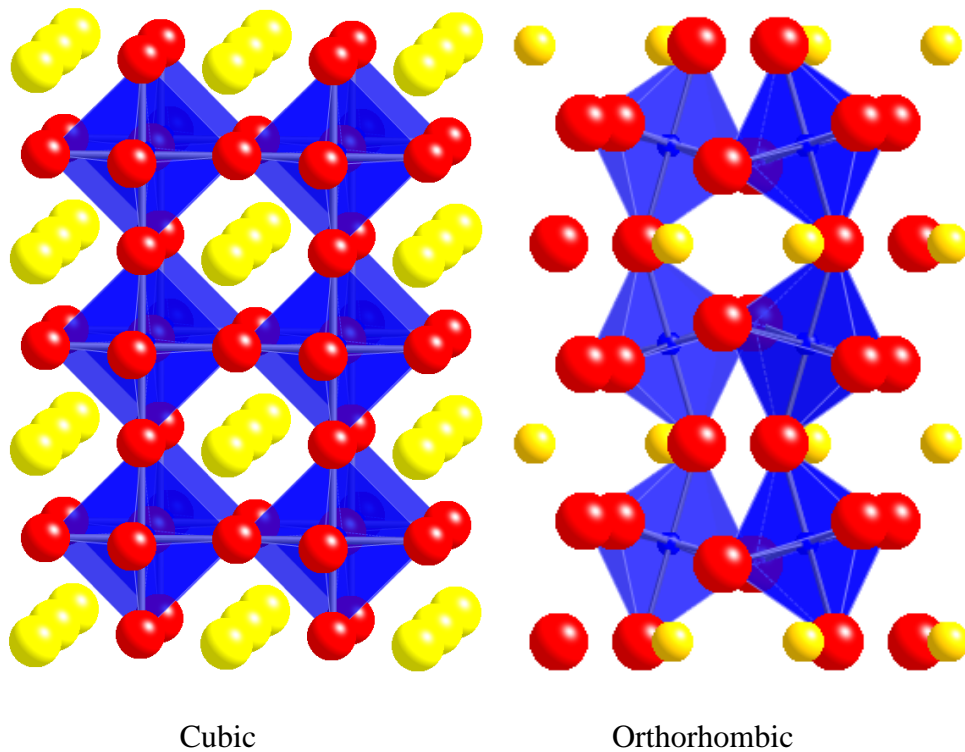


*Figure 2. Cubic and orthorhombic perovskite structures*

The Goldschmidt's tolerance factor allows the prediction of the strain on the unit cell and can also be used to make predictions about the symmetry of the system. An ideal perovskite typically has a large A-site cation paired with a small B-site cation which

gives a tolerance factor as close to 1 as possible, and typically results in a cubic unit cell [10]. A tolerance factor of less than 1, which corresponds to either a smaller A-site cation or a larger B-site cation, typically leads to the need for the octahedra to tilt to aid stability. This often leads to a lower symmetry unit cell, such as orthorhombic, with a value for  $t$  of 0.8 - 0.9. Alternatively, a tolerance factor over 1 might be observed, which is caused by too great a difference in cation size between A-site and B-site, in this case a hexagonal unit cell may result.

In Figure 2 it can clearly be seen that the change in unit cell from cubic to orthorhombic is due to the tilting of the  $\text{BO}_6$  octahedra. This is caused by having an A-site cation which is too small relative to the unit cell size and so the octahedra tilt, which brings additional anions into contact with the A-site cations. The degree of tilting is directly related to the ratio of the size of the A and B site cations as determined by Equation 2, with a tolerance factor closer to 1 displaying a lower degree of tilting.

Since the perovskite unit cell symmetry is highly dependent on the size relationship between the A-site and B-site cations, any changes that may occur through oxidation or reduction may bring about a change in symmetry, leading to a new material with potentially radically different properties. A good example of the different possible phases available for a given family of materials is that of  $\text{SrFeO}_{3-\delta}$  where  $0 \leq \delta \leq 0.5$ .  $\text{SrFeO}_3$  has the perovskite structure with tetragonal symmetry; however, upon heating in a reducing atmosphere it is possible to form the material  $\text{SrFeO}_{2.875}$  (or alternatively  $\text{Sr}_8\text{Fe}_8\text{O}_{23}$ ). In this structure, iron is present as both  $\text{Fe}^{3+}$  and  $\text{Fe}^{4+}$  and the oxygen vacancies order so that a regular pattern of both  $\text{FeO}_6$  octahedra and  $\text{FeO}_5$  square

pyramids form. If reduced further a brownmillerite-type phase,  $\text{SrFeO}_{2.5}$  (or  $\text{Sr}_2\text{Fe}_2\text{O}_5$ ), can be formed in which there are alternate layers of octahedral and tetrahedral Fe [11]. There is also evidence of the formation of other phases based around strontium ferrate, such as  $\text{SrFeO}_{2.75}$  ( $\text{Sr}_4\text{Fe}_4\text{O}_{11}$ ) [12].

## **2.1. Anode Materials**

This thesis focuses mainly on the synthesis and characterisation of materials for use as an anode in SOFCs. The anode of a SOFC is where the electrochemical reaction between the fuel and oxide ions occurs, with the additional strain on an anode-supported fuel cell system of having to provide the mechanical strength as well. The properties must therefore include: high electronic conductivity, good mechanical strength, electrocatalytic activity towards a range of fuels including hydrogen and/or hydrocarbons, tolerance to fuel impurities (such as sulphur); high surface area to allow maximum power densities, stability in reducing atmospheres, and chemical and mechanical compatibility with the electrolyte material used within the cell.

### **2.1.1. Current Material Limitations**

Current commercial anode technologies focus mainly on cermets, a dispersion of metal particles over a matrix of a ceramic. The ceramic is typically the same material as is used in the electrolyte layer, which allows a match in thermal expansion coefficients (TEC) as well as for the layers to bind together. It has been commonplace for many years in high

temperature cells for this cermet to consist of YSZ with nickel nanoparticles dispersed over the surface [13]. The nickel serves to conduct electrons as well as act as a catalyst towards the reaction of hydrogen and hydrocarbons with oxide ions. Between the nickel and YSZ, many of the criteria for an anode material are met [14]. The cermet is typically between 40-60% nickel oxide on manufacture, which reduces to nickel metal under operating conditions.

A cermet contains, by definition, a mixture of metal and ceramic particles. However, as it is uncommon for ceramics to conduct electrons or for elemental metals to conduct ionic species, the ability to fully function as an anode is restricted to those areas where the metals and ceramic are in contact together with fuel. This area is known as the triple phase boundary (TPB), as it involves the interaction of the gases with a solid that transports the ions and a solid that transports the electrons.

As can be seen in Figure 3, the triple phase boundary is the point at which the smaller nickel and larger YSZ particles are touching which is also open to a porous gas channel. As the electrochemical reactions taking place require the presence of electrons, oxide ions and the gaseous fuel, with nickel transporting the electrons and YSZ transporting oxygen ions, these boundaries must be within pores or channels in the material to allow the fuel to come into contact with the ions. This leads to the need for a large surface area combined with the nickel being very well dispersed across the surface of the YSZ ceramic support [15]. However, if the nickel is too widely dispersed then there is little interconnectivity between particles and this leads to a lowering of cell performance due to the raised resistance to electron transport of the anode.

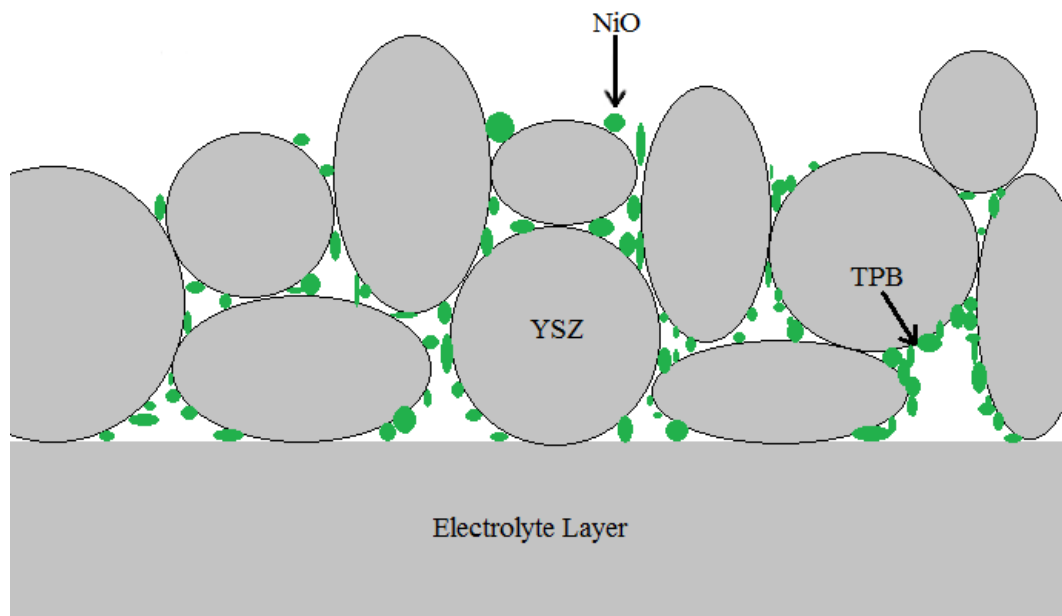
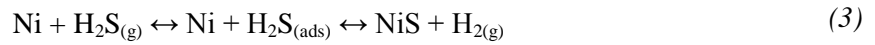


*Figure 3. An example of the triple phase boundary in a SOFC utilising a YSZ/NiO cermet as the anode*

The increase in size of the TPB would be highly desirable as it would increase the available surface for reactions to take place on. This would subsequently have the potential to increase the performance of the cell. However, with investigations into mixed ionic-electronic conductor (MIEC) materials, particle size and porosity become important factors due to not needing a mixed material anode. MIEC material research will be covered in greater depth later in this Chapter.

These nickel/YSZ cermets are typically produced through mixing of nickel oxide with YSZ, either as powders or a slurry. Once the SOFC has been fabricated, the NiO is typically reduced in-situ to the metal as the anode material is exposed to a reducing environment. This also leads to an increase in porosity as this removal of oxygen causes a reduction in density of the material.

However, while these Ni/YSZ cermets have many benefits, they also have many drawbacks which has led to a large wealth of research to be carried out into alternative materials. Most readily accessible hydrocarbons, even after they have been cleaned to remove contaminants or molecules outside of the molecular weight range, still contain traces of pollutants, the most common of which is sulphur in the form H<sub>2</sub>S. Ni-containing cermets can be severely degraded through the use of sulphur-containing fuels due to sulphur poisoning of nickel. The mechanism by which sulphur reacts with nickel and forms an inactive Ni-S species is shown in Equation 3.



*Equation 3. Sulphur poisoning of nickel within SOFC anodes*

Studies have shown that at a concentration as low as 0.05 ppm at a typical SOFC operating temperature of 750°C, YSZ/Ni anodes can be degraded by sulphur, which will lead to a dramatic loss of performance over time, with the effectively-irreversible formation of NiS [16, 17]. Sulphur is typically present in the range of a few ppm in natural gas as delivered to most homes within the UK currently. It is often in the form of methanethiol (CH<sub>3</sub>SH) or tetrahydrothiophene (C<sub>2</sub>H<sub>4</sub>S) which are often added to give the gas supply a smell; methane has no odour otherwise so gas leaks would be very difficult to detect. If the problem of anode poisoning by hydrogen sulphide can be overcome then it will allow SOFCs to be much more easily integrated into the current energy infrastructure.

The drop in performance when exposed to sulphur-containing fuels is not enough by itself to justify such a large quantity of research into anode materials for SOFC. However, in addition to the issues surrounding sulphur, nickel acts as a catalyst towards the formation of carbon-carbon bonds; in fact, it is a widely used catalyst in industry for hydrogenation and reforming. This formation of carbon-carbon bonds causes 'coking' of cells when they are run on hydrocarbons. This coking is a deposition of carbon on the surface of the anode and is particularly problematic when there is little steam present, as the steam acts to oxidise the carbon deposits and so help to remove it. This coking significantly lowers the performance of the cell by reducing the surface area available for reactions to occur [18–20]. Equation 1, Equation 4 and Equation 5 cover both steam and dry reformation and also partial oxidation of methane, the simplest hydrocarbon fuel.



*Equation 4. Partial oxidation of methane*



*Equation 5. Dry reformation of methane*

In addition, formation of carbon deposits on the anode can cause damage to the microstructure of the anode. This may cause the delamination of materials or the formation of microcracks, leading to poorer material interconnections and lowering cell performance. It is possible to determine the nature of the carbon deposited on the cell through temperature programmed oxidation (TPO). This involves subjecting the coked cell to an oxygenating atmosphere and measuring the levels of carbon monoxide and

dioxide being produced (using a mass spectrometer), while raising in temperature. Carbon which is only adsorbed onto the surface (amorphous) will oxidise around 300 °C, whereas graphitic carbon will oxidise at 600 °C [19–22].

The processes involved in both carbon deposition and sulphur poisoning are varied. Layers of both carbon and sulphur have been observed to grow on anode surfaces in a similar fashion as chemical vapour deposition (CVD), for example [23]. Several methods used for reducing poisoning effects (such as increasing steam content at the anodes to allow steam reformation of methane) have significant unwanted side effects (such as difficulties in thermal management due to the endothermic reforming process), further complicating matters. Therefore, much work is ongoing into alternative materials which do not suffer from carbon deposition or sulphur poisoning.

### **2.1.2. Novel Material Research**

Significant research in recent years has focussed on replacing, either fully or to some degree, nickel with copper within cermet systems [24]. Copper has been shown to have the capability to reduce coking when running on hydrocarbons, even when the fuel is dry [25, 26]. However, copper oxide (CuO) has a melting point of 1083 °C, which is far lower than that typically used for the sintering of YSZ. This means that in order to use copper as a catalyst within the anode of an anode-supported SOFC it must either form a part of a cermet which contains a ceramic other than YSZ, which sinters at a temperature lower than 1083 °C, or it must be added to the anode layer once all stages of fabrication which involve temperatures over 1083 °C have been completed. In addition, Cu has a

lower catalytic activity towards the breaking of carbon-carbon and carbon-hydrogen bonds than that of Ni. This lower catalytic activity is the reason behind copper being more resistant to coking; however, it is problematic for operation on hydrocarbons as the efficiency of internal reforming is significantly reduced. This has led to the use of CGO in conjunction with Cu as this also displays some catalytic activity towards the breakdown of hydrocarbons and can be sintered at lower temperatures than YSZ, although this is still problematic [27, 28]. In addition, it has been shown in some recent studies that both YSZ and CGO may be unstable in the presence of copper, leading to a loss in oxide ion conductivity [29].

There is also a great deal of interest in materials based around CGO or utilising a cermet or mixture of CGO and other materials, due to its catalytic activity towards the breakdown of hydrocarbons and the fact that it is a better oxide ion conductor than YSZ [30, 31]. Within the anode, the problems of electronic conduction above 600 °C are no longer an issue as increased electronic conductivity is favourable. Unfortunately CGO is in the region of 3 - 4 times more expensive than YSZ, reducing its appeal.

Investigations into MIEC materials have also been carried out, with many of these being based around the perovskite structure. These typically feature transition metal elements on the B site, usually first row transition elements due to the small size requirements of the site. The use of MIEC materials within the electrodes of SOFCs would potentially bring about a number of improvements over a Ni/YSZ cermet. The simplification of the fabrication process would be advantageous, as additional processing of the nickel oxide and YSZ would be required over a single material, and also because the nickel oxide

used is a suspected carcinogen and so additional safety precautions are required. The conduction of both oxide ions and electrons within MIECs also aids the available area for reactions to occur; the triple phase boundary is extended to any surface of the MIEC material within the porous anode as  $O^{2-}$  can be supplied and electrons removed through the same material. MIEC materials also typically don't suffer from particle agglomeration to the same degree as a NiO system; nickel particles move over the surface of the YSZ (or other oxide ion conductor material) framework over time, leading to reduced surface area and consequently reduced cell performance [32, 33].

In terms of such systems, there is a lot of work focussing on perovskite titanates based around  $SrTiO_3$  which has been known to have potential as an anode material [34]. This compound provides redox stability, even at the high operating temperatures of a SOFC; however, it is very difficult to reduce and this irreducibility also brings with it low electronic conductivity. This can be countered through doping, both on the Sr and Ti sites. However, many of these doped systems struggle with relatively low oxide ion conductivity, in part due to the lack of oxide vacancies even after reduction. Many different variants of this material have been made, with dopants such as Ba, Ca, La, Ni, Mg, Mn, Fe, Cr, In, Sn, Nb [35–39]. However, they largely suffer from the same issue of low oxide ion vacancies and hence oxide ion conductivity. In an attempt to counter this, perovskite materials with A-site deficiencies have been synthesised, for example  $Sr_{1-x/2}Ti_{1-x}Nb_xO_{3-\delta}$  [40–42]. These materials also display increased resistance towards forming Ruddlesden-Popper type impurities (which reduce electrical conductivities) as forming these layers requires an excess of A-site cations [43, 44].

Compounds based around the tungsten bronze structure of  $A_xBO_3$ , where  $x < 1$ , A is usually an alkali or alkaline earth metal cation and B is a large transition metal cation, such as W or Nb, have also been investigated. These are closely related to perovskite systems and incorporate the same  $BX_6$  octahedra with A-site cations occupying interstitial sites. Many variations can be synthesised, such as  $Sr_{0.6}Ti_{0.2}Nb_{0.8}O_{3-\delta}$  and  $Na_{0.8}Nb_yW_{1-y}O_{3-\delta}$ , which can display promising electronic conductivities [45–48]. However, slow oxygen ion transport caused by a diffusion-limited process, combined with possible reactivity with YSZ are problems yet to be overcome.

The synthesis and analysis of A-site deficient perovskite materials, such as  $(La_xSr_{1-x})_{1-y}Cr_{0.5}Mn_{0.5}O_{3-\delta}$  with  $y \leq 0.1$  has shown promise, with good stability shown at high temperature in both oxidising and reducing environments [49, 50]. This series of materials, however, suffers from similar issues to those of the titanates, namely low oxide ion conductivity. In addition, catalytic activity is also low, necessitating the inclusion of additional catalytically active materials. It has been shown that adding 4% Ni to  $La_{0.8}Sr_{0.2}Cr_{0.8}Mn_{0.2}O_{3-\delta}/CGO$  increases cell performance when fuelled by hydrocarbons, without significantly increasing carbon deposition [51]. This lack of increase in coking is thought to be due to the low levels of Ni used. In addition,  $CeO_2$  has been used as an additive with reasonable success [52]. This also displays a better sustained performance when sulphur is present than those with the nickel additive.

Focus has also been placed on the series  $Sr_{1-y}La_yTiO_{3+\delta}$  [35, 53]. This has been shown to display high electronic conductivities, as high as  $100 - 500 \text{ S cm}^{-1}$  between  $700 - 1000 \text{ }^\circ\text{C}$  [54]. However, only low oxide ion conductivities have been achieved without relying on

doping. Mn, Ga, Y, Al, Mg, Fe, Ce and Sc have all been doped onto the B-site and have been shown to increase oxide ion conductivity at the expense of electronic conductivity [54–56]. Study into A-site deficient analogues were been carried out and was also shown to increase the ionic conductivity [41]. More work is required on these systems if they are to be utilised as a composite anode, for example with YSZ, as the electronic conductivity alone is too low to produce an efficient cell.

Other perovskites such as  $\text{Sr}_{1-x}\text{La}_x\text{VO}_3$  have also been investigated. These vanadate perovskites display very high electronic conductivities at higher temperatures [57]. Unfortunately, most are unstable in an oxidising environment, and this coupled with a large volume change on reduction leads to incompatibility with many electrolytes, both conventional and novel, as well as manufacturing difficulties. Mo doped compounds such as  $\text{CaV}_{0.5}\text{Mo}_{0.5}\text{O}_{3-\delta}$  have been shown to have oxidised (a scheelite-type structure) and reduced structures with very similar TECs in addition to high electronic conductivity of over  $500 \text{ S cm}^{-1}$  at  $800 \text{ }^\circ\text{C}$  [58]. Degradation of the material, however, was observed above  $600 \text{ }^\circ\text{C}$ , which may be a result of the presence of calcium on the A-site, as this has previously been observed to increase electronic conductivity at the expense of redox stability [59].

Research on Mo containing anodes has been built upon with studies into the double perovskite  $\text{Sr}_2\text{MgMoO}_6$  and related materials [60–62]. These have the potential to be sulphur tolerant anodes with both high oxide ion and electronic conductivity. They have also been shown to be stable in both oxidising and reducing environments, along with good tolerance to the presence of S. Mo has, however, been shown in some cases to

diffuse into the YSZ electrolyte of the cell, which is detrimental to performance. To counteract this issue, it has been shown that a CeO<sub>2</sub> barrier layer can be successfully employed to prevent this diffusion, albeit at the expense of additional cost and complexity of the cell. The promising results of these molybdates is generating increased interest into this material group.

Oxyanion doping into the perovskite structure is a doping strategy which has recently begun to have a more rigorous examination. Whereas many traditional doping strategies focus on replacing cations with aliovalent alternatives, incorporating oxyanions such as nitrate, sulphate or phosphate has been shown to be possible on the B site within perovskite systems. Through oxyanion doping it is possible to stabilise phases which otherwise would not be stable; for example, Ba<sub>2</sub>In<sub>2-x</sub>P<sub>x</sub>O<sub>5+x</sub> (0.1 ≤ x ≤ 0.3) has increasing cubic structure stability at lower temperatures on increasing levels of phosphate concentration [63–65]. The orthorhombic crystal structure has ordered oxide ion vacancies, as opposed to the disordered vacancies present in cubic structures; typically, ionic conductivity increases with increasing oxide ion disordering. This stabilising of phases can be seen in other ionic conducting solid, such as YSZ, where undoped zirconia undergoes a phase change at a temperature too high to be of use.

The doping of oxyanions onto the B-site of perovskites is also being investigated for use within electrodes of SOFCs. Initial studies based around SrCoO<sub>3-δ</sub> were carried out, involving doping with phosphate, sulphate and silicate [66, 67]. Doping with between 3% - 7% of oxyanion onto the Co site caused a phase change from hexagonal to cubic, subsequently leading to large increases in conductivity. However, further studies on

long-term stability showed that annealing above 600°C caused a gradual phase change back to a hexagonal cell.

Similar investigations into the doping behaviour of the related hexagonal perovskite  $\text{SrMnO}_3$  have also been carried out [68]. Higher levels of dopant were found to be required at around 15%, with only silicate proving possible to stabilise the cubic phase. The incorporation of the  $\text{SiO}_4^{4-}$  anion, which is tetrahedral, in both Co/Mn perovskites at the expense of the B-site cation, which is octahedral, necessitates the formation of oxide ion vacancies, leading to partial reduction of the remaining Co/Mn.

This allows doping with oxyanions to be used as a potential strategy to modify the oxidation states of transition metal cations through oxide ion vacancy creation. This has been demonstrated to be an effective means of improving electrical conductivity, even when no change in cell symmetry is recorded, in the work carried out by Porras et al into doping  $\text{CaMnO}_3$ . In addition, doping with borate was shown to increase conductivity, despite being of lower valence than the Mn it was replacing, which was again attributed to the increase in electron doping through increased oxide ion vacancies outweighing the expected decrease of the smaller charge species. It was not clear whether the boron was present as  $\text{BO}_3^{3-}$  or  $\text{BO}_4^{4-}$ , with further work being required in order to determine the coordination in-situ.

Iron-containing perovskite systems, such as  $\text{SrFe}_{0.75}\text{Mo}_{0.25}\text{O}_{3-y}$  have been investigated in depth [69, 70]. Powder neutron diffraction studies show a tetragonal unit cell, and Mössbauer and XAS studies show that oxidation states are +6 for Mo and +3/+4 for Fe.

This material showed promising regenerative properties to both sulphur poisoning and coking, with the material regenerating on exposure to oxygen at operating conditions. Mo content increases have also been investigated in the series  $\text{SrMo}_{1-x}\text{Fe}_x\text{O}_{3-y}$  (with  $x \leq 0.3$ ) [71, 72]. Fe was doped onto the B site of  $\text{SrMoO}_3$  in an attempt to introduce oxygen vacancies and improve the oxide ion conduction, without compromising the high electronic conduction of the parent material.  $\text{SrMo}_{1-x}\text{Fe}_x\text{O}_{3-y}$  showed promising results when utilised as the anode as part of a SOFC cell (with  $\text{La}_{0.8}\text{Sr}_{0.2}\text{Ga}_{0.83}\text{Mg}_{0.17}\text{O}_{3-\delta}$  (LSGM) as the electrolyte and  $\text{SrCo}_{0.8}\text{Fe}_{0.2}\text{O}_3$  (SCFO) as the cathode), achieving maximum power densities of 870 and 790  $\text{mW cm}^{-2}$  at 850 °C on  $\text{H}_2$  (for  $x = 0.1$  and 0.2 respectively). The thermal expansion coefficients correspond to many widely-used electrolyte materials (in the region of  $11 - 14 \times 10^{-6} \text{ K}^{-1}$ ) and chemical compatibility with LSGM was demonstrated.

Studies into another iron containing system,  $\text{LaSr}_2\text{Fe}_2\text{CrO}_{9-\delta}$  ( $\text{La}_{0.33}\text{Sr}_{0.67}\text{Fe}_{0.67}\text{Cr}_{0.33}\text{O}_{3-\delta}$ ) were undertaken. Cells were fabricated using  $\text{LaSr}_2\text{Fe}_2\text{CrO}_{9-\delta}$ /CGO anode, LSGM electrolyte and LSCF cathode, with a  $\text{La}_{0.4}\text{Ce}_{0.6}\text{O}_{2-\delta}$  (LDC) barrier layer. A maximum current density of  $\sim 400 \text{ mW cm}^{-2}$  was recorded at 800 °C on wet hydrogen, and resistance to sulphur poisoning was displayed at 22 ppm sulphur content. Good redox performance was also noted; however, poor performance on methane indicates a lack of catalytic activity.

## 2.2. Cathode Materials

The requirement for cathodic materials includes those standard to any fuel cell material such as stability at high temperatures and matched TECs, in addition to catalytic activity towards the dissociation of oxygen and electronic conductivity within oxidising conditions. Many of these criteria are met by  $\text{LaMnO}_{3\pm\delta}$  and other perovskite systems containing transition metals, which are widely used in SOFCs [34, 73, 74]. The high electronic conductivity exhibited is a result of the mixed valency of the manganese, present as both  $\text{Mn}^{3+}$  and  $\text{Mn}^{4+}$ . This is further enhanced through doping with alkaline earth cations, most typically strontium, to form  $\text{La}_{1-x}\text{Sr}_x\text{MnO}_{3-\delta}$  (LSM), which shows very high electronic conductivity at the high operating temperatures of SOFC systems [75]. Unfortunately, LSM exhibits relatively low oxide ion conductivity and has been shown to react with YSZ, a common electrolyte material, at elevated temperatures, which leads to an insulating layer preventing oxide ion transportation, reducing the available triple phase boundary area and lowering the performance of the cell [76]. Other related perovskite systems such as  $\text{La}_{0.6}\text{Sr}_{0.4}\text{FeO}_{3-\delta}$  (LSF) have also been studied in detail, and were found to have favourable ionic and electronic conductivity alongside good thermal expansion and chemical compatibility with both YSZ and CGO [77, 78]. Further work on these systems has been carried out leading to interest in  $(\text{La/Sr})_{1-x}\text{Cr}_y\text{Mn}_{1-y}\text{O}_{3-\delta}$  (LSCM) and  $(\text{La/Sr})_{1-x}\text{Co}_y\text{Fe}_{1-y}\text{O}_{3-\delta}$  (LSCF) with  $x \leq 0.1$  for use at high and intermediate temperatures respectively [79–81].

Research into potential new cathode materials has been focussed on improving upon several well-defined structure types:

1. Pyrochlores such as  $R_2MnRuO_7$  (where  $R = Tb, Dy, Ho, Er, Tm, Yb, Lu$  and  $Y$ ), feature good catalytic activity towards dissociation of oxygen combined with low area specific resistance [82]. These have been investigated for use in both cathodic and anodic conditions; for example,  $Gd_2Ti_{1.4}Mo_{0.6}O_{7-\delta}$  has been shown to be a sulphur-tolerant anode, by being able to operate on 10%  $H_2S$  in  $H_2$  without suffering from significant degradation [83, 84]. However, these materials generally contain rare earth or noble metals and so are hampered by high costs.
2. Layered double perovskites of the general formula  $AA'BB'O_6$ , where  $A$  and  $A'$  and  $B$  and  $B'$  are in alternate layers, such as  $(Gd/Pr)BaCo_2O_{5+\delta}$  [85–87]. These often feature high electrical and ionic conductivity at operating temperatures for SOFC, however high activation energies reduce effectiveness at the lower end of the operating temperature spectrum [88].
3. Ruddlesden-Popper type materials;  $A_{n+1}M_nO_{3n+1}$  with  $A =$  alkaline or rare earth,  $M =$  transition metal such as  $La_{n+1}Ni_nO_{3n+1}$  ( $n = 1, 2$  and  $3$ ) [89, 90]. Originally reported for  $Sr_{n+1}Ti_nO_{3n+1}$ , these often contain a wide range of elements and feature alternating blocks of perovskite and rock salt structures. They have similar positive and negative characteristics to many novel perovskite structure materials, namely high ionic and electronic conduction but with some chemical reactions occurring between the cathode and electrolyte materials [89, 91].
4. Other perovskite types: there are several different perovskite structures which appear promising, including variations around  $LaNi_{1-x}Fe_xO_3$  (LNF) and  $Ba_{0.5}Sr_{0.5}Co_{0.8}Fe_{0.2}O_{3-\delta}$  (BSCF) amongst others [92–97]. Characteristics vary, but often include high ionic and/or electronic conductivity at the expense of some reactivity with common electrolyte materials.

Significant research has been put into cathode materials and while there are still challenges to be overcome, great leaps forward have been made over the past few decades with several materials well established for commercial use. This has not stopped work being carried out into novel materials and of course the use of novel electrolytes within cells, particularly IT-SOFCs, brings about a range of new issues such as chemical compatibility and performance under different operating conditions.

### **2.3. Electrolyte Materials**

Materials used as electrolytes in SOFCs must adhere to a range of characteristics, including but not limited to: high degree of sintering to allow formation of gas-tight, thin layers; high oxide ion conductivities; very low electronic conductivities; chemical and thermal stability at operating temperatures in both reducing and oxidising conditions.

Currently, the majority of these characteristics are met by certain ceramics of the fluorite or perovskite structure. The most common two materials in use within SOFCs are stabilised zirconia and stabilised ceria. These are generally in the form of yttria-stabilised zirconia (YSZ, fluorite-type structure) and gadolinia-doped ceria (GDC, also often referred to as cerium-gadolinium oxide (CGO), fluorite-type structure). YSZ has high oxide ion conductivity at temperatures over 800 °C, combined with excellent thermal and chemical stabilities [98, 99]. It is also available at low cost and is already manufactured on an industrial scale for use within oxygen sensors. However, the high temperature required to reach adequate oxide ion conduction is a potential issue for SOFC durability

and has spurred research into alternative materials for use within intermediate temperature SOFCs (IT-SOFCs). In the temperature region of 500-600 °C, GDC is preferred as it has a similar conductivity to YSZ at 800 °C [30]. Above 600 °C in reducing conditions, the  $\text{Ce}^{4+}$  is partially reduced to  $\text{Ce}^{3+}$  which reduces cell efficiencies by allowing electronic conduction. Therefore the choice of conventional electrolyte material is dependent on the temperature bracket for which the cell is designed. Ceria may be doped with other rare earth metals to similar effect, as in samaria-doped ceria (SDC).

A range of other perovskite materials for SOFC electrolyte use have also been developed. One particularly interesting series is  $\text{La}_{1-x}\text{Sr}_x\text{Ga}_{0.8}\text{Mg}_{0.2}\text{O}_{3-\delta}$  (LSGM) where  $x$  typically = 0.1 or 0.2, which has been extensively studied and used as a basis for many other alternative systems [100]. LSGM displays a high oxide ion conductivity of  $\sim 0.14 \text{ S cm}^{-1}$  at 800 °C which is better than YSZ under the same conditions [101, 102]. However, while this family of materials are generally chemically compatible with LSM, NiO in the anode tends to react with LSGM during fabrication, forming  $\text{LaNiO}_3$  which can block oxide ion transfer [103].

The wealth of research carried out into both perovskite (such as  $\text{BaCeO}_3$ ) and fluorite (such as YSZ) structured materials for use as electrolytes in SOFCs has led to both effectively reaching their maximum potential with little room for improvement [104], and much current research is focused on optimising deposition techniques and microstructural advances, in addition to investigations into the chemical compatibility with novel electrode materials [105–112]. However, this has not prevented research into

other structure types in order to continue the pursuit of increased performance. Novel structures investigated include:

1. Apatite-type materials: general formula of  $(\text{Ln}/\text{A})_{10}\text{M}_6\text{O}_{26+y}$  with Ln = rare earth, A = alkaline earth, M = Si or Ge [113–115]. This family of materials typically shows good oxide conductivity with negligible electronic conductivity. Further research is being conducted with the aim of promoting the inclusion of Si over Ge for cost reasons and to overcome potential chemical compatibility and sintering issues [116].
2.  $\text{La}_2\text{Mo}_2\text{O}_9$ : shows very high oxide conductivities above the phase-transition point of  $\sim 580^\circ\text{C}$  [117]. Work is continuing to synthesise a sample with high conductivity at lower temperature, mainly through doping with the aim of lowering the phase transition temperature [118].

## 2.4. Project Aims

The process of research into novel materials for use within SOFCs involves synthesis of a large volume of materials, with subsequent dismissal of further research into certain material groups. A variety of reasons may be the cause of abandoning research into specific materials, such as impurities being present (from reagents not being fully incorporated into the structure, for example), difficulties in sintering, poor electronic or oxide ion conductivity and redox instabilities. Many of these issues are indicative of greater problems such as poor mechanical strength or low performance as part of a fuel cell.

The work within this thesis aims to synthesise and characterise novel materials, largely focussed on materials with the perovskite structure. These are based around existing systems, with the aim of improving stability and performance in reducing environments. To this end, the synthesis and characterisation of novel perovskite materials was carried out, with the goal of utilisation as an anode material within a solid oxide fuel cell.

## **Chapter 3. Experimental Techniques**

In this Chapter, a description of the main experimental techniques used within this thesis will be presented, to include the underlying theory that underpins their function and the way in which they have been used to obtain data for this thesis.

### **3.1. Synthesis Techniques**

This section covers a range of techniques suitable for use in synthesising metallic oxide ceramics.

#### **3.1.1. Solid State Synthesis**

Solid state synthesis is one of the most widely used synthesis routes within materials chemistry. It involves precursor materials, typically metal oxides/nitrates/carbonates being combined in the correct stoichiometric quantities and then intimately mixed. Combined powders may be ground by hand, or a mechanical mill (such as a vibromill, planetary ball mill, etc) may be used to ensure more complete mixing. This mixture is then placed in a crucible within a furnace and heated, typically to temperatures of 800 °C or more, for periods of 12 hours or longer. This high temperature and long duration is required to allow the new material to be formed through the breaking of the bonds within the original materials and the migration of ions to new positions in the product. The

process of grinding and then reheating is repeated, usually with analysis by X-ray diffraction between repeats to determine if the material has reached a single phase. While simple to perform, the long reaction times and high temperatures required for the diffusion of ions over a long distance can be disadvantageous, as can the lack of control over microstructure and particle size.

### **3.1.2. Co-Precipitation**

Co-precipitation involves creating a solution of metal cations with the correct elemental composition for the desired material. This is typically achieved through using stoichiometric quantities of metal nitrates dissolved to form an aqueous solution. A precipitating agent is then added to the solution, causing a solid product to form. The precipitating agents used vary widely but are often strong acids or alkalis. The solution can then be filtered, leaving the solid precursor to the final product which is usually formed through heat treatment. The temperature, concentration and pH of the solution must be carefully controlled in order for the results to be as intended.

The advantages of this technique include the atomic level mixing of reagents which affords a much faster route to phase purity than solid state synthesis, along with lower temperatures required. However, it is more labour intensive and requires more equipment than solid state synthesis which is an important consideration for shared laboratory space. Initial material costs are also often higher which is particularly detrimental if performing speculative synthesis. In addition, if the rates of precipitation of components are different then a non-homogeneous mixture will result.

### **3.1.3. Sol-Gel**

Sol-gel synthesis again involves the creation of a solution containing metal cations in the correct stoichiometric quantities. Typically metal nitrates are added to deionised water and heated to aid dissolution. Chemicals are then added to promote the formation of an organo-metallic polymer; typically ethylene glycol and citric acid are used [119]. A range of different ratios of ethylene glycol and citric acid have been reported as being effective, with no definitive standard quantity universally used [120, 121]. The mixture is then heated, evaporating water until a gel is formed. This gel is then heated in a furnace to burn off the organic material, leaving a mixed metal oxide. The temperature required for full organics removal typically range around 600 °C and care must be taken during the heating process so that the remaining water does not evaporate too rapidly and cause the mixture to overflow the reaction chamber.

Once again there are similarities to co-precipitation in terms of advantages and disadvantages against solid state synthesis, including lower synthesis temperatures and mixing of reagents at an atomic level, coupled against higher reagent costs and increased labour intensity.

### **3.1.4. Hydrothermal synthesis**

Hydrothermal synthesis involves utilisation of an autoclave (a pressurised reaction vessel), typically stainless steel, which must be completely inert to the chemicals

involved in the reaction. The reaction mixture contains water and usually a strong acid to aid dissolution of the reagents used. The reagents used are dissolved into the solution and heated to the temperature required for the reaction to occur, above 100 °C to increase the vapour pressure inside the vessel but typically under 250 °C. This combination of supercritical water, high pressure and aggressive pH raise the solubility of many materials, allowing the use of reagents which would normally not be water soluble.

Hydrothermal synthesis uses much lower temperatures than solid state synthesis, and similarly to both co-precipitation and sol-gel synthesis the reagents are mixed at an atomic level, which affords a much faster route to phase purity. The size and shape of the products can also be controlled through varying the temperature, pressure and duration of the reaction.

However, the reagents can be more expensive and, in some cases unavailable, making this synthesis route suitable only in some cases. In addition it may be necessary to optimise reaction conditions for every reaction to be carried out, with different conditions leading to different product structures. It is also more equipment heavy, requiring an autoclave and heater per reaction which are considerably more expensive than the crucibles used in the solid state method. In addition, it cannot be used to synthesise products that are unstable in the hydrothermal conditions used. Hydrothermal synthesis is often utilised in growing single crystals of materials, and forming porous structures such as zeolites which cannot be obtained by other means.

Within this thesis only solid state synthesis was used. Powders were weighed out using an analytical balance accurate to  $\pm 0.1$  mg. A planetary mill (Fritsch Pulverisette 7) was used for grinding powders, with alumina crucibles used as reaction vessels.

### **3.2. Pellet Production for Conductivity and Dilatometry Experiments**

Pellets of synthesised materials were formed through using a pellet press. This involves using mechanical or hydraulic pressure to compress powder into a pellet within a die set. The pressure required to form a pellet of sufficient mechanical strength to allow it to be moved without damage depends on the properties of the materials used, including but not limited to: particle size, moisture levels and material adhesion. In addition, binding agents such as stearic acid, polyvinyl alcohol (PVA) and ethanol can be used to assist pellet formation.

Once formed, pellets are placed into a furnace and heated to the desired temperature, typically above 1000 °C. This has the effect of sintering together the particles which form the pellet, increasing the density of the pellet and affording it much greater mechanical strength.

Within this thesis, pellets were pressed using a manual hydraulic press, dies of between 8mm and 22mm diameter and pressures of up to 10 tons.

### 3.3. X-Ray Diffraction (XRD)

X-ray diffraction is a technique used for the analysis of crystalline structures which has the capability to determine the dimensions of the unit cell and the crystal structure, and so can give insights into the ordering of atoms within the structure.

X-rays are produced through bombardment of a metal target with electrons that have been accelerated through a high voltage, typically around 40kV. This radiation is powerful enough to eject core electrons from the metal, leaving a void in the core K (1s orbital) shell. An electron from a higher energy shell, either the L (2p orbital) or M (3p orbital), drops down to fill this void, and in doing so emits a photon of electromagnetic radiation. As the hole which is filled is in the K-shell, this type of X-ray is called K-radiation. The energy, and therefore the wavelength of the emitted electromagnetic ray, is dependent on which shell the electron originates from;  $K_{\alpha}$  is produced by an electron from the L-shell and  $K_{\beta}$  is a product of an electron from the M-shell. Spin multiplicity causes these peaks to be split in two, forming the  $K_{\alpha 1}$  and  $K_{\alpha 2}$  peaks. In an attempt to use only a single wavelength of radiation and so simplify the spectra obtained, filters are used to block out the  $K_{\beta}$ ; in the case of the most common target metal copper, this filter is made of nickel. In addition, monochromators can also be used, which can remove the  $K_{\alpha 2}$  peak, leading to a single wavelength, i.e. the  $K_{\alpha 1}$  X-ray.

X-rays typically have a wavelength of around  $1 \times 10^{-10}$  m or 1 Å, which is in the same region as interatomic distances in crystal structures. This similarity causes the X-rays to be diffracted when passing through the solid, with the diffraction angle related to the

distance between the lattice planes involved which is quantified by Bragg's law (see Equation 6 and Figure 4).

$$n\lambda = 2d \sin \theta \quad (6)$$

Equation 6. Bragg's law, where  $n$  = integer,  $d$  = crystal plane spacing,  $\lambda$  = wavelength of X-rays used and  $\theta$  = angle of the X-rays in relation to the plane

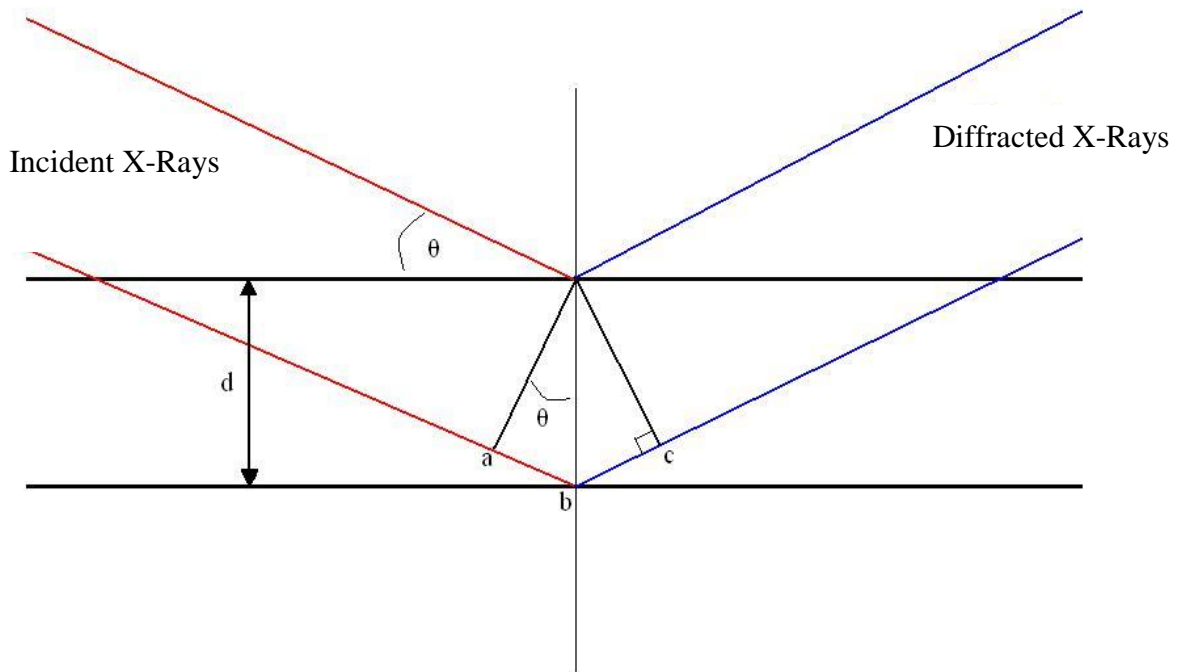


Figure 4. Two crystal planes with spacing 'd' showing reflection of X-rays

In order for peaks to be measured, constructive interference must occur. The extra distance travelled by the X-ray diffracted by the second plane in relation to the first plane must be a whole number of wavelengths larger; i.e.  $(\vec{abc}) = n\lambda$  where  $n$  = integer. Ideally for XRD, a single crystal would be analysed. However, it is often not possible to create a

single crystal of a material for study so powders are commonly be used. Powder XRD was developed for this very reason, and though it is not as powerful as single crystal XRD for structural determination, providing a starting model is available it can still be used to determine a crystal structure.

There are 2 commonly-used instrument orientations used in powder diffraction, which have different capabilities although the diffraction pattern obtained is analysed using the same techniques. Typically, 0.5 g of powder sample is typically required in order to record a diffraction pattern at a large enough intensity in reflection mode (Bragg-Brentano). However, smaller quantities of samples may be analysed in transmission mode (Debye-Scherrer). In order to get the data as uniform as possible, the sample is usually spun; this also assists in trying to capture the maximum number of orientations. The reflected X-rays occur at an angle of two theta ( $2\theta$ ) to the incident rays. With both transmission and reflection geometries, the sample along with the X-ray beam and detector must move relative to each other to preserve focussing and allow intensities at a range of  $2\theta$  values to be recorded. The data recorded can then be compared to XRD patterns stored in a crystallography database in order to assist in characterising the material and determine whether there are any impurities.

For perovskite materials, particularly cubic perovskites, the XRD pattern recorded is usually very simple for a phase pure material. The peaks are typically very clearly defined with no shoulders which makes analysis straightforward.

All data within this thesis were acquired on either a Bruker D8 or a D5005 utilising a copper target. The X-rays used for analysis are Cu  $K_{\alpha 1}$  ( $\lambda = 1.5406 \text{ \AA}$ ) for the D5005 and Cu  $K_{\alpha}$  ( $\lambda = 1.5418 \text{ \AA}$ ) for the D8 diffractometer.

### **3.4. Crystal Symmetry**

There are two different general types of solid; amorphous and crystalline. Amorphous solids have no long range order, with atoms and ions arranged randomly throughout, in comparison with crystalline solids which comprise of a regular lattice of atoms/ions forming the structure. The smallest section of these crystalline materials that can be used to replicate the entire lattice is referred to as the unit cell.

Although there are a wide range of potential arrangements of atoms or ions within crystal structures, every single type of unit cell can be described as one of the 14 Bravais lattices. Within this group there are 7 different crystal class types of varying dimensions. Each of these has at least one of the following sub-types, depending on the arrangement of the lattice: primitive (P), body-centred (I), face-centred (F) or base (C). The full arrangement of all 14 Bravais lattices and the 7 crystal classes can be seen in Figure 5 and Table 1.

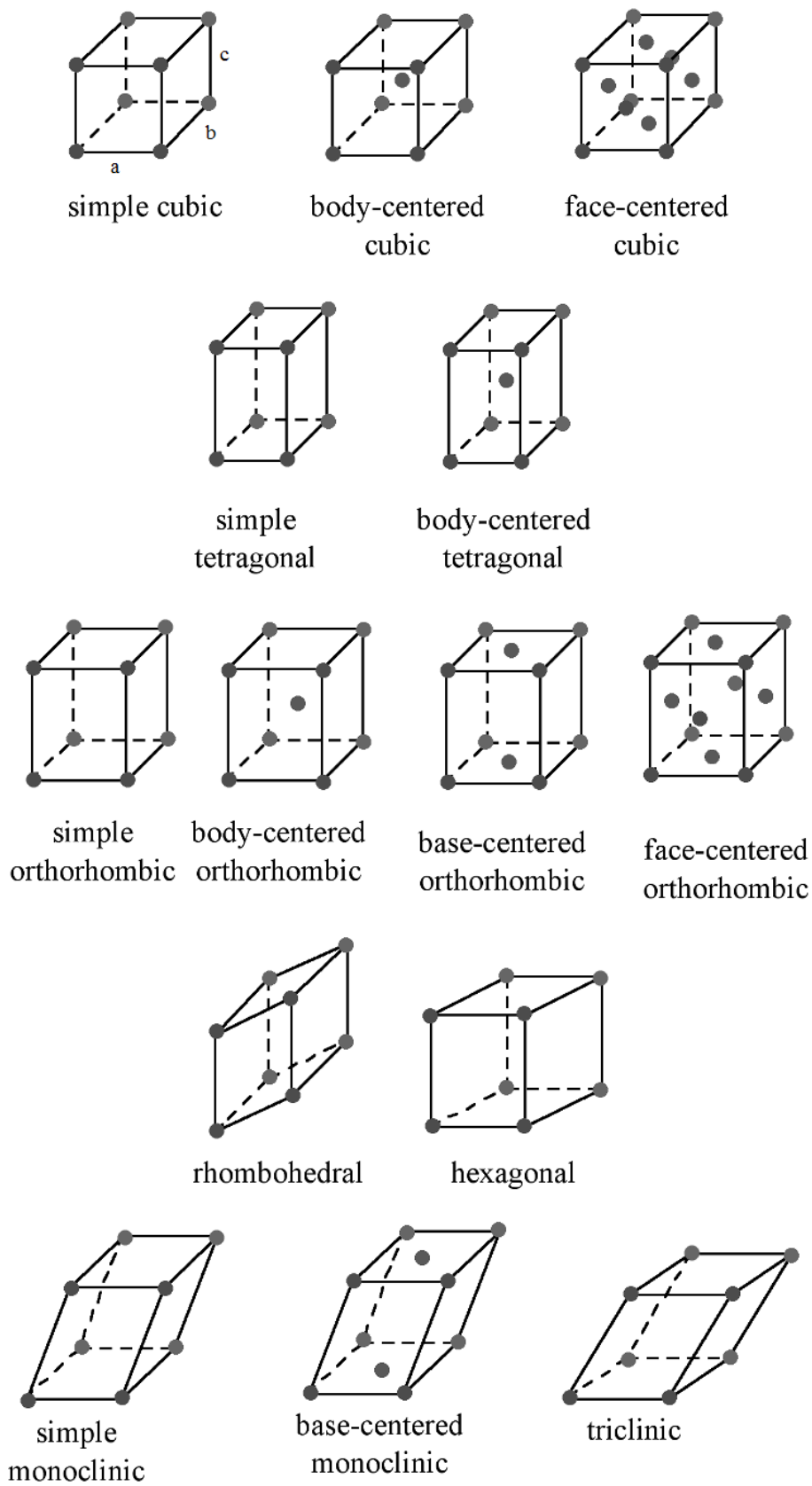


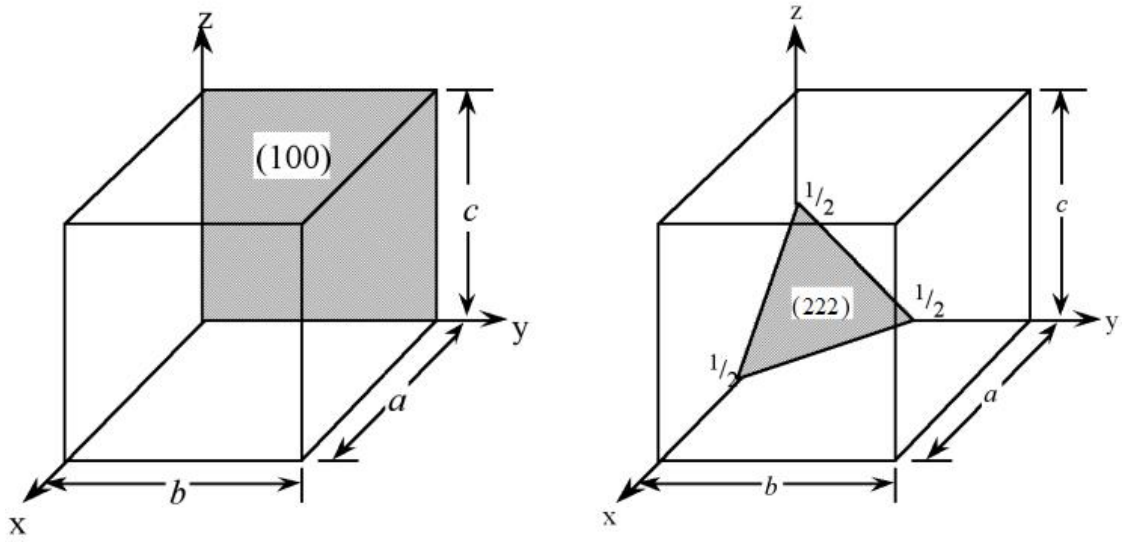
Figure 5. The 14 Bravais lattice unit cell types [106]

Symmetry	Side lengths	Bond angles
cubic	$a = b = c$	$\alpha = \beta = \gamma = 90^\circ$
tetragonal	$a = b \neq c$	$\alpha = \beta = \gamma = 90^\circ$
orthorhombic	$a \neq b \neq c$	$\alpha = \beta = \gamma = 90^\circ$
trigonal/rhombohedral	$a = b = c$	$\alpha = \beta = \gamma \neq 90^\circ$
hexagonal	$a = b \neq c$	$\alpha = \beta = 120^\circ \gamma = 90^\circ$
monoclinic	$a \neq b \neq c$	$\alpha = \gamma = 90^\circ \neq \beta \neq 90^\circ$
triclinic	$a \neq b \neq c$	$\alpha \neq \beta \neq \gamma \neq 90^\circ$

*Table 1. Unit cell symmetries, side lengths and angles*

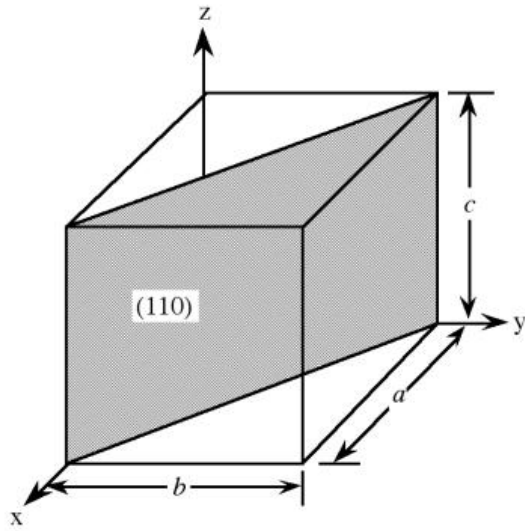
Miller Indices are used to describe lattice planes in crystal structures. These are determined using notation involving 3 integers,  $h$ ,  $k$  and  $l$ , which represent directions from the unit cell origin. These Miller Indices can be used to accurately describe a plane within a unit cell, as can be seen in Figure 6.

The position of atoms/ions within a unit cell are denoted as  $(x,y,z)$ . For example, within a perovskite unit cell the A cation can be described using the value of  $(0.5,0.5,0.5)$  as it sits within the centre of the unit cell, half way along each of the  $x$ ,  $y$  and  $z$  axes.



$$\begin{array}{ccc}
 h & k & l \\
 \frac{1}{1}, \frac{1}{\infty}, \frac{1}{\infty} & = & (100)
 \end{array}$$

$$\begin{array}{ccc}
 h & k & l \\
 \frac{1}{1/2}, \frac{1}{1/2}, \frac{1}{1/2} & = & (222)
 \end{array}$$



$$\begin{array}{ccc}
 h & k & l \\
 \frac{1}{1}, \frac{1}{1}, \frac{1}{\infty} & = & (110)
 \end{array}$$

Figure 6. Miller Indices for several lattice planes [106]

### **3.5. Point Groups and Space Groups**

The symmetry within a unit cell can additionally be described through the use of point groups and space groups. Point groups assign a single point to remain fixed in which the cell is reflected or rotated around (either proper or improper rotation), referred to as an operation. There are 32 different point groups, describing the rotation or reflection symmetry of the crystal structure. Space groups expand on this and combine the point groups with Bravais lattices and include screw axis and glide plane symmetry operations. This provides a total of 230 space groups which describe all possible crystal symmetries.

### **3.6. Rietveld Refinement**

The structural analysis of crystalline materials through XRD is effective only if there is a suitable technique for analysing the results. Traditionally this meant that only high symmetry samples could be studied in detail as otherwise multiple overlapping peaks made the determination of peak intensities impossible. In addition, the shape of the peak is important; the peak area (area underneath the peak, or integral intensity) gives a true measurement of peak intensity, with the width relating to strain or disorder within the crystal structure.

In an attempt to resolve this and allow more complex structures to be resolved, Hugo Rietveld began using computers to analyse XRD data by calculating a model which fits the observed data most closely [122]. This was achieved through using least square refinements until the model and observed data correlated. This was achieved through

using individual data points, rather than peak intensities, and performing least square refinements until the model most closely matched the observed data. A model provides data, with the least square method altering the model by changing selected parameters in order to reduce the sum of the squared residual differences between the model data and the observed values. The model is then further optimised until there is a strong degree of correlation between calculated and observed data. Rietveld refinement is now a widely used method for structural refinement and can be applied to a wide range of materials.

Over the years, many different computer programs have been developed which make it possible to carry out Rietveld refinements from diffraction data. Some of these are relatively simple, open-source programs while others allow more complex data analysis. Within this thesis the GSAS suite of software is used to identify structural characteristics of materials [123, 124].

For Rietveld refinement to be carried out, some information about the system must be known. Atom positions, cell parameters and space group are required, as well as the wavelength of the X-rays used to acquire the data. The atomic positions and cell parameters can then be refined during the analysis process in order to more accurately match the observed pattern and so more accurately determine the structure. During the analysis it is also possible to vary a range of other parameters to better fit the observed data, such as peak shapes, atomic thermal displacement values, scale factors and atomic occupancy.

Once all data has been input and the observed pattern is in place, it is possible for a calculated pattern to be generated. Altering parameters alters the calculated pattern, which can be compared with the observed data as in Figure 7. It is then possible to display the difference between the two diffraction patterns which will help to identify how good a fit the model is to the actual structure.

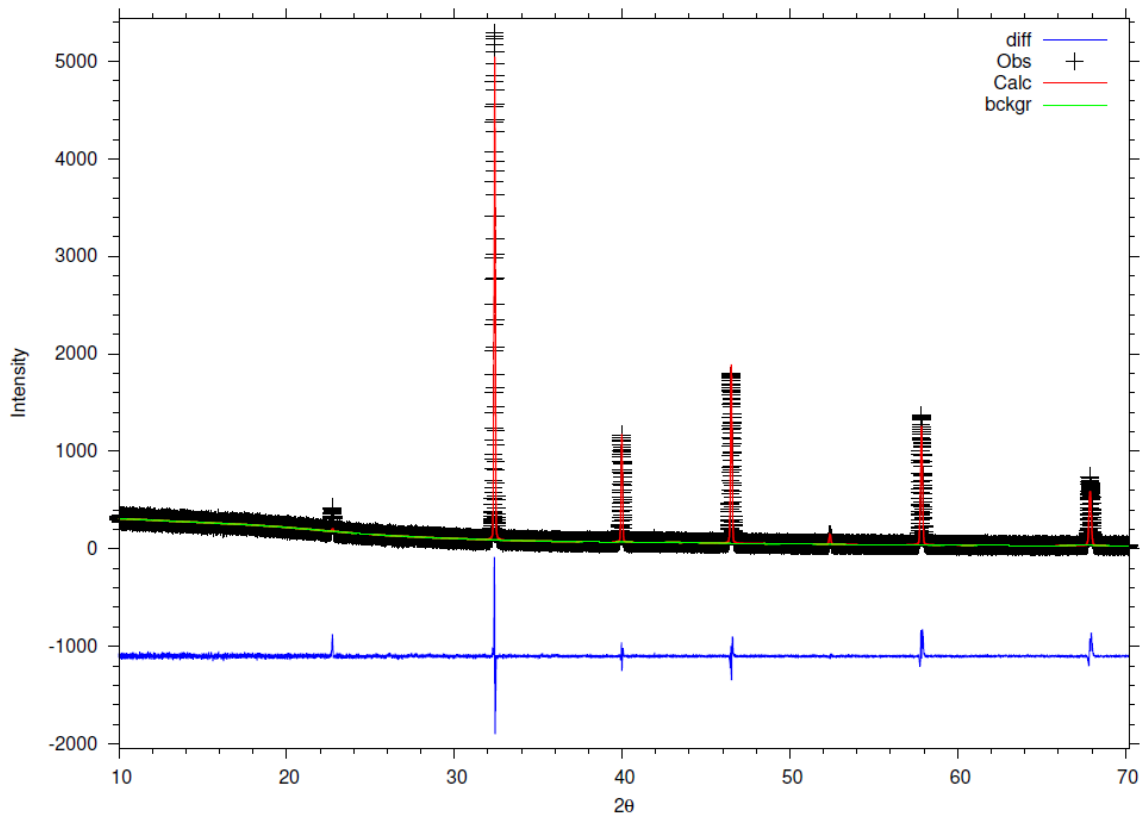


*Figure 7. Diffraction pattern undergoing refinement using the GSAS suite*

It should be noted that the requirement of a reasonably accurate starting structural model means that it is not possible to use the Rietveld analysis technique on samples of unknown structure.

### **3.7. Thermogravimetric Analysis coupled to Mass Spectrometry (TGA-MS)**

Thermogravimetric analysis (TGA) involves investigating the relationship of a change of weight in a sample to the change in temperature. TGA can be coupled with Mass Spectrometry (MS) which is used to analyse any exhaust gases from the sample and determine their composition. This is combined with the data from the mass loss to work out exactly what is lost from a sample, at what temperature and in what amount.

In TGA, a sample is loaded onto a precise balance within a furnace. The temperature is increased in line with a profile defined by the operator, with the process being carried out in either air, H<sub>2</sub> or an inert gas. The TGA-MS equipment used within this thesis was manufactured by Netzsch, with the TGA being model number STA 449 F1 and the MS being QMS 403 C. This equipment is coupled, in this case, to a MS setup which analyses the exhaust gases from the furnace in real time, allowing the gain or loss of weight to be linked to the change in exhaust output. This leads to identification of chemical changes which are tied to specific temperature changes.

Mass spectrometry (MS) involves the ionisation of a sample which is then analysed to determine the mass to charge ratio. In the case of TGA-MS, the exhaust gas is analysed, so the sample has already been vaporised. Any molecules are ionised before being accelerated by an electric field. They are then analysed by a mass analyser to determine mass to charge ratio and then pass onto a detector which analyses the quantity of each ionic species present.

The combination of both TGA and MS into a single technique allows for the analysis of exactly what is being released by a sample at different temperatures, and in what quantities. This can lead to a better understanding of phase changes, chemical and thermal stabilities of samples, and hence allow for changes to be made to improve properties.

The weight, temperature and change in both must be monitored very carefully during the analysis period. TGA-MS can be used to analyse a range of materials, from organic to inorganic, complex to simple. In this thesis, the use will be focused on determining oxygen content within ceramic powders. This was carried out in an inert gas flow or in 5% $H_2/N_2$  in order to reduce the oxygen content, and from the mass loss observed determine the original oxygen content. This use of the TGA doesn't require analysis by MS, so no mass spectrometry data will be presented.

### **3.8. Dilatometry**

Dilatometry is the determination of the expansion of a material with regards to temperature. The majority of materials expand when heated and by using a dilatometer this expansion can be measured and so the thermal expansion coefficient (TEC) can be calculated. There are there are several obvious examples of the use of dilatometry such as mercury thermometers.

For research purposes one of the most common dilatometer configurations is to have a highly sensitive pushrod encased within a furnace. As the furnace increases in

temperature the change in sample length is measured and from this the TEC can be calculated, as in Equation 7 below [125]. Dilatometers may also be configured so as to allow samples to be heated in atmospheres other than air, such as hydrogen or argon, in order to observe different material TEC properties in different conditions.

$$a = \frac{L_f - L_i}{L_i(T_f - T_i)} \quad (7)$$

*Equation 7. Expression for calculation of linear thermal expansion coefficients, where  $a$  = TEC,  $L_i$  = initial length,  $L_f$  = final length,  $T_i$  = initial length and  $T_f$  = final length*

Thermal expansion of materials occurs due to the increase in average bond lengths between atoms within a structure at increasing temperatures. For materials of different chemical structures, the overall expansion coefficient can be expressed as the sum of the different components of the content of the structure, weighted for the angle of the bonds in relation to their relative position within the crystal lattice. For example, the rock salt structure has identical bonds all at 90° to each other so the increase in lattice size in any one plane is equal to the increase in the bond in that direction, whereas the perovskite structure has bonds at angles not equal to 90° of each other and so the increase in lattice size in any one plane is a composite of the components in that directional plane.

Within SOFCs, the TEC of materials used is a very important consideration. Ideally, all TEC values for all materials used should be similar for any temperatures the cell may experience; in the case of SOFCs that range can be between 0 - 1000 °C. As the range is so large, differences in TEC are magnified over the whole temperature band so large

differences cannot be tolerated by the cell. If TEC values for materials in contact with one another are widely different then, upon heating, cracks may form or delamination may occur, which would at the very least cause the cell to become less efficient and at worse may cause the cell to cease functioning and become a hazard, especially if the anode and cathode gases are allowed to mix. It is for this reason that, wherever possible, TECs of materials must be analysed to confirm material compatibility.

Within this thesis, dilatometry measurements were carried out using a Netzsch 409C dilatometer running on a profile from 25 to 1000 °C at 15 °C min<sup>-1</sup>. Samples were prepared by ball milling powders (Fritsch Pulverisette 7 Planetary Mill for 1 hour at 350 rpm) before being pressed into thick pellets of 10 mm diameter and approximately 10 mm length. These were sintered at temperatures relevant to the material being analysed before being polished and having their length measured accurately using digital callipers (accurate to ±0.01 mm).

### **3.9. Electrical Testing**

A variety of electrical testing methods were employed to determine the electrical properties of the materials and cells produced within this thesis, and are covered in detail below.

### 3.9.1. Four Probe D. C. Conductivity

The electrical conductivity of a material is an important characteristic for any fuel cell material. The electrolyte layer requires a material that has little to no electronic conductivity, whereas electrode materials benefit from high electronic conductivity. There are several methods for quantifying the conductivity of materials, and within this thesis, 4 probe DC conductivity was used as it is relatively straightforward to carry out and is suitable for analysis of electrode materials.

Analysis is carried out by attaching electrodes to a sintered dense pellet or strip in the configuration seen in Figure 8. Current is passed across the outer electrodes (1 and 4), with the difference in voltage between the inner two electrodes (2 and 3) measured. From this it is possible to calculate the resistance, which can then be used to calculate the sample conductivity. The equations involved can be seen in Equation 8.

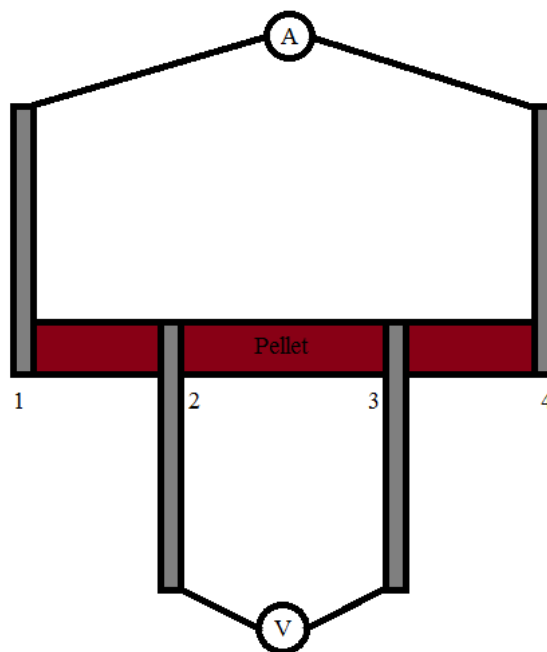


*Figure 8. Electrode configuration for 4-probe DC conductivity*

$$\sigma = \frac{L}{A} \times \frac{I}{V} \quad (8)$$

*Equation 8. Calculation for 4 probe DC conductivity (where  $\sigma$  = conductivity,  $L$  = distance between electrodes 2 and 3,  $A$  = pellet cross-sectional area,  $I$  = current passed between electrodes 1 and 4,  $V$  = voltage difference between electrodes 2 and 3)*

4 probe DC conductivity is a useful technique for determining the conductivity of samples with relatively low resistivities. As such, it is not suitable for analysis of electrolyte materials with high resistivities; these would better be analysed using techniques which allow more accurate determination of higher resistivities, such as AC impedance spectroscopy. While there are other variations of 4 probe DC conductivity (such as Van de Pauw), work within this thesis was carried out using the method outlined above, as previous work on similar materials in both pellet and strip configurations had shown little variation between different techniques and so the simpler technique was utilised [126].

### **3.9.2. Electrochemical Impedance Spectroscopy (EIS)**

Electrochemical impedance spectroscopy can be used to determine the behaviour of electrode or electrolyte materials. This will be discussed within this thesis primarily as AC impedance conductivity and also area specific resistance. The two techniques are closely related, sharing many similar characteristics.

### 3.9.2.1. AC Impedance Spectroscopy

AC impedance spectroscopy is used within SOFC material testing to provide information on oxide ion conductivity. It involves passing an alternating current voltage across a sample and measuring the resulting current response. If the voltage passed across the sample is sinusoidal, the current response will also be sinusoidal, and typically the input and response will be out of phase. Expressions for a sinusoidal voltage and the phase shift between input voltage and output current can be seen in Equation 9 and Equation 10.

$$e = E \sin \omega t \quad (9)$$

*Equation 9. Expression for a sinusoidal voltage, where  $e$  = observed voltage at time  $t$ ,  $E$  = input voltage and  $\omega$  = frequency (in Hz) times  $2\pi$*

$$i = I \sin(\omega t + \varphi) \quad (10)$$

*Equation 10. Expression for the phase shift between input voltage and output current, where  $i$  = current,  $I$  = the maximum amplitude of the current and  $\varphi$  = phase angle between input and output*

Most materials have some degree of resistance and some degree of capacitance. They can be modelled as a series with the resistance and capacitance in series. The presence of a capacitance effect leads to the phase shift of the output current. If the material acts as a pure capacitor, the capacitive resistance can be shown as in Equation 11. Equally, if the material acts as a pure resistor, the current can be calculated through Equation 12.

$$i = \frac{E}{X_c} \sin\left(\omega t + \frac{\pi}{2}\right) \quad (11)$$

Equation 11. Expression for the capacitive resistance  $X_c$  for a pure capacitor, where  $X_c = 1/\omega C$

$$i = \frac{E}{R} \sin(\omega t) \quad (12)$$

Equation 12. Expression for the current of a pure resistor, where  $R = \text{resistance}$

$$\vec{E} = -jX_c \vec{I} \quad (13)$$

Equation 13. Expression for the voltage-current relationship for a pure capacitor, where  $\vec{E} = \text{voltage amplitude}$ ,  $j = \sqrt{-1}$  and  $\vec{I} = \text{current amplitude}$

For a pure capacitor, the output current would be perpendicular to the input voltage. This means that if the current were to be plotted on one axis (horizontally) and the voltage plotted on the other (vertically) then both real components could be described by the complex notation shown in Equation 13.

$$\vec{E} = \vec{E}_R + \vec{E}_C \quad (14)$$

Equation 14. Capacitance and resistance components in series

$$\vec{E} = \vec{I}(R - jX_c) = \vec{I}Z \quad (15)$$

Equation 15. Expression defining impedance  $Z$

As  $V = IR$ ,  $X_c$  must contain a resistive element. The voltage  $\vec{E}$ , when applied across a capacitor and resistor in series, must equal the sum of the voltage drops of each

individual element, as seen in Equation 14. Through combining Equation 13 and Equation 14, it is possible to define the impedance vector,  $Z$ , as can be seen in Equation 15. The impedance is formed of two parts; the real and imaginary parts, as seen in Equation 16.

$$Z = Z_{Re} - jZ_{Im} \quad (16)$$

Equation 16. Expression showing the two components of the impedance, where  $Z_{Re}$  = real part ( $R$ ) and  $Z_{Im}$  = imaginary part ( $X_c$ )

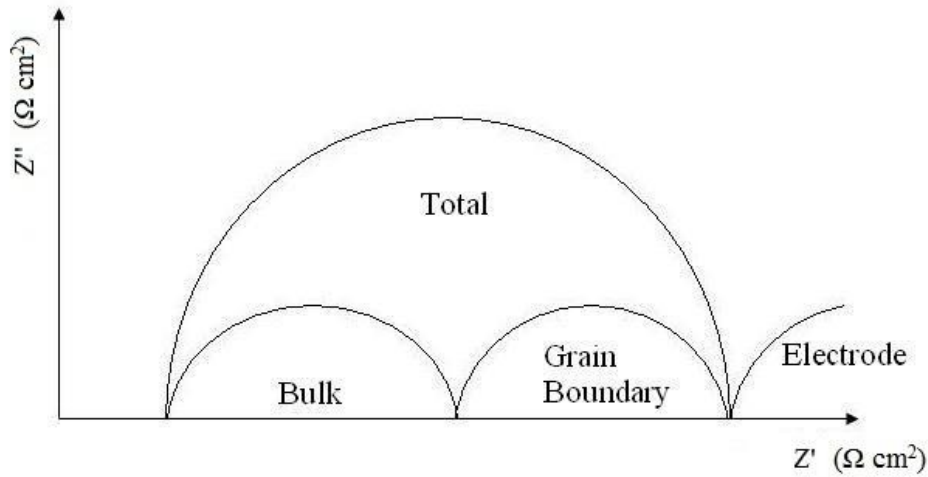


Figure 9. Example of a Nyquist-plot for ionic conducting solids, demonstrating different physical phenomena.  $Z''$  = imaginary impedance,  $Z'$  = real impedance

This data obtained through EIS is often expressed in a Nyquist plot, where the imaginary part of the impedance ( $Z''$ ) is plotted against the real part of the impedance ( $Z'$ ) as a function of frequency ( $\omega$ ). An example Nyquist plot can be seen in Figure 9.

Different physical phenomenon cause capacitance values of varying amounts, which can often be easily identified on a Nyquist plot. For example, ionic resistance in the bulk of the material would have a capacitance value in the region of  $10^{-12}$  F, whereas that of the grain boundaries within the material would have a capacitance value of  $10^{-11}$  -  $10^{-8}$  F. The bulk and grain boundary resistances can manifest themselves as separate curves on the Nyquist plot, however it is not uncommon for the curves to be partially or fully merged, especially when the resistance of one is significantly greater than that of the other. If impedance spectra are collected over a range of temperatures, it is possible to calculate the activation energy as per Equation 17.

$$\sigma T = Ae^{\frac{-E_a}{RT}} \quad (17)$$

*Equation 17. Expression for the calculation of activation energy as a function of the properties of the sample and the temperature, where  $\sigma$  = conductivity,  $T$  = temperature,  $A$  = sample surface area,  $E_a$  = activation energy and  $R$  = resistance*

The activation energy can easily be found by plotting  $\text{Log}_{10}(\sigma T) / \text{S cm}^{-1} \text{K}$  vs  $T^{-1} / \text{K}^{-1}$ , with the activation energy being the slope of the resultant line.

The system analysed can be modelled as an electrical circuit, with the behaviours of different components represented through capacitors and resistors. There are several physical behaviours for various different cell components that have equivalent circuit elements, which are listed below.

- Polarisation resistance: also known as overpotentials, these occur whenever the potential of an electrode is forced away from its OCV value. These can be split into three separate components; activation polarisations, caused by the reaction kinetics within the electrodes; ohmic polarisations, caused by the resistance to the transfer of ions through the electrolyte (and, to a smaller degree, the electrodes); and concentration polarisations, caused by limitations on the availability of reactants and the ability of the system to replenish consumed reactants.
- Double layer capacitance: The capacitance effect of forming a layer of ions on the surface of a catalytically active substance, allowing the storage of a small amount of electrical energy. This may also be modelled by a constant phase element, which helps to define a capacitor which is not behaving in an ideal manner (common in a real cell).
- Charge transfer resistance: the resistance of the transfer of charge from the reactants to the system, and vice versa.
- Warburg impedance: caused by the diffusion of reactants. This is low at high frequencies and increases linearly with reduction in frequency due to the additional distance that reactants have to travel.

Typically, cell components are modelled as having several equivalent circuit elements acting simultaneously, allowing accurate representation of the properties of the component. The various elements can be modelled either in series or in parallel in order to build as correct a portrayal of the system involved.

### 3.9.2.2. Area Specific Resistance (ASR)

The area specific resistance measurements made in this work use a variation on AC impedance spectroscopy in order to acquire data. The ASR of electrode materials contributes to the ohmic resistances of the overall cell, and as such it is important to quantify and minimise these resistances where possible. Determining ASRs involves passing an alternating current of different frequencies across a sample and measuring the impedance. The components of a typical impedance are displayed in Equation 18.

$$Z = Z'(\omega) + jZ''(\omega) \quad (18)$$

*Equation 18. Typical impedance (Z) where Z' is the real part, j is the imaginary unit,  $\omega$  is the frequency and Z'' is the imaginary part*

Data collected using ASR are also commonly expressed using a Nyquist plot, containing similar features as those formed through A.C. impedance conductivity. While ASR can provide complex data when carried out on a full fuel cell, the complexity is minimised when performed on a simplified cell. Cells used within this thesis comprise of a dense sintered pellet of either CGO or YSZ electrolyte onto which a symmetrical layer of electrode ink was applied to both sides and then heated to bond to the electrolyte. A layer of platinum paste was then applied to both sides with a strip of platinum foil to allow connection to an external circuit. This allows the cell to be analysed through AC impedance spectroscopy. The dense electrolyte pellet, which has an electrical resistance several orders of magnitude larger than that of electrode materials, appears on the

Nyquist plot separately so identification of the electrode and electrolyte response is straightforward to carry out.

The area specific resistance can be calculated using data from the Nyquist plot. The resistance forms a semicircle which crosses the x axis at least once. If a circle is fitted for this data, the difference between the intercept points for the electrode response can be used to calculate the ASR as in Equation 19. It should be noted that ASR analysis can be carried out without fitting, simply through use of the intercept points on the x axis.

$$ASR = \frac{I_H - I_L}{n} \times A \quad (19)$$

*Equation 19. Calculation to determine the ASR from the intercept points on a Nyquist plot, where  $I_H$  = high intercept,  $I_L$  = low intercept,  $n$  = number of sides (in the case of a pellet, always 2) and  $A$  = area of one face*

Within this thesis, ink suspensions were prepared containing 1:1 wt% of electrolyte and electrode materials with 20%wt Decoflux (Zschimmer and Schwarz) to act as a dispersant and binder. These inks were then ball milled (Fritsch Pulverisette 7 Planetary Mill for 1 hour at 350 rpm) and coated onto dense pellets of  $Ce_{0.9}Gd_{0.1}O_{1.95}$  (CGO10, Aldrich, presintered at 1500 °C for 12 hours) to form a symmetrical cell and then fired at 1000 °C for 1 hour. Pt paste was then applied to both sides to act as a current collector and heated at 800 °C for 1 hour. ASR values were obtained in both cathodic (air) and anodic (5% $H_2/N_2$ ) conditions at temperatures up to 800 °C (air) / 600 °C (5% $H_2/N_2$ ). Impedance data were collected between 5 Hz - 13 MHz with an AC signal amplitude of

100 mV (HP 4912A Frequency Analyser), setting which had previously shown to give reliable and repeatable results with few anomalies [126]. The spectra were plotted using ZView software [127] to give an estimate of the resistance and capacitance of the different cell component materials.

### **3.9.3. Fuel Cell Testing**

Fuel cell testing was carried out on both microtubular cells and simple button cells. The test rig was custom built using insulating fire blocks (Thermal Ceramics) and ceramic rods. Nichrome ribbon (Advent Ni80/Cr20 1.5 mm x 0.13 mm) was used for heating elements, wound around the ceramic rods. The blocks were hollowed to allow a heating chamber to be formed. A Eurotherm 2404 controller was used to control the formed furnace. Unit Instruments 7300 mass flow controllers (MFCs) regulated gas flow to the system, via Swagelock piping. The tubes undergoing testing were inserted onto an inlet pipe with an external diameter of approx 1.5 mm which allowed fuel to be supplied to the anode layer on the inside wall of the mSOFC. Gases were supplied by BOC, with 99.95% pure H<sub>2</sub> and 50:50 He/H<sub>2</sub> being used. A schematic of the equipment used can be seen in Figure 10.

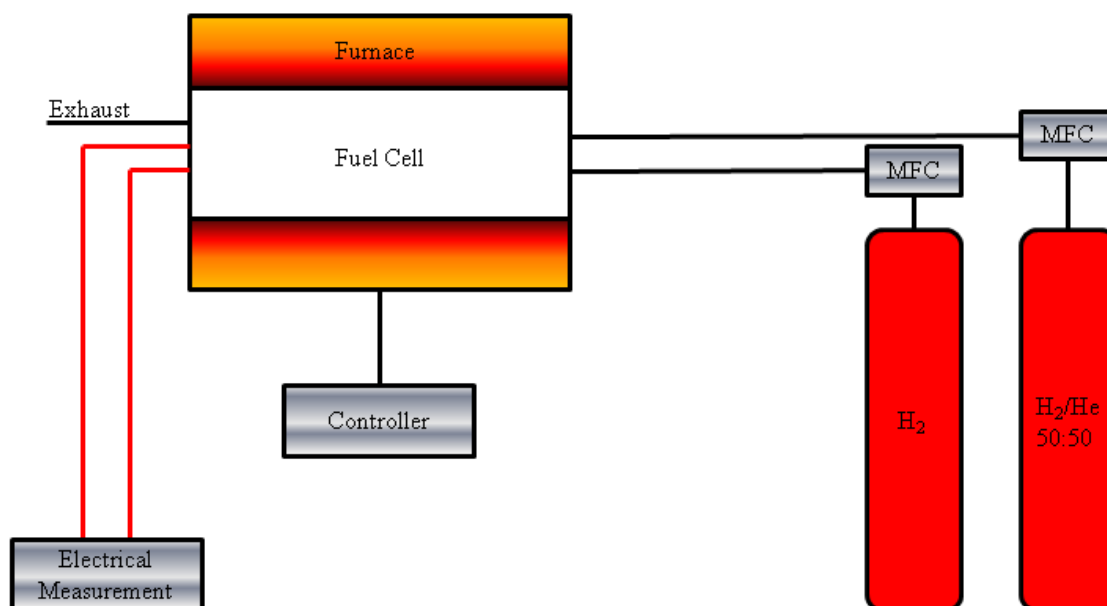


*Figure 10. Schematic diagram of the fuel cell test equipment used in this thesis*

The button cells required additional equipment in order to make them gas tight. Cells prepared were coated with porous silver ink paste (SPI) over the surface of both electrolyte layers, and used to attach a short length of silver wire (Silver Wire Co, 99.98%) to either side. The button cell was then cemented onto a ceramic firing tube with an outer diameter matching the size of cell, using ceramabond (Aremco) and left to set for 6 hours. Once set, the same test procedure for the m-SOFCs was followed; the firing tube with the button cell was placed over a length of Swagelock<sup>®</sup> tubing within the furnace, allowing hydrogen to be supplied to the anode side sealed within the firing tube and allowing air to reach the cathode side still exposed. A schematic showing the test setup in more detail can be seen in Figure 11.

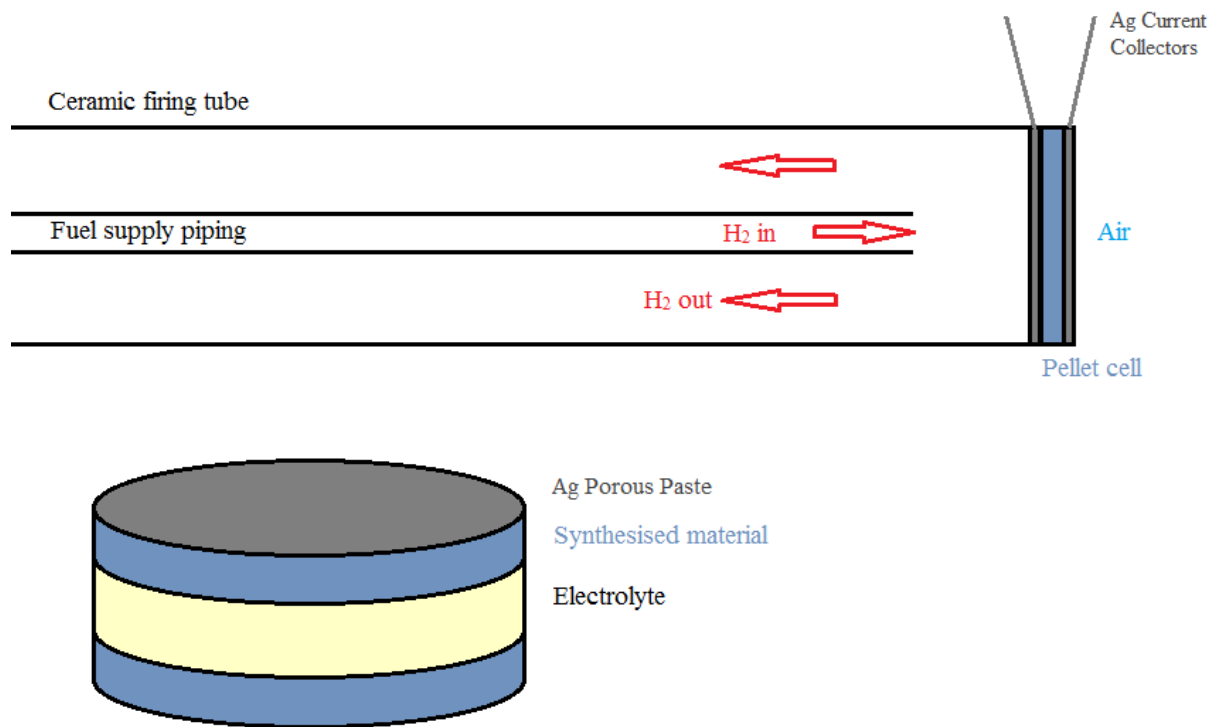


Figure 11. Schematic diagram of the pellet cell test setup used in this thesis

A Solartron 1400 was used to record all electrical measurements and to control electrical demands on the cell. The Solartron CellTest suite of software was used to program a test profile and to analyse results obtained.

### 3.9.3.1 Fuel Cell Thermodynamics

As a fuel cell is an energy conversion device, the efficiency of conversion is of paramount importance. This can be calculated theoretically and also verified experimentally. The energy available for conversion to electrical work is given by the Gibbs free energy change for the overall cell reaction, which is the difference in the energy of formation of the products and reactants and is the maximum amount of energy

that can be produced from the reaction under the conditions specified. The Gibbs free energy change at STP for the reaction between hydrogen and oxygen to give liquid water can be seen in Equation 20.

$$\Delta G = G_{f, products}^{\Phi} - G_{f, reactants}^{\Phi} \quad (20)$$

$$\Delta G = G_{f, H_2O}^{\Phi} - (G_{f, H_2}^{\Phi} + G_{f, O_2}^{\Phi}) = -237.2 - (0 + 0) = -237.2 \text{ kJmol}^{-1}$$

*Equation 20. Gibbs free energy change of the reaction of hydrogen and oxygen to form water*

The Gibbs free energy change is itself a function of temperature and reactant concentration (equated to partial pressure for gaseous reactants) and can be seen in Equation 21, where  $\Delta G^{\Phi}$  is the standard Gibbs free energy change, R and T are the universal gas constant ( $8.134 \text{ J K}^{-1} \text{ mol}^{-1}$ ) and absolute temperature, and  $p_{H_2O}/p_{H_2}/p_{O_2}$  are the partial pressures of  $H_2O$ ,  $H_2$  and  $O_2$  respectively.

$$\Delta G = \Delta G^{\Phi} + RT \ln \left( \frac{p_{H_2O}}{p_{H_2} p_{O_2}^{1/2}} \right) \quad (21)$$

*Equation 21. Gibbs free energy change for the reaction of hydrogen and oxygen to form water, with respect to partial pressure of gases*

If the system is assumed to be operated reversibly, with all Gibbs free energy being converted to electrical energy, then the electromotive force between the anode and

cathode takes the value of  $E$  in Equation 22, with  $n$  being the number of electrons involved in the reaction and  $F$  being Faraday's constant ( $96485 \text{ C mol}^{-1}$ ).

$$\Delta G = -nFE \quad (22)$$

*Equation 22. Calculation of electromotive force between anode and cathode in a fully reversible system*

Combining Equation 21 and Equation 22 leads to Equation 23, the Nernst equation, in which  $E^\Phi$  represents the reversible potential under standard conditions (1.23 V for a hydrogen/oxygen system).

$$E = E^\Phi + \frac{RT}{nF} \ln \left( \frac{p_{H_2} p_{O_2}^{1/2}}{p_{H_2O}} \right) \quad (23)$$

*Equation 23. Nernst equation for the reaction of hydrogen and oxygen to form water*

The Nernst equation relates the open circuit voltage (OCV, represented by  $E$ ) of the fuel cell to the temperatures and (in this case) partial pressures of reactants and products. Typically for an SOFC running on hydrogen at  $800 \text{ }^\circ\text{C}$  the open circuit potential is between 0.9 - 1 V.

### **3.9.3.2 Fuel Cell Polarisation Curve**

A fuel cell undergoing evaluation is usually subject to testing to determine the current-voltage response of the cell. By recording the response of the cell to different loads

placed upon it, it is possible to form a fuel cell polarisation curve, an example of which can be seen in Figure 12.

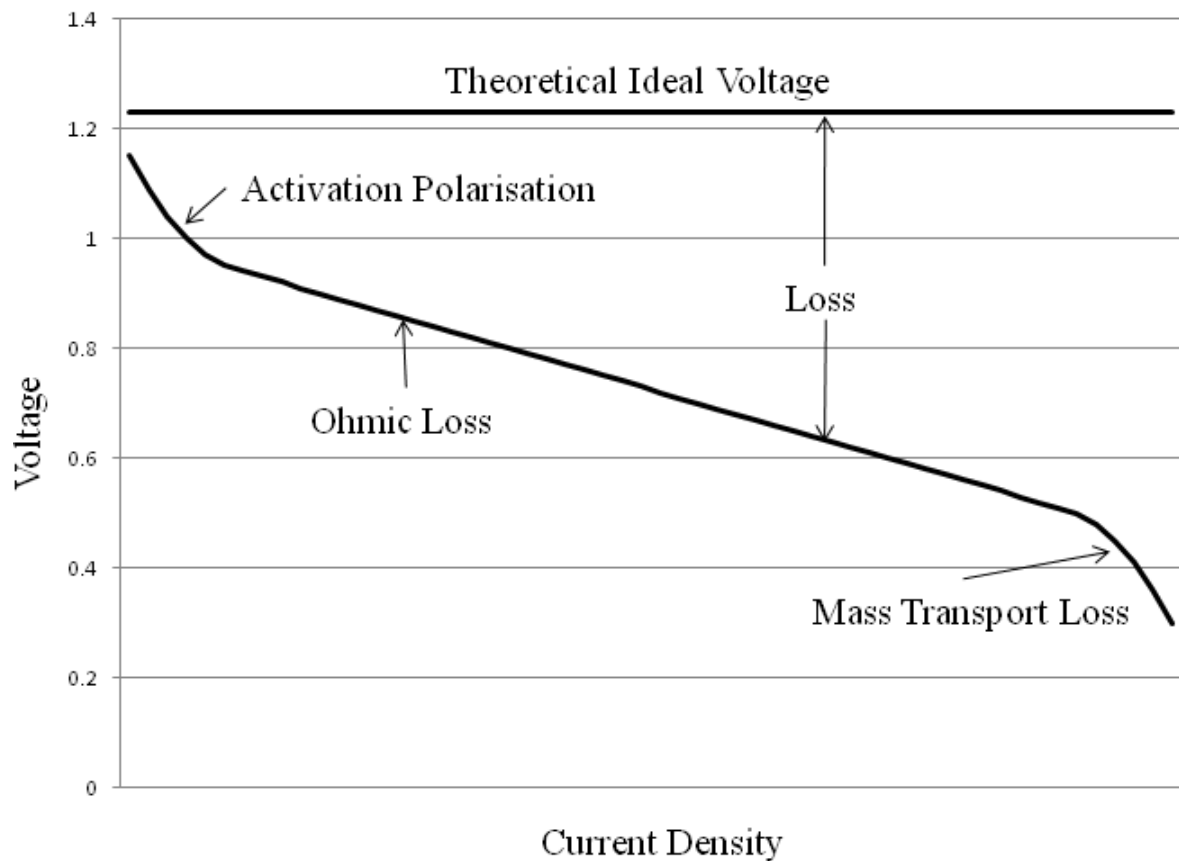


Figure 12. Example fuel cell polarisation curve showing the three main sources of voltage losses

The voltage losses within a fuel cell polarisation curve can be split into 3 main categories: activation polarisation losses, ohmic losses and mass transport losses.

- Activation polarisation losses are primarily caused by the kinetics of the reactions taking place at the electrodes; for example, the oxidation of hydrogen to protons.
- Ohmic losses are primarily caused by resistances in the materials used within the cell; for example, the electronic resistance of the electrode materials.

- Mass transport losses are primarily caused by the inability for enough reactants to be supplied to the active layers of the electrodes to supply demand.

Developments in SOFC anode materials may assist in reducing losses caused in any of these three sections. For example, improvements in electronic or oxide ion conductivity would potentially reduce ohmic losses, while improvements in catalytic activity may bring about a lowering of activation polarisation losses.

### **3.10. Microtube Manufacture**

The processes used in the manufacturing of SOFC microtubes are detailed within this section. A SOFC microtube (m-SOFC) is a solid oxide fuel cell with a tubular geometry, typically in the region of 1 - 20 mm diameter. The tubular nature affords many advantages, such as far easier gas sealing with respect to planar SOFCs, and small tube diameters which allow relatively fast heating and cooling times. The m-SOFCs comprises of several layers, with electrode materials on the inner and outer surfaces of the cell and the electrolyte layer separating the two. Figure 13 displays an example of the particular variety of anode-supported m-SOFC investigated within this thesis.

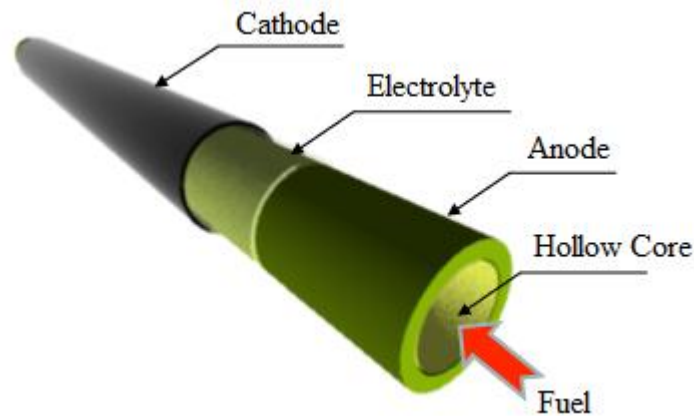


*Figure 13. Schematic of an anode-supported m-SOFC [111]*

### **3.10.1. Powder Preparation**

Constituent powders were first milled using a vibromill to break down any particle agglomerates and to ensure all solid materials had been mixed; this process is common in cermet production [128]. This functions by rapidly shaking the sample within an enclosed vessel containing milling beads, and can be used to break up particle agglomerates, mix powders and reduce average particle size. It has also been noted that ball milling of SOFC cermet powders can lead to increases in sample conductivities and performance post sintering [129, 130]. This is believed to be due to the even distribution of YSZ over the surface of the Ni particles and the interconnection between nickel particles being increased, leading to a greater triple phase boundary area and subsequent performance.

Powders were measured out in their respective quantities for the particular paste being formed, and were then placed within a milling bottle. Ceramic milling beads were added

and the bottle sealed before being placed within the vibromill. The powders were milled for 24 hours to ensure they were fully mixed and all agglomerates were broken down.

### **3.10.2. Paste Formation**

The formation of a paste, which can be extruded to form a tube, is instrumental in the overall process and the materials used can affect the performance characteristics of the cell. The materials required for the anode are measured out in powder form and combined with a binder which serves to hold the powders together. The binder is often formed of both solid and liquid components, which when combined form an initial amorphous solid [131]. The solvents used serve to soften the solid plastics to make them more malleable and allow it to form a paste.

After being vibromilled, the liquid dispersants and binding agents were added to the powders to begin paste formation. These were stirred by hand within a fume hood until the powders began to form large agglomerates. The paste itself was formed using a twin roll mill. This is a set of two smooth cooled metal cylinders, with a small adjustable gap in between them, rotating in opposite directions at slightly different speeds. Photos of the twin roll mill can be seen in Figure 14.

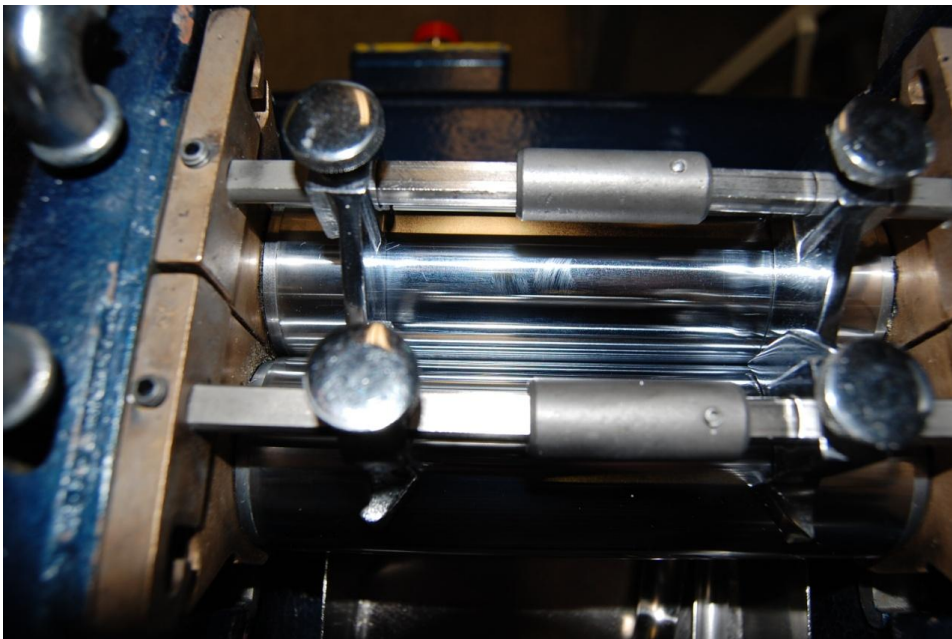
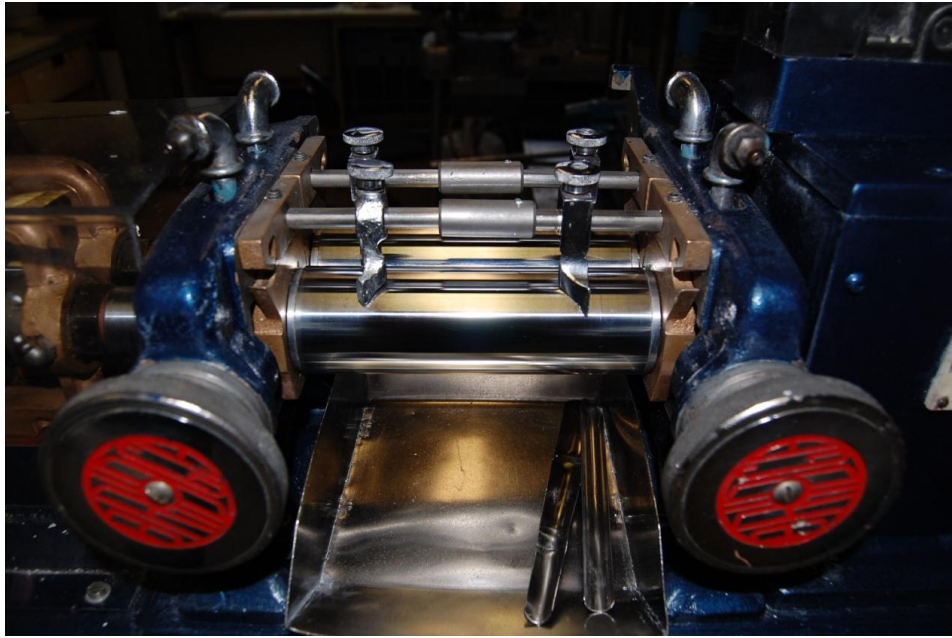


*Figure 14. The Bridge twin roll mill used for this work*

The mixture was added slowly to the two cylinders to form the paste while the distance between them is gradually increased in line with the increased sample quantity. The distance between the rollers was closely monitored and adjusted to cause shearing of the paste to further aid mixing. The paste formed was tactile enough to adhere to the rollers,

typically more to the slower rotating cylinder than the faster. The rotation movement forces it through the gap in between the cylinders which causes further mixing through shearing. The desirable properties of the paste for this extrusion manufacturing technique include it being soft and flexible enough to allow it to fold without cracking, and it should also be possible to remove it from the cylinder without it sticking. It typically took 10 - 15 minutes to achieve the correct consistency, during which time the materials become well mixed. The paste was cut from the roller and re-applied to the cylinders several times, in order to maximise mixing on the mill, before it was ready to use.

The twin roll mill utilised is of a suitable size to deal with batches of material as small as 50 g total of ceramic and metal powder, in addition to the binding formulation used. Any smaller quantities would lead to the sample being too thin on the mill to work with easily and would not provide enough material to allow extrusion to be carried out, while larger batches can still be accommodated.

### **3.10.3. Cold Extrusion**

Extrusion involves the compression of a material, which is then forced through an aperture to cause it to form a specific shape. Extrusion is used to manufacture a wide range of products, from steel girders to pasta [131]. There are many variations of extrusion, however this thesis will focus on single barrel ram extrusion. This particular type of extrusion involves a barrel into which the material to be extruded is placed. A die set is installed at one end, with a ram inserted at the other. Pressure is applied via a computer controlled load cell to the ram in order to force the material out of the die set,

see Figure 15.

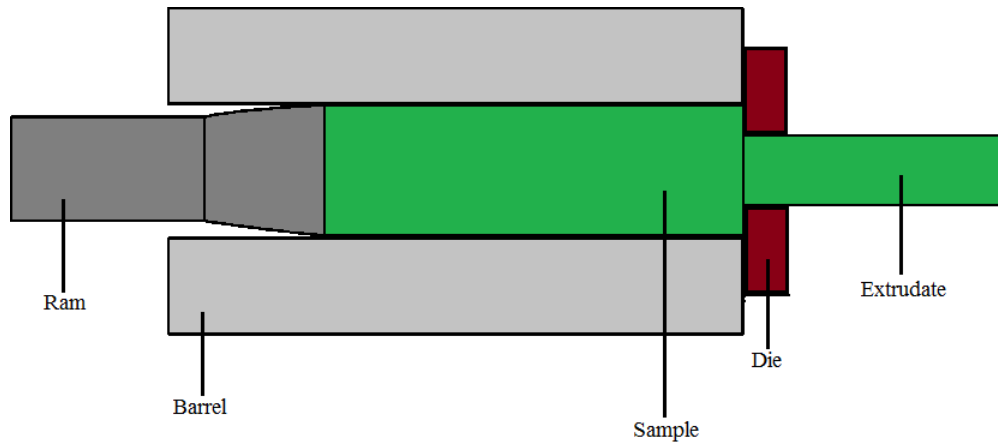


*Figure 15. Diagram detailing a basic extrusion technique*

The extrusion die and equipment used here comprises of a barrel of 21 mm diameter onto which a die is attached. This die is a metal cylinder with a central hole of 2.2 mm diameter and a small indentation for an alignment cylinder. The extruder ram has been manufactured with a thin cylinder of metal of 1.8 mm diameter (from here on referred to as the mandrel) in the centre of the rod, which is designed to fit through the hole in the die, causing the material present to be extruded as a tube with walls of 0.2 mm thickness. The indentation in the die is to allow for a small brass cylinder, with the same diameter hole as that of the mandrel, to fit onto the end, outside of the extrusion barrel, which aligns the mandrel central to the die. This is forced out of the way once extrusion begins and is designed to ensure that the walls of the tubes produced are as uniform as possible.

Co-extrusion was initially considered for this project, however was later ruled out. This was due to several reasons: the required extensive work on paste rheology for pastes

comprising of novel materials would reduce the ability to quickly prepare tubes of a variety of materials; the complexity of die sets increases the difficulty of re-engineering if required; and that control of the thickness of the layers of material has proven difficult, leading to difficulties in comparison between different materials produced through the same technique. Overall, if the intention would be to produce tubes on a larger scale than a prototype basis, co-extrusion would be well suited as it could considerably cut down the production time of a batch of tubes, if properly controlled.

Photographs of the extrusion ram, mandrel and Instron extrusion equipment can be seen in Figure 16, Figure 17 and Figure 18.

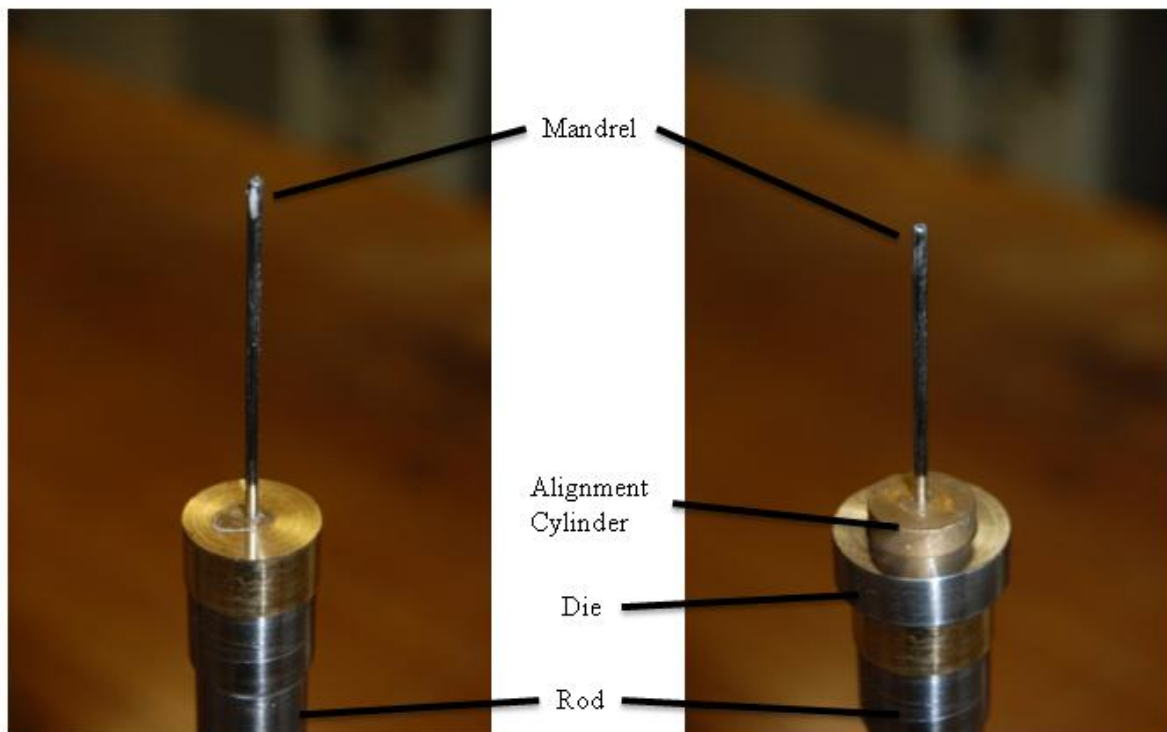


*Figure 16. Extrusion rod complete with mandrel, without and with extrusion die and alignment cylinder*

The paste is prepared for extrusion by cutting to size and wrapping it tightly around the mandrel to the width of the extrusion ram before inserting the extrusion ram into the barrel. The correct size is to allow 5 mm at the end of the mandrel to be exposed which can then be used to align the equipment, utilising the brass collar to confirm central alignment. The die and barrel setup is then installed into a set of extrusion equipment, in this case an Instron 4467 with a 30 kN load cell.

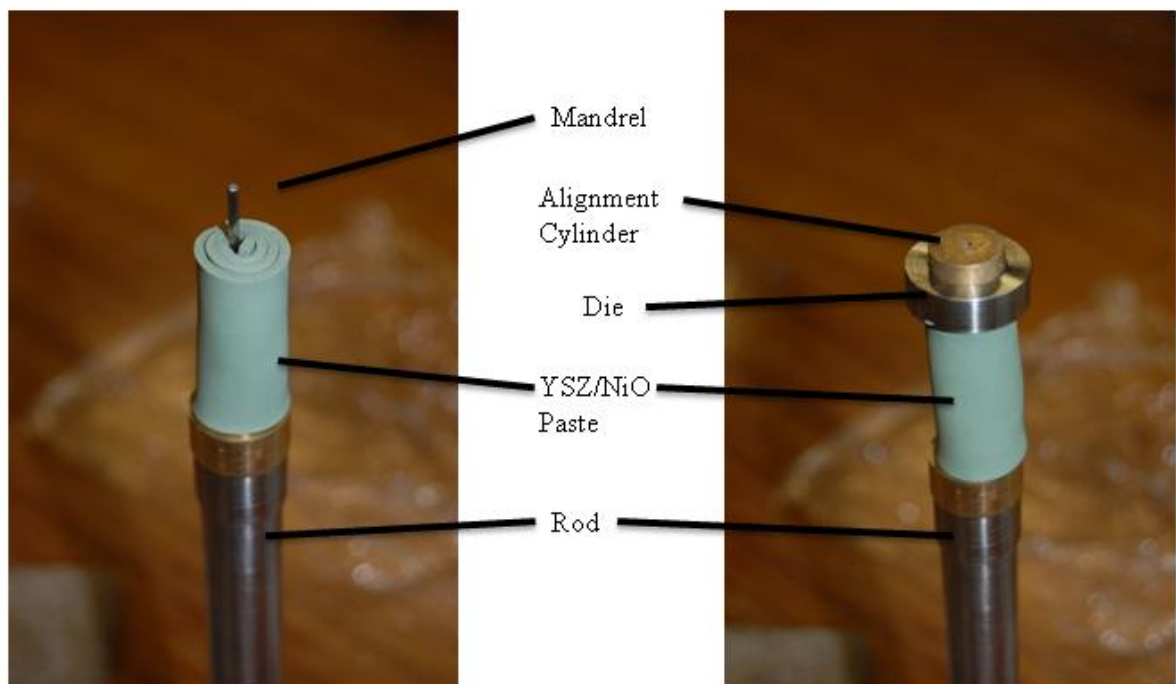


*Figure 17. Extrusion ram and mandrel with YSZ/NiO paste wrapped around it. (L) shows before insertion into extrusion barrel, (R) is setup complete with die as it would be inside the barrel*

A simple program is run to extrude the paste into a tube. The equipment is set to compress at a rate between 0.5 mm and 2 mm per minute, which leads to the tube being extruded at approximately 1 mm per second. On starting the extrusion process, the small

alignment piece is forced off the end of the mandrel by the extruded tube, which then continues to be forced out of the die. These tubes are cut into lengths and laid on drying racks to allow the solvents to evaporate, causing the binders to harden and give the tubes temporary mechanical strength, before debinding and sintering of the ceramic takes place.

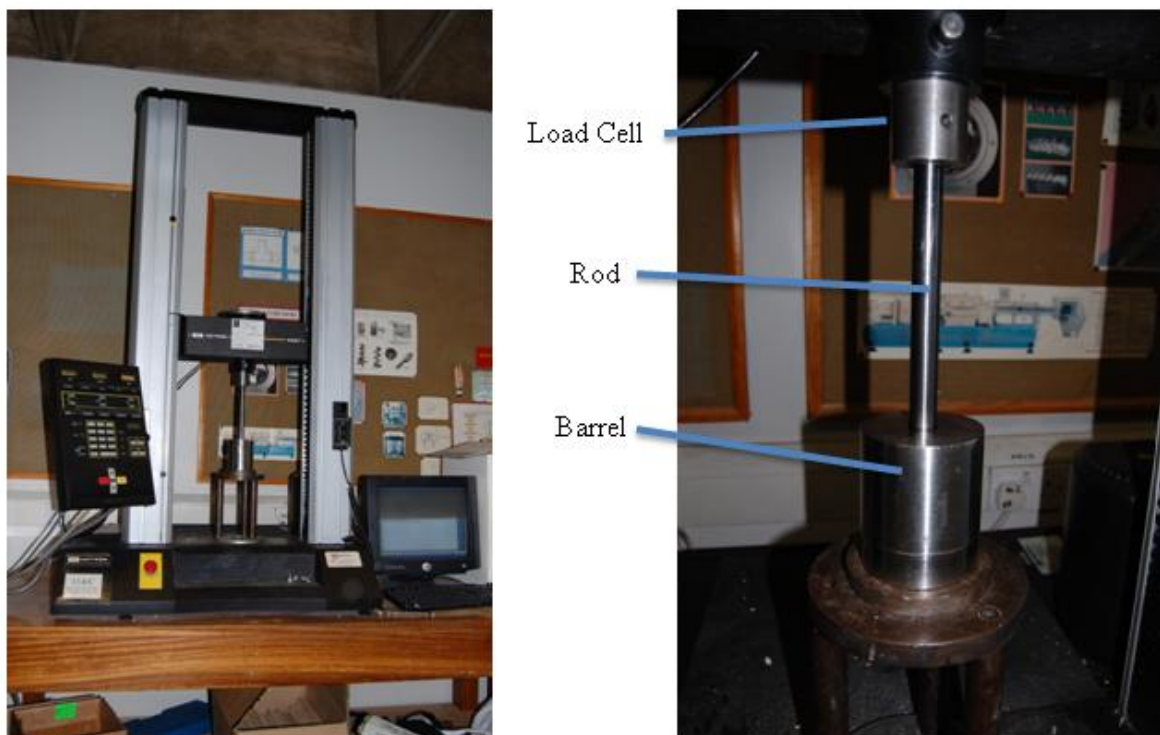


*Figure 18. Instron 4467 with 30kN load cell and sample installed (L), close-up of sample ready to extrude (R)*

Much of the powder processing, paste formation and extrusion work within this thesis was based on methodology by Taylor et al. at the University of Birmingham [15].

#### **3.10.4. Hot Extrusion**

Hot extrusion was considered for use in this project. The process can be performed in a variety of ways, all involving the use of a binder which is solid at room temperature and liquid when heated. The heated medium is extruded through a die, as above, to form the extrudate into the desired shape.

Work was carried out into use of a linear single screw hot extrusion machine for extruding YSZ/NiO anode-supported microtubes. This equipment comprises of a hopper containing the desired materials and binder at one end, a single archimedes screw which forces the material through the system, a heating barrel which surrounds the screw to provide a heat input, and a die set to form the extrudate to the shape required. Once formed and cooled, these tubes can be sintered in the same fashion as those formed through cold extrusion. Within this thesis, a Rondol Linear 18 single screw hot extruder was used.

#### **3.10.5. Debinding and Sintering**

The debinding process removes the plastic and organic binding agents used to form the paste. As this leaves the tubes very fragile it is combined with the first stage of sintering the ceramic involved, which reduces handling and helps to minimise damage to the tubes. This interconnection of ceramic gives the tube its mechanical strength and provides the support for the other layers.

As debinding of organic materials usually occurs over 200 °C but sintering of most ceramics requires at least 1000 °C (and often far higher), the temperature profile for the overall process must be well structured in order to complete debinding and sintering without the thermal stress of heating and cooling damaging the cells, as well as also minimising the amount of time taken. The profiles used are detailed, along with various binding and anode mixtures, within the extrusion experimental section of this thesis.

### **3.10.6. Layering**

Each anode-supported microtube must be layered with both electrolyte and cathode materials once the anode has been sintered. This can be achieved using a variety of techniques, the most common of which are electrospray deposition, spray coating and dip coating. The electrolyte layer should be as thin as possible, while still being a complete and unbroken layer, in order to minimise resistance while preventing short circuiting. The cathode layer should have high porosity in order to afford a large surface area, while remaining complete and unbroken, so as to allow the easy collection of current produced.

#### **3.10.6.1. Electrospray Deposition**

Electrospray deposition involves using an electric charge to produce an aerosol from a liquid sample. The sample contains, either in solution or suspension, the materials which will form the layer required. The liquid is electrically charged and then passed through a jet nozzle which causes it to form many small droplets, kept apart by coulomb repulsion.

The size of these droplets can be tuned by changing the charge and the nozzle, amongst other factors. This aerosol is deposited on a ground surface, losing its charge in the process, and forming a layer. The technique is highly adjustable and can produce layers of nearly any thickness, making it very well suited for electrolyte deposition. Electro spray deposition of thin layers for use within SOFCs has been studied at length, for example the deposition of YSZ for use in IT-SOFCs [132]. It is also possible to apply layers of different materials over one another, potentially speeding up the fabrication process.

However, the equipment is costly and time consuming to calibrate and prepare, which could only be justified in this case if tubes were to be produced on a large scale. As work was to be focused on small batches of tubes, this technique is less appropriate. If tube production were to be scaled up or made commercial, electro spray deposition would be amongst the recommended layering techniques, as the preparation time and cost could be accounted for.

#### **3.10.6.2. Spray Coating**

Spray coating is similar to electro spray deposition in that it is the production of an aerosol (containing materials of interest), which is deposited on a surface. However, it usually uses compressed gas to both produce and propel the aerosol, rather than a current, and this aerosol is directed at a target. It has the advantage of being relatively quick to set up and the equipment required is cheap. However, it is much more difficult to accurately determine and alter the thickness of the layer produced, making it less

suited to larger scale production. This inability to control the layer thickness to any degree of accuracy also renders the process less repeatable. In addition, spray coating can lead to a large wastage of material which would significantly lower the efficiency of the process and the waste material would need to be recovered. Spray coating has been successfully deployed to deposit SOFC materials such as LSCF, BSCF and LSM cathodes, SDC protective layers and YSZ electrolyte layers [28, 133–135].

### **3.10.6.3. Dip Coating**

Dip coating involves immersing a surface in a sample liquid containing either a solution or suspension of the desired layer material. When removed from the suspension, the liquid dries leaving a layer of solid behind. The process can be repeated in order to build up thicker layers, if required, and can also be used to deposit layers of different materials. The technique is made far more repeatable by utilising an automated machine to control the speed of motion and duration of immersion, and has been carried out successfully to form layers of common SOFC materials, such as electrolyte layers comprising of YSZ [112]. The thickness of layers produced can be varied through changing the formulation of slurry used. This technique falls somewhere between electrospray deposition and spray coating with regard to ease and preparation time, as it requires more expensive equipment and more time to set up than the latter, but less time and less expensive equipment than the former.

#### **3.10.6.4. Vapour Deposition**

Vapour deposition allows a thin film layer of material to be deposited onto a target surface. There are two main types of deposition; physical vapour deposition (PVD) and chemical vapour deposition (CVD).

#### **3.10.6.5. Physical Vapour Deposition**

PVD is carried out by bombarding a source material with energy in order to vaporise it, before this vapour is deposited onto a target surface. There are several different methods which can be employed to vaporise the source, such as sputtering, electron beam, cathodic arc and evaporative, all of which require specialist equipment and have various advantages and disadvantages. They generally allow a specific layer thickness to be built up and the microstructure of the layer produced can also be altered in some cases, such as 1  $\mu\text{m}$  layers of CGO barrier layers within SOFCs [136]. However it can take a long time to set up in order to be able to reproduce and control the layers, and the equipment can also be expensive which renders it unsuitable for this study. In addition, not all materials are suitable for PVD application due to the high energies involved to induce vaporisation, which can lead to disintegration or alteration of the source.

#### **3.10.6.6. Chemical Vapour Deposition**

CVD is widely used in the electronics industry as a large-scale method of applying a controllable thin film of material onto surfaces. It involves the deposition of a layer

through a chemical process and so involves precursor materials which undergo reactions to form the desired product material. The conditions for the process can be widely varied, allowing liquid, gas and plasma based processes combined with variable vacuum conditions to produce layers of precise thicknesses and microstructures. However, like PVD, the expense and time taken to calibrate the equipment is a significant drawback with relation to this project, and so CVD was not considered. CVD has been used to deposit YSZ-containing cermet layers, amongst other materials [137].

Both spray coating and dip coating were used to prepare tubes documented within this thesis, as equipment was available and could be tailored to the requirements of the project in a fairly short amount of time. In addition, the smaller quantities of tubes produced make both techniques highly suitable, with spray coating being favoured overall due to the thin layers produced.

### **3.11. Scanning Electron Microscope (SEM)**

SEM is a technique involving the use of a scanned beam of electrons to image a surface. Due to the narrow nature of the electron beams used, SEM can produce high resolution images of features down to approx. 1 nm in size, with a magnification of up to 500 000 times [138]. This is several orders of magnitude better than the most advanced light microscopes, due to their use of electromagnetic waves of much longer wavelength than the electrons used in SEM. In addition, back scattered electrons (BSEs) reflected from the sample are used to differentiate areas of the sample containing elements of different

atomic number. This is made possible due to the heavier atoms interacting more with an electron beam than lighter ones, so a larger proportion of electrons are reflected.

If it is desirable to determine the exact elemental composition of an area of a sample examined, many SEMs have the ability to analyse samples using energy-dispersive X-ray spectroscopy (EDX, also known as EDS or XEDS). When the electron beam interacts with the sample it excites some of the electrons from the ground state in the sample into an outer shell vacancy, creating an inner shell vacancy. When an electron from a higher energy shell fills this inner shell vacancy it gives off a photon of energy in the X-ray wavelength. Due to differences between the shell energy levels in all elements, the X-rays given off are unique to each element and can be used to identify the species.

Utilising SEM and EDX in tandem can be particularly useful when studying the change between aged and new SOFC cells as it can show species migration and agglomeration of particles and can be used to identify the elements involved. In addition the effect of sintering can be observed by analysing cells before and after. However, like many X-ray based techniques it is difficult to analyse organic-containing components such as carbon deposits within SOFC cells due to the light size of the elements involved, as X-rays interact weakly with lighter elements.

A standard SEM setup usually involves an electron gun which is principally a cathode made of tungsten. This is heated and charged using an electrical current which causes the emission of electrons. Tungsten is often used due to its low cost and high melting temperature, which allows it to remain a reliable electron source for a long working life.

The beam can be altered in energy by changing the temperature and the current passed through the cathode, typically between 0.5 and 40 keV. This beam is focussed by lenses to a typical diameter of between 0.5 and 5 nm. This flexibility on energy and beam size allows different materials and structures to be imaged in high clarity. The interaction of the beam with the interaction volume of the sample is measured through the detection of the elastic and inelastic scattered electrons, and analysis of their energy and position along with the detection and analysis of any electromagnetic radiation emitted. As the technique scans over the surface it allows a picture to be built up, which is normally stored as a digital image.

Most SEM analysis is conducted in a vacuum, due to electron beams being dispersed by gases, which would lead to interference. In addition, samples must be electronically conductive and ground at the surface in order to record an image of a sample. This prevents any build-up of electric charge while the sample is being analysed. While this makes metal items very straightforward to prepare for SEM imaging, non-conductive specimens must be mounted on a metal sample stub before being coated with a conductive material, typically gold. This is either performed using sputter coating or evaporation; with the former being most common due to the low vacuum requirements (evaporation needs a high vacuum). The layer formed allows all charge built up to be dispersed through the stub. For the purposes of this thesis, all specimens analysed were prepared on sample stubs, and coated with gold via sputter coating.

The equipment used within this thesis is a Philips XL-30 scanning electron microscope. The information gained through SEM imaging in this thesis was used to analyse the

dispersion and microstructure of particles and materials within formed SOFC microtubes, along with details such as the porosity of the material. In addition, the size of particles or layers could be measured accurately and this information could be used to identify potential ways to improve the production techniques of both materials used in making the SOFCs, and also the procedures used to manufacture the SOFCs. For example, specimens which display poor porosity in both anode and cathode layers could be improved in several ways; either the manufacturing composition could be changed to include more, or a different type of pore forming agent (PFA) in the mixture of materials, or the materials themselves could be synthesised with different size or shape of particles in order to attempt to improve the porosity.

## **Chapter 4. Extrusion and Fabrication of Microtubular**

### **SOFCs**

#### **4.1. Introduction**

Microtubular and planar SOFCs operate with similar principals; however, they have various advantages and disadvantages over each other. Planar SOFCs typically have higher power density and are simpler to manufacture; however, due to their size, they typically suffer from slower start-up times which are necessary to ensure even heating of cells. For these reasons, planar stacks of cells are more suited to continuous power supply systems with few on-off cycles.

Microtubular SOFCs, however, are better suited to applications where faster start-ups are required. Cells have been shown to be stable when heated at rates of up to  $100\text{ }^{\circ}\text{C min}^{-1}$  [139] and small stacks of cells have been shown to be relatively straightforward to design [140]. Due to the geometry, they are also much easier to seal than planar cells; however, there are usually more cells involved in a single stack so cell interconnections become more complex. Smaller diameter cell sizes, while bringing about more interconnections, also increase the power density of a stack, so some trade-off is required between power density and complexity.

There are a variety of manufacturing techniques which are suitable for the production of microtubular solid oxide fuel cells. Several stages are required for the production of cells from dry powders. These stages can be broken down into four individual groups: Tube Manufacture, Electrolyte Deposition, Cathode Deposition and Cell Test Preparation. Each stage has several sub-stages for separate processes. The procedure followed within this Chapter was based around work carried out by Taylor et al [15] and can be seen in Figure 19.

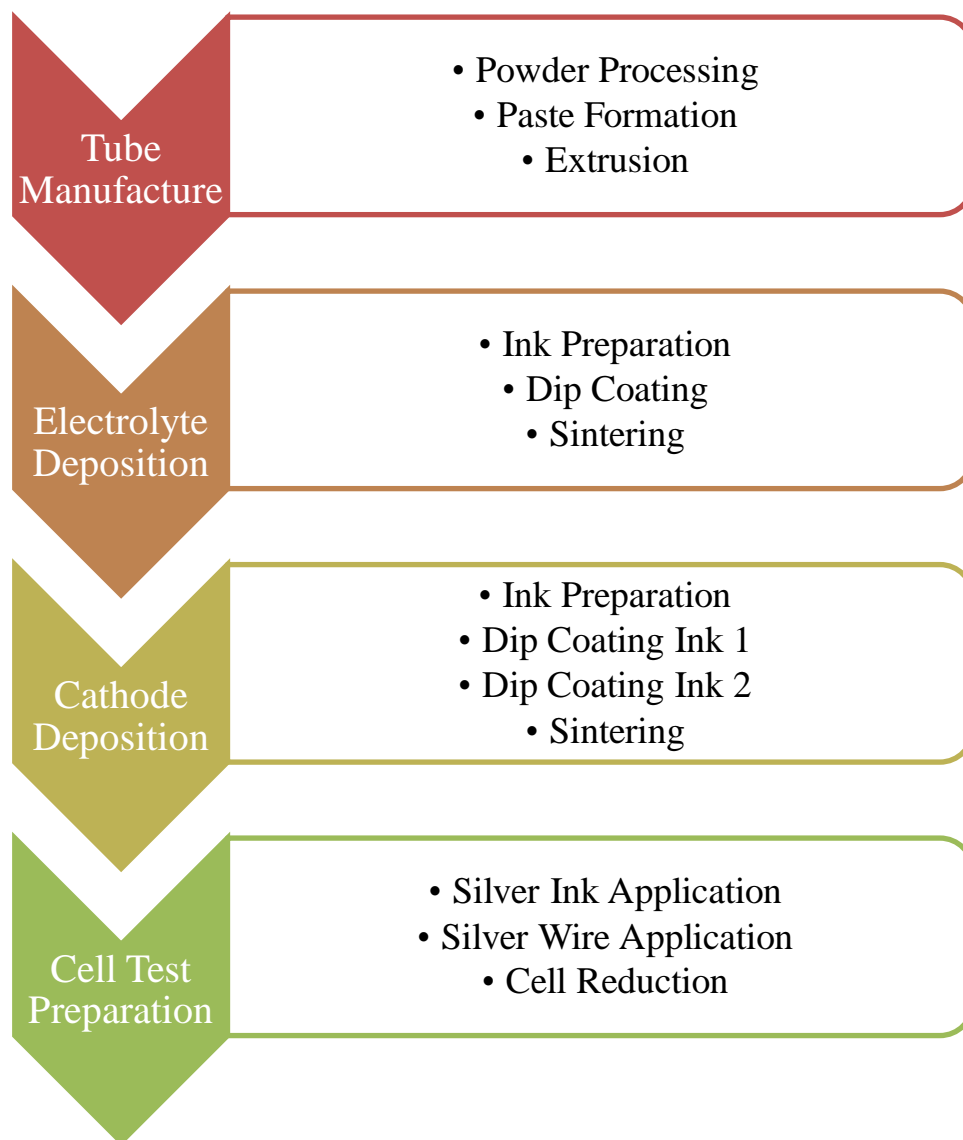


Figure 19. Flow diagram for microtubular solid oxide fuel cell manufacture

## 4.2. Experimental and Results

### 4.2.1. Paste Formation

The first stage of the project detailed in this thesis was to further refine existing techniques so as to develop a manufacturing procedure which would afford reliable and repeatable results with every batch of microtubes produced. The importance of this is two-fold; it allows results to be checked and confirmed empirically, and it reduces waste of some of the potentially expensive and hard-to-manufacture materials that will be used later within the project.

Anode-supported tubes consisting of YSZ ceramic and either nickel oxide, copper oxide or a mixture of both were chosen to be the first batches of tubes to be fabricated. This choice of materials was made due to the fact that YSZ/NiO systems are well studied, meaning that direct comparison with tubes purchased from an industry supplier could be made, and the particle sizes should allow a framework of larger YSZ particles surrounded by smaller NiO particles to form. Copper was chosen to be used as part of the cermet in some batches of cells for several reasons: several studies have shown performance improvements in anodes containing copper when running on methane; also additionally to provide an idea of whether processing techniques could effectively be transferred from a YSZ/NiO system to those containing other materials, with CuO providing a suitable material as it can directly replace NiO as part of the processing precursors, allowing composites containing both copper and nickel to be produced [27, 29, 129, 141]. Table 2 shows the ratios of powders used during initial fabrication. The

YSZ (99.99%) used was from Tosoh, with the NiO (99.9%) from Novamet (grade F) and the CuO (99.995%) from Sigma Aldrich. The average particle size for NiO and CuO were  $\leq 1 \mu\text{m}$  and  $\leq 5 \mu\text{m}$  respectively.

For the purposes of the first extrusion run, 100 g of each sample of cermet material was prepared, to allow for experimentation during the extrusion process. Quantities of powder used can be seen in Table 2.

Sample Reference	A	B	C
YSZ (g)	50	50	50
NiO (g)	50	-	25
CuO (g)	-	50	25

*Table 2. Quantities of powders used to make up the cermet for different samples*

The powders were mixed together within a fume hood until a mixture of uniform colour was obtained before being ball milled in a vibromill for 24 hours, along with 10 alumina milling beads. Vibromilling was chosen as the mixing method for the dry materials as it was shown to have a positive effect on microstructure and mechanical strength of the produced tubes [142]. The solid binder materials were added and mixed using a mortar and pestle before the liquid binders were added. The first batch of powders had binders added in the quantities listed in the prior work [15]. This was found to yield pastes too stiff to easily work with, and so several further batches were prepared using proportionally increased quantities of binding materials up to 150%. It was found that

125% of the literature values was most easy to work with, values shown in Table 3.

Material	Quantity per 100 g cermet
Cyclohexanone (VWR International)	10.5 g
Polyvinyl Butaryl (PVB) (Acros Organics)	9.5 g
Dibutyl Phthalate (Sigma Aldrich)	15 drops
Stearic Acid (BDH Chemicals)	0.125 g

*Table 3. Binder materials used for paste formation*

Binders based on organic solvents, rather than water, were selected for use within this study. This was due to both previous work carried out at the University of Birmingham and also due to the difficulties in producing reliable, straight tubes using water-based binding agents [15, 143].

It is thought that the decreased particle size of the powders used in this thesis against those used by Taylor et al (1  $\mu\text{m}$ /5  $\mu\text{m}$  vs 10  $\mu\text{m}$ ) accounts for why the different quantities of binders were required, as smaller average particle sizes lead to proportionally larger surface areas [15].

#### **4.2.2. Extrusion**

The three samples from the first successful paste batch, 1A, 1B and 1C, were extruded as

described in Chapter 3 to form tubes. However it could clearly be seen that, even when set up as accurately as possible, the equipment used still failed to produce straight tubes with regular wall thicknesses. The die set was inspected and found to be damaged and in need of re-machining. While this equipment was being re-made, the next steps in microtubular SOFC production were carried out on the initial 3 samples as a test of principal, as well as to observe if it was possible to obtain a working fuel cell using the technique.

Tubes were first laid out within straight, smooth channels on wooden drying racks to allow them to harden as straight as possible. After 24 hours they were then fired in a furnace within cylindrical firing tubes, with the firing profile dependant on the cermet materials used. Firing within ceramic firing tubes was found to be necessary to minimise bending of the microtubes upon heating. As CuO would begin to melt out of the tubes at 1083 °C, samples 1B and 1C, containing CuO, were fired at temperatures up to 1200 °C in an attempt to find a balance between keeping the material present and sintering of the YSZ. The reluctance of YSZ to sinter at this lower temperature meant that dwell times needed to be increased in an attempt to prolong the sintering stage. In addition, a variety of final dwell temperatures were investigated to ascertain the difference, if any, on the final product. These profiles are listed in Table 4 and Table 5.

Process	Start Temperature ( °C)	End Temperature ( °C)	Time (mins)
	RT	150	120
Drying	150	150	60
	150	600	450
Debinding	600	600	240
	600	1300/1400	480
Sintering	1300/1400	1300/1400	720
	1300/1400	ambient	180

*Table 4. Firing Profile for sample 1A*

The heating profile used is a slightly modified version to that found in the literature [15]. It was developed complete with slow rises in temperature of around 1 °C per minute in order to minimise cracking of tubes. The profile incorporates drying the microtubes before debinding and then finally sintering, allowing the tubes to stay in position through all steps, in order to minimise mechanical stress before sintering has occurred. Heating rates were kept relatively low in order to minimise thermal expansion of materials causing cracking or delamination.

Process	Start Temperature ( °C)	End Temperature ( °C)	Time (mins)
	ambient	150	120
Drying	150	150	60
	150	600	450
Debinding	600	600	240
	600	1100/1200	480
Sintering	1100/1200	1100/1200	1080
	1100/1200	ambient	180

Table 5. Firing Profile for samples 1B and 1C

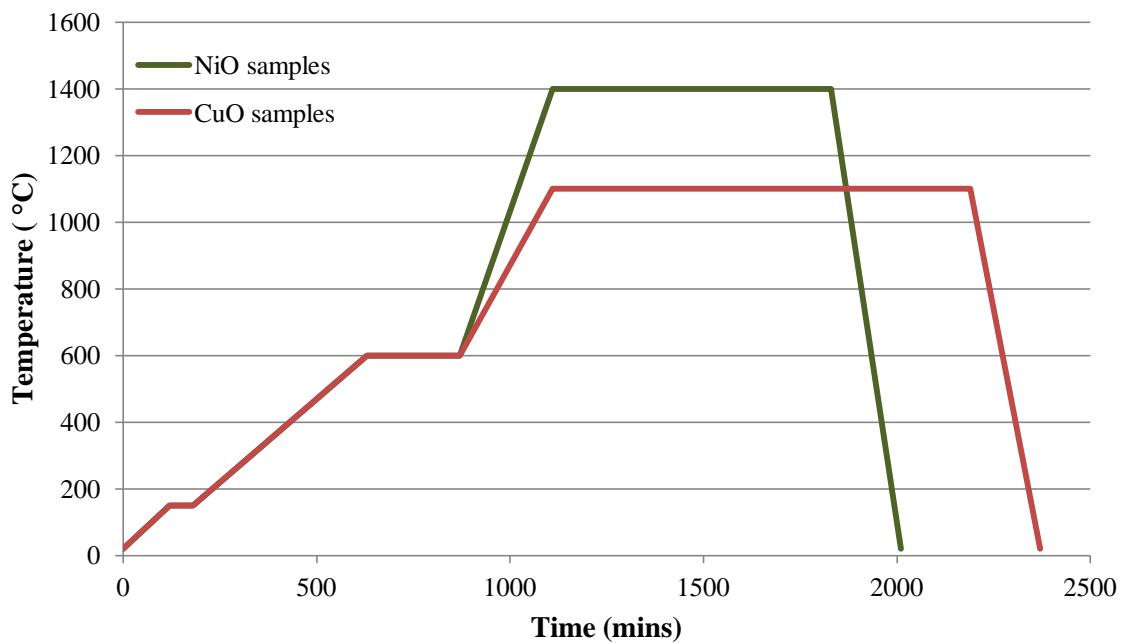


Figure 20. Graph showing sintering profiles for NiO-only samples (batch 1A) and CuO-containing samples (batches 1B and 1C)

Once fired, tubes were inspected for visible cracks or defects caused by heating, and also for melting of the CuO present in samples 1B and 1C. Unfortunately, these copper-containing samples were deemed to have been degraded through the loss of CuO even with the lowered sintering temperatures used, as a significant amount of material had melted onto the firing tubes used within the furnace. In addition the 1100 °C batches remained relatively weak and were prone to snapping easily while being handled. The 1200 °C batches were also difficult to remove from the firing tubes due to increased loss of CuO, which was found to be melting out of the microtubes and causing them to react with the surface of the firing tubes.

The next stage was to deposit an electrolyte layer. Dip-coating was chosen out of the deposition techniques as this was being developed in another project at the University of Birmingham for use on SOFC microtubes bought from a leading microtubular SOFC manufacturer, which were complete apart from the cathode layer, and this study helped to further the technique and ink slurry development [144]. The initial YSZ electrolyte slurry used is listed in Table 6.

Material	Quantity
YSZ (Tosoh)	5 g
Acetone (Sigma Aldrich)	5.5 g
KD2 (Sigma Aldrich)	0.2 g
Terpineol (Sigma Aldrich)	1 mL

*Table 6. Initial composition of electrolyte slurry used for dip coating*

This slurry, along with 10 alumina milling balls, was vibromilled for 24 hours in order to fully mix the materials, and also to reduce the particle size and particle conglomerates. The tubes were prepared for dip coating by sealing and covering a small section of each end in order to leave a section of anode exposed to allow an electrical connection to be made. The YSZ slurry was then dip coated (at a rate of  $0.5 \text{ mm s}^{-1}$ ) onto several tubes from sample 1A, from both the 1300 and 1400 °C sintering groups. A sample of several tubes were dip coated twice in an attempt to determine if the thickness of the electrolyte layer formed had a noticeable effect on the fuel cell performance. Once dipped, these tubes were left for 24 hours to dry. They were then sintered at 1300 or 1400 °C (dependant on their original sintering temperature) for 12 hours.

Second and third slurries were formulated using quantities of YSZ increased by 50%/100%, i.e. 7.5 g and 10 g, while retaining the original quantities of dispersants and solvents. These were formed in the same way, through vibromilling for 24 hours; however, they proved to be too thick to be used easily and so were discarded. These slurries were trialled in order to determine that the maximum level of YSZ was being included so as to deposit an electrolyte layer in a single process, without requiring a second dip. As the initial goal was to achieve a working cell, rather than an optimised cell, having an electrolyte layer thicker than ideal would not be considered detrimental at this early stage.

Cathode layers were then dip coated onto the microtubes. The microtubes that are purchased from a leading microtubular SOFC manufacturer by the Fuel Cell Group at the University of Birmingham consist of anode-support and electrolyte layers and require the

deposition of cathode material. This has led to a standard deposition formula being developed [19, 20, 145]. There are 2 inks used for cathode forming, one which bonds strongly to the YSZ-based electrolyte (cathode ink 1), and the second which then forms a more active layer (cathode ink 2). The formulations can be seen in Table 7.

Material	Cathode Ink 1	Cathode Ink 2
La <sub>0.5</sub> Sr <sub>0.5</sub> MnO <sub>3</sub> (Praxair)	6.5 g	-
La <sub>0.82</sub> Sr <sub>0.18</sub> MnO <sub>3</sub> (Praxair)	-	20 g
YSZ (Tosoh)	6.5 g	-
Acetone (Sigma Aldrich)	0.25 g	0.4 g
Acetone (Sigma Aldrich)	16 mL	14 mL
Triolein (Sigma Aldrich)	0.2 g	-
Terpineol (Sigma Aldrich)	-	2 mL
Milling Beads	12	7

*Table 7. Composition of cathode inks 1 and 2*

These components were measured out before being vibromilled along with 10 alumina milling beads for 24 hours. Both the 1300 °C and 1400 °C NiO/YSZ sintering tubes were coated in the same way. Initially, samples were dip coated in cathode ink 1 at a rate of 0.5 mm s<sup>-1</sup>, then left to dry for 24 hours. Cathode ink 2 was then deposited in the same manner, followed by 24 hours drying time. Both sets of samples were fired at 1200 °C for 12 hours to allow the binding of the cathode layers.

### **4.2.3. Re-Machined Die Set Samples**

Once the die set had been re-machined it was used to fabricate several additional batches of NiO/YSZ tubes. These were formulated in an identical manner to those in batch 1A, including firing at both 1300 °C and 1400 °C, layering with both electrolyte and electrode materials and preparation for cell testing by application of silver ink. These batches will be referred to as batch 2.

The cells produced in batch 2 were more regular than those produced in either batch 1A, 1B or 1C. This regularity was noted through the fact that the tubes extruded using the re-machined die set could be placed within the drying racks with much more ease, with each groove in the rack being ~0.5 mm wider than the width of extruded tubes, indicating a straighter extrusion. However, closer inspection revealed that wall thicknesses still varied, and producing cells with walls of uniform thickness proved very difficult. Many repetitions of the extrusion process were carried out as part of batch 2 but despite these many attempts, including minor variations to the paste formulations and alterations to the extrusion rates, reliable manufacturing of cells using static variables proved impossible.

### **4.2.4. Hot Extrusion Samples**

Several binders were trialled, recommended by the manufacturer of the extrusion equipment and chosen for their different properties upon heating. Polymethylmethacrylate (PMMA) and high density polyethylene (HDPE) were selected

as they both had melting temperatures within the operating window of the equipment used ( $< 300\text{ }^{\circ}\text{C}$ ), were straightforward to source and provided a variation in crystallinity (i.e. they had different softening behaviour on heating, different tensile strengths etc). Mixtures of YSZ and NiO (50:50 by weight) were combined with various proportions of binder, from 50 TO 100 %wt. These were then fed through the Rondol Linear 18 extruder at varying temperatures to ascertain the optimum for tube production.

The ideal quantity of binder for production of even, uniform microtubes was found to be in the region of 50:50 wt of binder to YSZ/NiO mixture for both PMMA and PEHD. PEHD was found easier to work with, as the sharper melting point (i.e. the material softens less up to melting point) allowed the temperature to be set just above the melting point of  $\sim 130\text{ }^{\circ}\text{C}$ , so that the tubes produced hardened faster on exposure to air. However, on sintering using the profile listed above (for both 1A tubes), all tubes produced using both binders were found to have disintegrated. This was postulated as being due to the relatively low proportions of cermet contained within the pre-sintered tubes, approximately 20% by volume, which was insufficient to provide mechanical strength.

Efforts were made to increase the quantity of cermet present in the extruded tubes, while retaining uniform shape. 50 %wt for both binders trialled was found to approach the limit of the equipment; below this threshold, there was too little binder present to allow the paste formed under heating to flow through the die set without exceeding the torque safety limits of the linear screw, even with extrusion temperatures increased in an attempt to confirm that all binder was indeed molten. When using binder quantities

significantly below 50 %wt, the equipment used would seize regardless of the temperature of operation due to having too little binder present to allow the flow of paste. However, even with this reduced binder concentration, the produced tubes disintegrated on sintering. While previous studies have shown that formation of a thin-walled microtube consisting of YSZ was possible using approximately 50:50 wt ratios of binder to ceramic, incorporation of metal oxide powders (such as NiO) weakens the ceramic framework leading to tubes of insufficient mechanical strength [106]. In comparison to the cold extrusion, which allows binders to be present at ~20 %wt (approximately 1:1 by volume) or below, the minimum binder concentration of 50 %wt for hot extrusion using the available equipment was a significant disadvantage and led to the continuation of studies into microtube production by this method to be discontinued.

#### **4.2.5. Cell Testing**

NiO/YSZ tubes from both batch 1A and batch 2 were prepared for performance testing. This involved applying porous silver ink paste (SPI) and silver wire (Silver Wire Company, 99.98%) to act as current collectors, and connecting them to both the anode and cathode. The cell preparation and current connection techniques used were based around those developed by Dhir et al [19, 20]. The size of active area for each cell was calculated by measuring the cathode: the cells produced were typically 1.6 mm in diameter and the active area was 2.5 cm long, giving an active cathode area of approximately 1.0 cm<sup>2</sup>.

Both 1300 °C and 1400 °C sintering tubes from batches 1A and 2 were tested as

complete fuel cells. This involved placing them in a firing tube in a hydrogen/helium atmosphere at room temperature, before raising to 700 °C with a flow of 20 mL min<sup>-1</sup> of H<sub>2</sub>/He and holding for 1 hour to reduce the NiO to nickel metal, followed by testing to obtain information on their performance. Reduction at this temperature and in this fashion has been proven to be an optimum balance between mechanical strength and performance on methane [19, 145]. Once reduced and cooled, microtubes were slotted onto an injection tube which acted to hold the cell in position and also provide fuel to the anode. This injection tube was made from stainless steel and the fuel was provided at a variety of rates between 10 - 50 mL min<sup>-1</sup>. Cells were heated to 800 °C at a rate of 20 °C min<sup>-1</sup>, mirroring testing procedure for the commercial cells. The initial measurements on fuel cell testing, involving determining the open circuit voltage (OCV) and collecting information to build a current-voltage curve (I-V curve) were carried out. The OCV is the voltage recorded with a negligible current drain applied to the cell, with the I-V curve being found through applying different current loads to the cell and recording the voltages achieved.

Both sample groups of cells were able to record an OCV, with little noticeable difference between the two sintering temperatures or batches, most initially recording a value in the region of 1.0 V at 800 °C running on dry hydrogen as a fuel, with a few anomalous exceptions. This indicated a cell that was sealed, with no fuel leaking, as expected with the fabrication techniques used [140].

The testing profile for recording a polarisation curve is to draw incrementally larger currents from the cell and record the output voltage, allowing the curve to be built up

from the data. As the cells were all in the region of  $1 \text{ cm}^2$  active area, and previous studies have shown that commercial cells of similar materials can record current densities in the region of  $0.7 \text{ A cm}^{-2}$  at  $0.5 \text{ V}$ , a test profile involving stepping the current up in increments of  $0.05 \text{ A}$  from OCV was decided upon, with the test being halted once the voltage reached  $0.4 \text{ V}$ . However, neither set of samples was stable enough to withstand the current demands placed upon them during the I-V measurement stage, with output dropping rapidly to the trip voltage. Examples of voltages obtained during this process can be seen in Figure 21, with all cells being from batch 1A in this case.

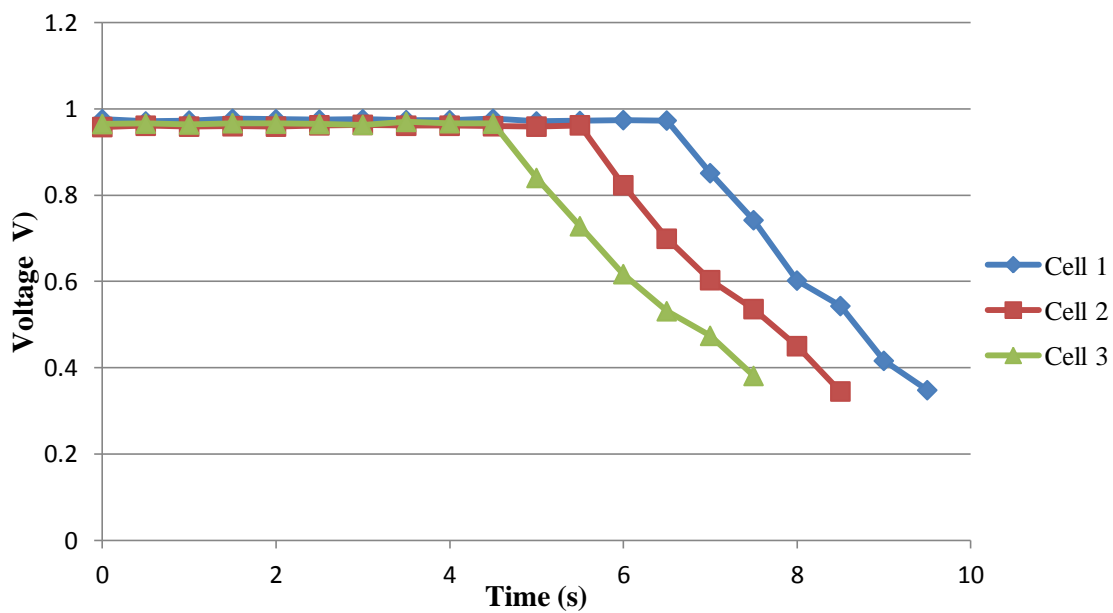


Figure 21. Voltages for cells moving from OCV to  $0.05 \text{ A}$  current demand

As it can be seen, cells recorded show a very rapid decay in voltage as soon as there was a current demand, with the test tripping at the low voltage mark within several seconds. The cells have been offset by 1 second in order to separate the data better, with the current demand being placed on at 7, 6 and 5 seconds respectively. The current demand

was only 0.05 A at this point. Due to the fast voltage degradation, analysis into the cause of the failure of cells was made more difficult; too little data was being recorded to determine what exactly the failure mode was, or to generate a polarisation curve. In addition, once this initial testing had been performed, attempts were made to record OCVs once again, however readings were typically only a few mV, with no cells reaching an OCV above 0.1 V.

The testing profile was then altered to record readings 5 times a second, up from 2 times per second. In addition, the current demand was changed so that it increased in increments of 0.01 A every 10 seconds until the low voltage trip of 0.4 V was reached. Examples of voltages recorded against time through this process for cells from batch 1A can be seen in Figure 22.

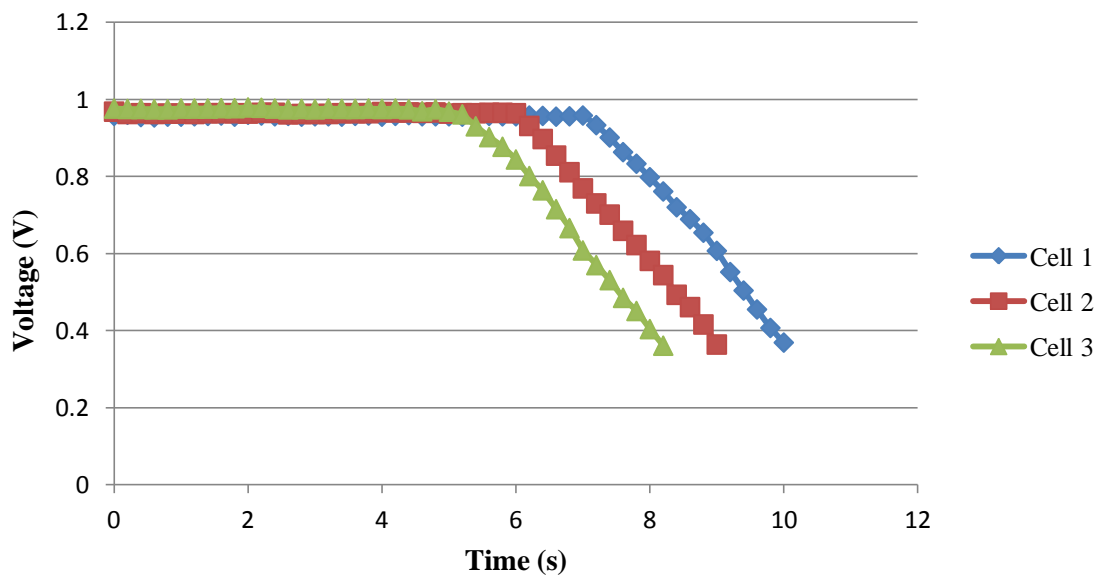


Figure 22. Voltages for cells moving from OCV to 0.01 A current demand

The voltages decay at similar rates for both test profiles, and within 2 seconds of drawing a current the low voltage trip had been reached. Again, analysis of the failure mechanism proved difficult as so little data could be collected before irrecoverable damage to the cells occurred.

An attempt was made to obtain a polarisation curve using voltage control, reading the current produced at different voltages and using this information to create a curve. Again, data were recorded at 5 Hz, with the test profile starting at OCV and changing the voltage demand by 25 mV every 5 seconds from 0.9 V down to 0.45 V. Again, data from cells from batch 1A are shown here.

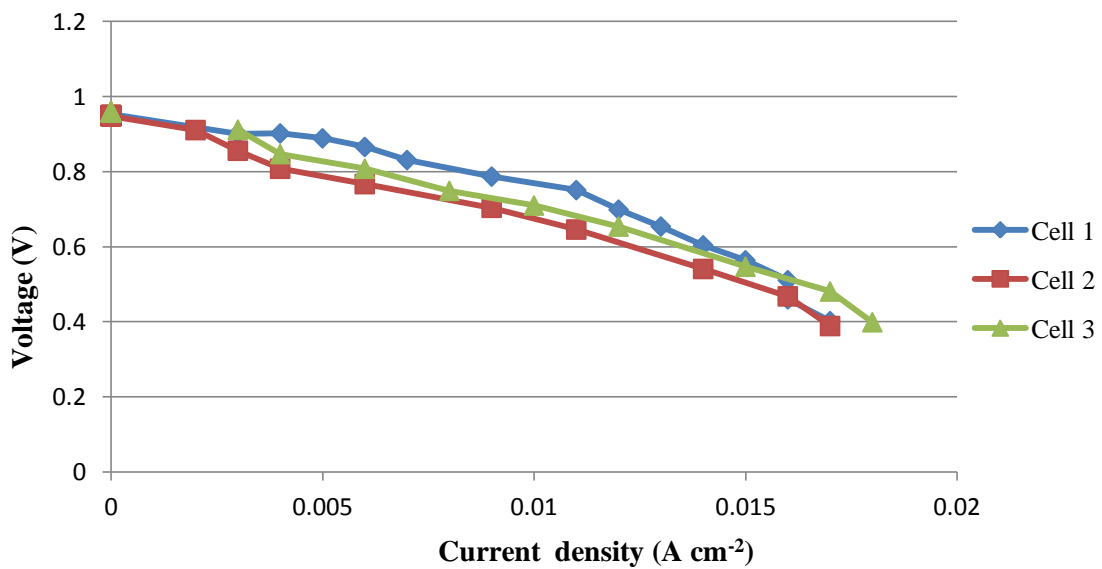


Figure 23. Voltages and currents for cells moving from OCV to 0.9 V voltage demand

As it can be seen in Figure 23, again within several seconds of testing the cell potential drops and hits the trip point. This being despite drawing a specific voltage instead of a current, attempting to allow the cell to reach a power which allows the cell to remain

stable. It should be noted that, under all settings used here, the measurement error is 10 mV / 5 mA over the range of readings, meaning that the results shown above in Figure 23 have potentially large errors.

This was initially put down to the unreliable and damaged extrusion equipment not producing regular tubes, which could therefore not withstand the thermomechanical stresses which occur at the operating temperature and conditions for a SOFC. After the tests, the tubes were carefully inspected. There was no visible damage to any cells, with no obvious cracks or leaks, although it was apparent that cells were considerably more brittle and fragile after exposure to fuel cell conditions than before. This was shown by several cells breaking during handling and disconnection from the test rig, something which did not occur at all during preparation for cell testing.

Analysis by SEM of cells at a variety of production stages was carried out in order to view the microstructure of materials and determine whether any obvious weaknesses could be identified which may be contributing to the poor stability displayed in cell testing.

#### **4.2.6. SEM Imaging**

Tubes from batches 1A, 1B and 1C along with batch 2 (those fabricated using the re-machined die set) were analysed using a scanning electron microscope, as detailed in Chapter 3. Images obtained can be seen in Figure 24.

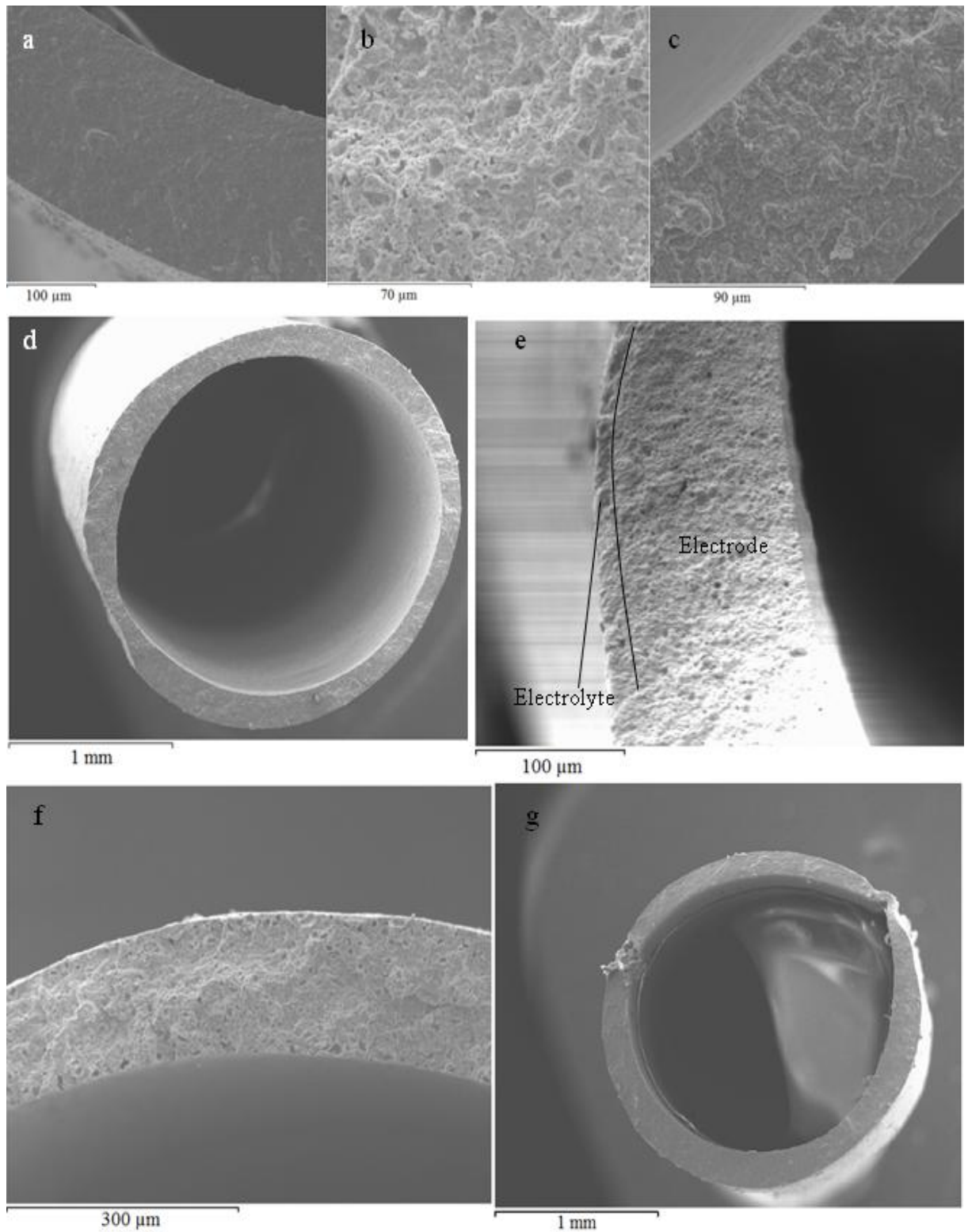


Figure 24. SEM images of tubes extruded of various batches and in various states of production. *a* = YSZ-NiO-CuO as extruded, *b* = YSZ-CuO debound and sintered at 1100 °C, *c* = YSZ-NiO debound and sintered at 1400 °C, *d* = YSZ-CuO as extruded, *e* = YSZ-

*NiO debound and sintered at 1300 °C then YSZ electrolyte deposited and sintered at 1300 °C, f = YSZ-NiO debound and sintered at 1100 °C, g = YSZ-NiO as extruded*

As it can be seen in Figure 24a, before the thermal removal of the binder the anode layer, which the tube is comprised of, is almost completely non-porous. The wall thickness here can be seen to be approx. 200  $\mu\text{m}$ . There is little noticeable difference across the thickness of the cell wall, with few large agglomerate particles over 10  $\mu\text{m}$  diameter. Figure 24b shows a close up image of a sample B tube wall after it has undergone the thermal removal of the binder and sintering at 1100 °C. It can be clearly seen that the porosity has increased over the sample seen in Figure 24a, before debinding and sintering. The loss of the binding agents used accounts for the increased porosity.

Figure 24c shows the decrease in porosity in samples sintered at higher temperatures, due to increased YSZ sintering and NiO agglomeration. A noticeable difference can be seen between Figure 24b and Figure 24c, showing the decrease in sample porosity due to the increased sintering temperatures used. This additional sintering has partially counteracted the pore-forming effect of removing the binding agents. The wall thickness can be seen here to be approx. 150  $\mu\text{m}$ .

Figure 24d shows the full profile of a tube manufactured from a batch of sample B paste. As with Figure 24a it can be seen that the walls are non porous; however, it is clear that the thickness of the wall varies quite dramatically at different points around the tube. This range is between 75 - 200  $\mu\text{m}$ . In addition, the tube is not perfectly round, even before undergoing thermal binder removal and sintering, which may lead to further

deformation as in Figure 24g.

Figure 24e shows the tube wall of a cell after coating with a YSZ electrolyte layer. The thin electrolyte layer can be seen on the outside of the cell wall and is easily distinguished from the more porous anode layer. The overall wall thickness shown here is in the range of 100 - 150  $\mu\text{m}$ , with the electrolyte layer in the region of 10 $\mu\text{m}$ .

Figure 24f shows the semi-porous wall structure as caused by the thermal removal of the binder. The difference between Figure 24d and Figure 24f is noticeable, with a significant increase in porosity. The wall thickness here can be seen to be in the range of 150 - 200  $\mu\text{m}$ .

However, Figure 24g shows the unreliable nature of the extruded tubes. As can be seen, the walls are not of a uniform thickness, nor are the tubes round. In addition, the tube wall is at one point very close to splitting completely, with a thickness of approximately 25  $\mu\text{m}$ . This deformation was a common occurrence and through many extrusion runs and SEM sessions it proved difficult to identify a sample which displayed a round, uniform profile. However, it should be noted that deformities such as that present on the upper left side of the tube pictured in Figure 24g may be due to the cell having been snapped in the preparation process for SEM analysis.

The lack of reliability of formed tubes has implications for full fuel cell testing. With tubes having irregular wall thicknesses and shapes, thermal stability of samples may be seriously compromised. In addition, achieving repeatable results is made considerably

more unlikely without a repeatable method of tube production.

#### **4.2.7. Further Extrusion Work**

Once the die and ram set had been re-made, further extrusion work was carried out. Multiple batches of YSZ/NiO paste were formulated as per above, however it proved very difficult to extrude tubes of uniform wall thickness. It was noticeable that the re-machined die set was easier to align, however once the alignment cylinder had been displaced by extrudate the ram became misaligned almost immediately. Many procedural modifications were made with the aim of improving tube shape. Paste batches were formulated which had lower concentrations of binder materials, consequently making them stiffer in an attempt to prevent the mandrel from becoming misaligned. Rates of compression for the load cell were varied between 0.5 - 10 mm min<sup>-1</sup> with a variety of paste binder concentrations, also in an attempt to prevent the mandrel from becoming misaligned and to try to increase the length of tube extruded before misalignment occurred. However it still proved impossible to form repeatable, reliable tubes of uniform profile.

Nevertheless, samples of extruded tubes were prepared for fuel cell testing using the methods detailed above. However, these suffered from the same rapid degradation even without a load on the cell, with OCV recorded dropping after a maximum of 15 minutes to under 100 mV. Consequently, it was decided to vary the electrolyte and cathode layer deposition techniques in order to attempt to counteract this failure and to verify that thermomechanical stresses were the more likely cause of the problem, rather than layer

formation. As tubes purchased from commercial sources came pre-prepared with an electrolyte layer, the cathode deposition technique was known to be successful through painting the ink onto the cell by hand and so this was to be repeated on this third batch of cells.

To this end, electrolyte layers were deposited using spray deposition. The ink utilised for electrolyte dip coating (see Table 6) was found to be suitable for use with the equipment available, being thin enough to avoid blocking the spray nozzle. Tubes (which had undergone debinding and sintering at 1400 °C) were again sealed at both ends and attached to a custom-made rig which span the sample at a uniform rate in an attempt to deposit ink over the cell at a constant rate. Batches of samples were prepared, which had one, two and three separate coatings of electrolyte slurry, and which were left to dry for 1 hour between applications. These were sintered at 1400 °C for 12 hours before having cathode inks applied via the dip-coating technique and being treated in the normal in-house fashion for m-SOFCs within the research group. Cells were prepared for fuel cell testing as described above, with silver ink and silver wire used for current collection purposes. Tubes were pre-reduced at 700 °C in H<sub>2</sub>/He for 1 hour before fuel cell testing.

It was found that these cells also underwent rapid degradation in the same way as the dip-coated electrolyte cells, with OCVs initially in the region of 1.0 V, but dropping to negligible values after attempting I-V measurement testing and also when running at OCV for longer than 10 - 15 minutes. This furthered the speculation that the electrolyte layer deposition technique was not at fault for the rapid performance drop, as several different techniques had led to the same result. Examples of attempts to draw power from

cells can be seen in Figure 25, where a voltage demand of 0.9 V was placed on the cells. Once again, data was recorded at 5 Hz to try to obtain a better insight into the cell behaviour.

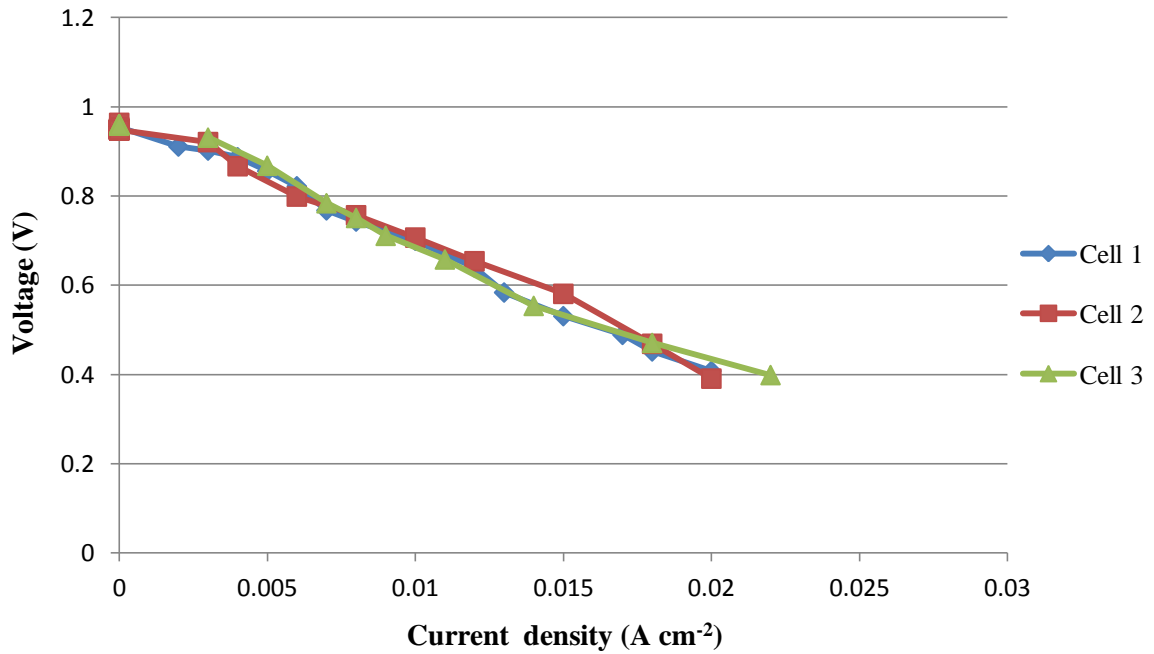


*Figure 25. Voltages and currents for cells (extruded using the remanufactured die set) moving from OCV to 0.9 V voltage demand*

Samples were also prepared which had the electrolyte layer applied by depositing an ink by hand. The ink formulation used in Table 6 was found to be too thin to easily apply using a paintbrush so a formulation with 50% increased YSZ content (over the spray deposition ink) was produced using the same process described above. The composition of this can be seen in Table 8.

Material	Quantity
YSZ	7.5 g
Acetone	5.5 g
KD2	0.2 g
Terpineol	1 mL

*Table 8. Composition of electrolyte slurry used for manual deposition*

This thicker electrolyte slurry was applied to YSZ/NiO tubes that had undergone debinding and sintering at 1400 °C. Several different batches were produced, some of which had just a single layer of electrolyte ink deposited and others which had two or three layers applied with an hour drying time between applications. These were sintered at 1400 °C for 12 hours. Cathode inks were then applied in the same manner as previously carried out and sintered at 1200 °C for 12 hours. Silver wire and silver ink was attached to the anode and cathode layers to act as current collectors. The tubes were again pre-reduced at 700 °C in H<sub>2</sub>/He for 1 hour.

Once again, the OCV performance was reasonable, however the performance while recording I-V curves rapidly dropped off once in operating conditions. The electrolyte layer applied to the hand painted samples should be considerably thicker than those deposited using either dip coating or spray coating. This should lead to lower performance than those other techniques due to the increased resistance to oxide conductivity, however this increased thickness should ensure that the cell is not short circuiting and that the anode and cathode layers remain better separated. Unfortunately,

the repetition of previous results remained, with cells failing to provide a constant OCV and rapidly dropping to under 100 mV.

Heating rates were investigated, and lowered to reduce thermomechanical stress, from 20 °C min<sup>-1</sup> down to 10 °C min<sup>-1</sup> then finally 5 °C min<sup>-1</sup> with no noticeable difference in cell longevity. Experiments were also performed which lowered the operating temperature to 700 °C, again with no noticeable difference on cell longevity or performance. Fuel flow rates were also varied between 10 - 50 mL min<sup>-1</sup> and cell tests were carried out using both dry and wet hydrogen. Unfortunately none of these variables managed to overcome the microtubes failing rapidly.

The aim of the extrusion work within this project was to develop a technique which provided reproducible results to allow both the University of Birmingham to become more self-sufficient in microtube production, as well as to also allow the direct comparison of novel anode materials against established SOFC materials. It can then be seen that most variables for the tube production and preparation were altered without success. The overall shape of the extruded tubes proved difficult to control, leading to an overall production technique which could not be thought of as repeatable or reliable. Furthermore, the inability of the tubes to allow significant load to be drawn from them showed major issues with the cell production. This combination of factors was instrumental in the decision to discontinue research into microtube production and instead focus on the synthesis and characterisation of novel materials for SOFCs. While material synthesis made up a significant proportion of the original project goals, this shift led to much less focus on the comparison between novel and established SOFC materials

using in-situ analysis and instead moved further into fundamental material characterisation.

#### **4.8. Further Work and Conclusions**

Varying the set up of the equipment for m-SOFC testing allows small button cells to be analysed. Fabricating cells in this geometry may allow crude comparisons of materials; however, difficulties in repeatable layer thicknesses, cell sealing and material porosity are problems to be overcome and all will affect cell outputs. Testing the resistance of cells produced through the extrusion technique listed here may help to further elucidate the cause of the poor IV performance of cells produced, which may be due to a very high cell resistance. In addition, 3-point stress tests would assist in quantifying the mechanical strength of the cells produced, both before and after reduction, which may help to determine the root of the problem of this extrusion work. Alternatively, current collection may be an issue as this is something that is a major problem in SOFC development.

# **Chapter 5. Synthesis and characterisation of Si doped**

## **SrFeO<sub>3-δ</sub> for both cathode and anode applications**

### **5.1. Introduction**

Perovskite materials containing transition metals have been widely investigated for potential use with SOFCs, although the majority of the research has focused on cathode applications. As a family of materials they show a wide range of favourable properties from catalytic activity through to high electronic and ionic conductivity. These properties also make them potential anode materials, which may allow the use of anodes which do not contain nickel. This would have the potential to allow SOFCs to run directly on hydrocarbon fuels without the need for as much fuel pre-cleaning, in particular the removal of H<sub>2</sub>S. Several perovskite-type materials have been investigated for use as SOFC anodes, such as Sr<sub>2</sub>MgMoO<sub>6</sub>, La<sub>0.75</sub>Sr<sub>0.25</sub>Cr<sub>0.5</sub>Mn<sub>0.5</sub>O<sub>3-δ</sub>, Sr<sub>1-x</sub>Ti<sub>1-2x</sub>Nb<sub>2x</sub>O<sub>3</sub> and others [35, 50, 60, 146–148].

Perovskite type SrFeO<sub>3-δ</sub>, has been shown to have high mixed ionic and electronic conductivity, and has been proposed as a potential material for use in oxygen sensors, SOFCs and other electrochemical applications [149–151]. It has been demonstrated to have the highest conductivities when the unit cell is cubic, a phase which is only stable at elevated temperatures [152–154]. SrFeO<sub>3-δ</sub> contains mixed valence iron cations (average oxidation state between 3 and 4) has a range of oxygen nonstoichiometry, undergoing a structural change leading to long-range oxygen ion vacancy ordering as iron reduces

towards  $\text{Fe}^{3+}$  [155–157]. This shift towards a brownmillerite-type structure is detrimental for both the oxide ion and electronic conductivity [158, 159]. This work, therefore, had the aim of stabilising the cubic form of strontium ferrate in both oxidising and reducing atmospheres, so as to increase the overall conductivity performance.

The majority of the doping strategies for perovskite materials have focused on replacing cations with those of similar size e.g. Mo for Cr, Co for Fe [24, 134, 160–162]. Previous work examining doping various oxyanion species (such as carbonate, sulphate, phosphate, borate) into perovskite systems has shown that incorporation into the perovskite crystal structure is possible [91, 152–154, 163–167]. Another potential oxyanion dopant is  $\text{SiO}_4^{4-}$ . In this respect, Si is often thought of as detrimental to oxygen conductivity and cell performance within SOFC systems, as in fluorite structures such as YSZ it collects at grain boundaries and inhibits oxide ion transport [108, 168, 169]. Relatively recently, work has been carried out to determine the effect on conductivity of the inclusion of  $\text{SiO}_4^{4-}$  oxyanion or other tetrahedral oxyanions species within perovskite materials to investigate the effect on performance [66, 167, 170]. In this respect, previous work on other perovskite electrode systems has shown that doping with Si caused the packing arrangement of  $\text{SrMO}_3$  ( $\text{M}=\text{Co}, \text{Mn}$ ) to change from face-sharing octahedra to corner-sharing octahedra, and a decrease in oxygen vacancy ordering [170]. Undoped  $\text{SrFeO}_{3-\delta}$  already contains corner-sharing octahedra so this packing arrangement change is not expected in this case, however the aim of this work was to inhibit the ordering of oxygen vacancies on reduction and so increase the conductivity over the undoped samples.

To this end, Si has been successfully incorporated into the perovskite structure to form  $\text{SrFe}_{1-x}\text{Si}_x\text{O}_{3-\delta}$  [171]. The work presented within this thesis investigates the effect on the structure and conductivity of the new materials, along with electrode area specific resistance (ASR) and thermal expansion coefficient measurements. The conductivity behaviour in both air and reducing atmospheres was examined to determine the potential for use as either anode or cathode SOFC materials.

## 5.2. Experimental

Stoichiometric quantities of high purity powders of  $\text{SrCO}_3$ ,  $\text{Fe}_2\text{O}_3$  and  $\text{SiO}_2$  were ground intimately before being heated to 1100 °C for 12 hours. Samples were then ball milled (Fritsch Pulverisette 7 Planetary Mill for 1 hour at 350 rpm with 2 milling beads) and heated to 1200 °C for a further 12 hours. Powder X-ray diffraction (Bruker D8 autosampler diffractometer using  $\text{Cu K}\alpha_1$  radiation) was carried out to determine phase purity and calculate cell parameters. Unit cell parameter refinement was carried out using GSAS suite of programs [123, 124].

For conductivity measurements, powders were again ball milled (Fritsch Pulverisette 7 Planetary Mill for 1 hour at 350 rpm with 2 milling beads) before being pressed as pellets of 13mm diameter and sintered at 1200 °C for 12 hours. Platinum electrodes were then attached using platinum paste (Metalor) and fired at 800 °C for 1 hour then held at 350 °C for 12 hours to ensure both bonding the Pt and full oxygenation of the samples. 4 probe D.C. conductivity measurements were then taken in both air and 5% $\text{H}_2/\text{N}_2$  at temperatures up to 800 °C.

For TGA experiments, a small quantity of the sample was accurately weighed. This was then subjected to a heating profile of  $10\text{ }^{\circ}\text{C min}^{-1}$  to  $1200\text{ }^{\circ}\text{C}$  in  $\text{N}_2$  followed by a holding stage at  $1200\text{ }^{\circ}\text{C}$  for 30 minutes in order to reduce the Fe oxidation state to 3+. The average Fe oxidation state for the sample could then be determined from the mass loss observed.

For ASR measurements, ink suspensions were prepared containing 1:1 wt% of electrolyte and electrode materials with 20% wt Decoflux (Zschimmer and Schwarz) to act as a dispersant and binder. These inks were then ball milled (Fritsch Pulverisette 7 Planetary Mill for 1 hour at 350 rpm with 2 milling beads) and coated onto dense pellets of  $\text{Ce}_{0.9}\text{Gd}_{0.1}\text{O}_{1.95}$  (CGO10, Aldrich, presintered at  $1500\text{ }^{\circ}\text{C}$  for 12 hours) to form a symmetrical cell and then fired at  $1000\text{ }^{\circ}\text{C}$  for 1 hour. Pt paste was then applied to both sides to act as a current collector and heated at  $800\text{ }^{\circ}\text{C}$  for 1 hour. ASR values were obtained in both cathodic (air) and anodic ( $5\%\text{H}_2/\text{N}_2$ ) conditions at temperatures up to  $800\text{ }^{\circ}\text{C}$  (air) /  $600\text{ }^{\circ}\text{C}$  ( $5\%\text{H}_2/\text{N}_2$ ). Impedance data were collected between 5 Hz - 13 MHz with an AC signal amplitude of 100 mV (HP 4912A Frequency Analyser). The spectra were plotted using ZView software [127].

Samples prepared for dilatometry measurements were ball milled as powders (Fritsch Pulverisette 7 Planetary Mill for 1 hour at 350 rpm with 2 milling beads) before being pressed into thick pellets of 10 mm diameter and approximately 10 mm length. These were sintered at  $1200\text{ }^{\circ}\text{C}$  for 12 hours and then polished to form smooth, flat ends. Dilatometry data were obtained using a Netzsch 409C dilatometer, running a profile from  $25\text{ }^{\circ}\text{C}$  to  $1000\text{ }^{\circ}\text{C}$  at  $15\text{ }^{\circ}\text{C min}^{-1}$  in an atmosphere of air.

For fuel cell testing, electrode inks were prepared with the same formula as that used for ASR testing; 1:1 wt% of electrolyte and electrode materials with 20 wt% Decoflux added. Pellets of ~200  $\mu\text{m}$  thickness of CGO10 and  $\text{Y}_{0.15}\text{Zr}_{0.85}\text{O}_2$  (YSZ8, UCM Advanced Ceramics) were prepared using a die of 13 mm diameter before being sintered at 1500 °C for 12 hours. The 10% Si doped  $\text{SrFeO}_{3-\delta}$  ink was painted onto both sides of these pellets and fired at 1000 °C for 1 hour, before being painted with porous silver ink (SPI) and having silver wire attached to act as current collector. The cells were then attached onto an alumina firing tube with internal diameter of 10 mm, external 15 mm, using ceramabond (Aremco) and left to set for 6 hours. The firing tube was placed within a modified tube furnace, with a length of Swagelock<sup>®</sup> tubing running down the centre. This tubing was used to supply the setup with hydrogen, with the inner face of the pellet acting as the anode side of the cell and the outer face acting as the cathode side. Open circuit voltages were obtained using a Solatron 1400A/1470E instrument, with the data processed using the Multistat suite of software [172].

## **5.3. Results and Discussion**

### **5.3.1. Synthesis and Structure Determination**

Figure 26 and Figure 27 show the XRD patterns for the series  $\text{SrFe}_{1-x}\text{Si}_x\text{O}_{3-\delta}$ . X-ray diffraction data showed that incorporation of Si for Fe was possible up to 15 % mol; above this level small  $\text{Sr}_2\text{SiO}_4$  peaks appeared showing that the lattice solubility limit

had been exceeded. It can also be seen that the unit cell changes from tetragonal to cubic upon doping with Si which corresponds to the disordering of oxygen vacancies.

Si mol %	0	5	10	15
a (Å)	10.9235	3.8636	3.8723	3.8755
c (Å)	7.6965	= a	= a	= a
Volume (Å <sup>3</sup> ) per formula unit	57.40	57.67	58.06	58.34

Table 9. Unit cell parameters and volumes (per formula unit) for the series  $SrFe_{1-x}Si_xO_{3-\delta}$

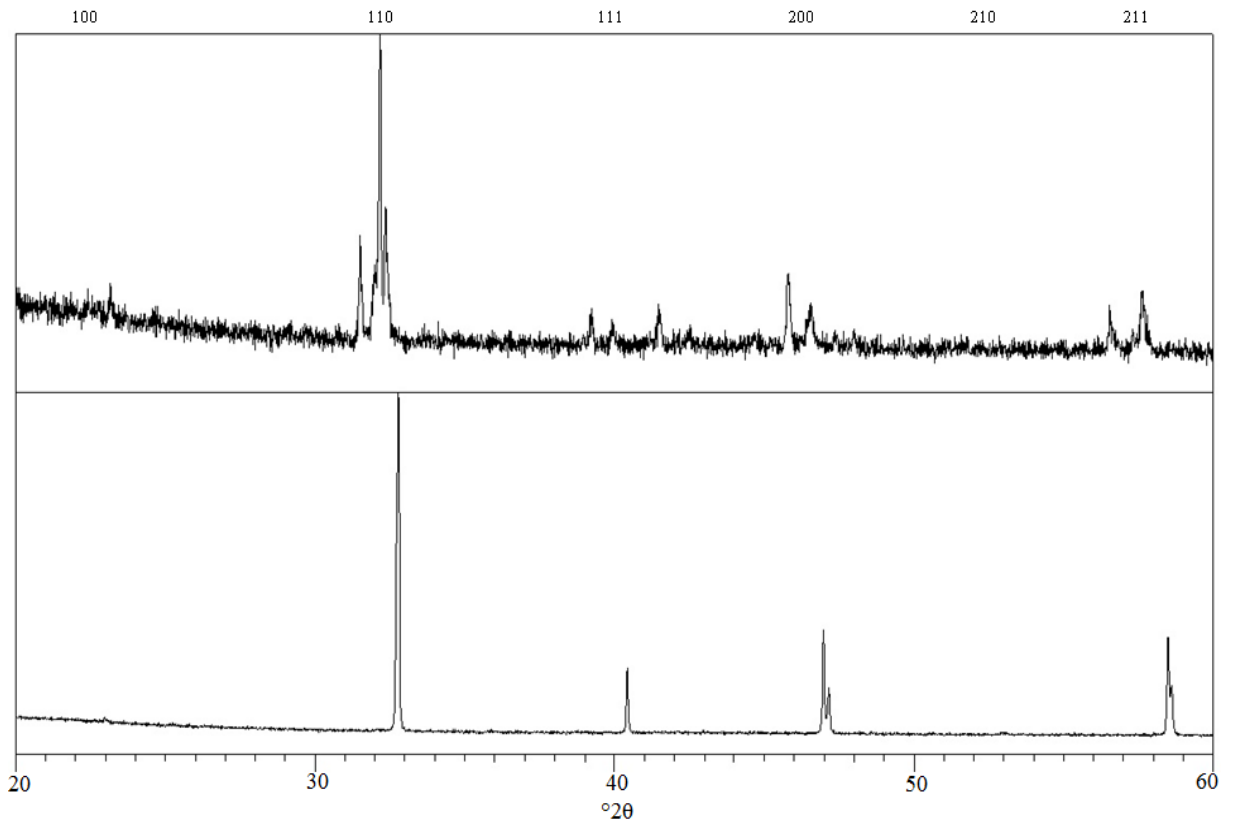


Figure 26. XRD pattern for  $SrFeO_{3-\delta}$  in air (bottom) and annealed in 5% $H_2/N_2$  at 600 °C for 24 hours (top)

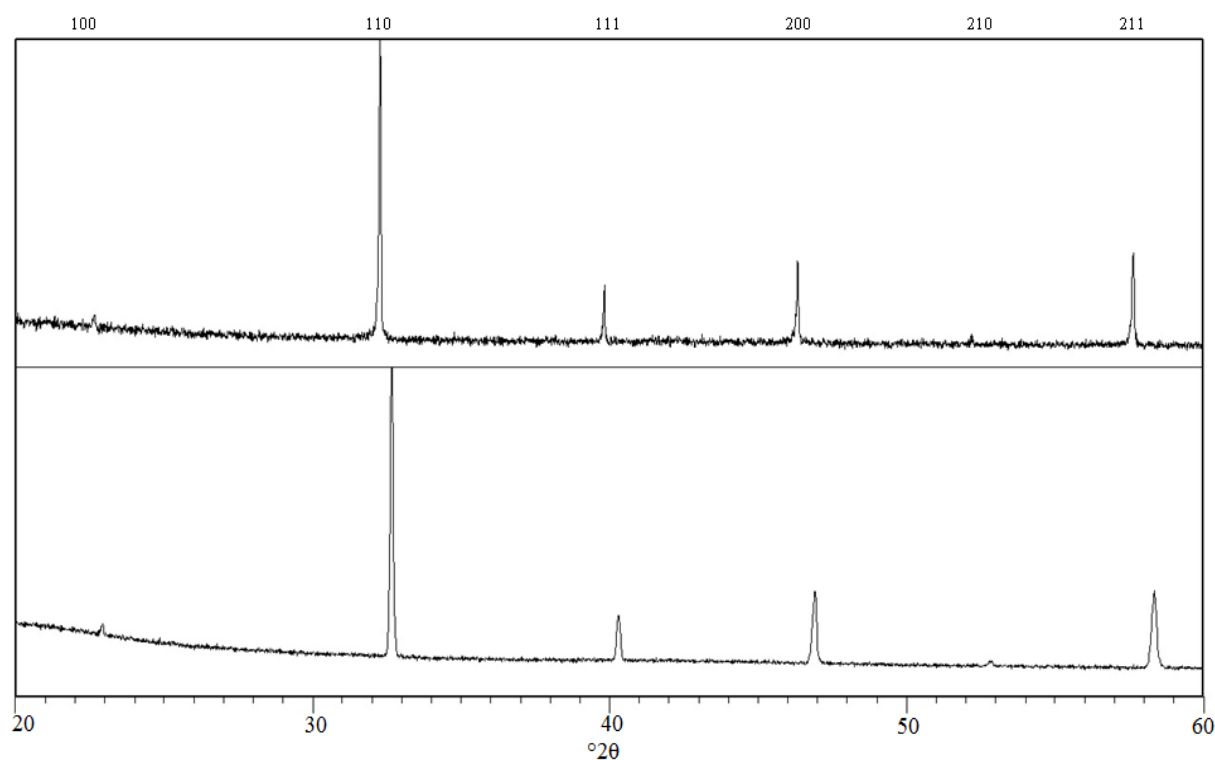


Figure 27. XRD pattern for  $\text{SrFe}_{0.9}\text{Si}_{0.1}\text{O}_{3-\delta}$  in air (bottom) and annealed in 5% $\text{H}_2/\text{N}_2$  at 600 °C for 24 hours (top)

Table 9 displays the unit cell volumes per formula unit for the series  $\text{SrFe}_{1-x}\text{Si}_x\text{O}_{3-\delta}$ . A trend of increasing cell volume with increasing Si content was noticed. This has also been previously reported for Si doping in Mn perovskites [170, 173] but is unusual as  $\text{Si}^{4+}$  is smaller than either the  $\text{Fe}^{3+}$  or  $\text{Fe}^{4+}$  it replaces, with tetrahedral Si having an ionic radius of 0.26 Å against octahedral  $\text{Fe}^{3+}$  at 0.645 Å and  $\text{Fe}^{4+}$  at 0.585 Å [173, 174]. This increase in cell parameter is attributed to the introduction of Si leading to a reduction of  $\text{Fe}^{4+}$  to  $\text{Fe}^{3+}$ . This can be explained by the strong tetrahedral coordination preference of Si which ensures the introduction of oxygen vacancies and hence partial reduction of iron according to the Kröger-Vink notation equation below:

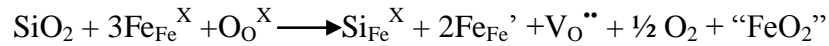


Figure 28. Kröger-Vink notation showing silica incorporation causes oxygen vacancies and Fe reduction

It should also be noted that it has been similarly reported in the literature that incorporation of a cation with a smaller or similar ionic radius than iron, such as  $\text{Al}^{3+}$ ,  $\text{Ga}^{3+}$  and  $\text{Mo}^{6+}$ , also leads to an increase in the unit cell size, and this was also attributed to the lowering of the proportion of  $\text{Fe}^{4+}$  [175, 176].

Si mol %	0	5	10	15
Fe Oxidation State	3.80	3.60	3.48	3.42
Oxygen Deficiency ( $\delta$ )	0.10	0.20	0.23	0.25

Table 10. Oxidation state and oxygen deficiencies for the series  $\text{SrFe}_{1-x}\text{Si}_x\text{O}_{3-\delta}$

Confirmation of the reduction in the average iron oxidation state was shown by TGA studies. This was carried out by accurately weighing a sample before heating at  $10^\circ\text{C min}^{-1}$  to  $1200^\circ\text{C}$  in  $\text{N}_2$ , and holding for 30 minutes, in order to reduce the iron present to  $\text{Fe}^{3+}$ . The weight loss experienced by the sample is attributed to the loss of oxygen and can be used to calculate the original oxidation state of the iron. The values obtained are shown in Table 10. It was found that as the Si content is increased the number of oxygen vacancies increased and the average oxidation state of iron decreased.

In order to examine the stability in strongly reducing conditions, XRD patterns of samples were recorded after reduction at 600 °C in 5% H<sub>2</sub>/ 95% N<sub>2</sub>. This showed that the undoped SrFeO<sub>3-δ</sub> changed structure from tetragonal to the brownmillerite-type orthorhombic Sr<sub>2</sub>Fe<sub>2</sub>O<sub>5</sub>, with contains ordered oxide ion vacancies (see Figure 26). This was in contrast to the doped samples which remained as cubic systems, indicating that disordered vacancies were still present. Thus Si doping has been demonstrated to increase long range oxide ion vacancy disorder under both oxidising and reducing conditions.

### **5.3.2. Electrical Conductivity Measurements**

Electrical conductivity measurements were taken for several SrFe<sub>1-x</sub>Si<sub>x</sub>O<sub>3-δ</sub> samples ( 0 ≤ x ≤ 0.15) using 4-probe DC conductivity analysis. Measurements were carried out in both air and 5%H<sub>2</sub>/N<sub>2</sub> to examine the potential for use as cathode and anode SOFC materials respectively.

#### **5.3.2.1. Air Atmosphere**

Conductivity measurements were carried out on dense sintered pellets of x = 0, 0.05, 0.1, 0.125 and 0.15 and the results are shown in Figure 29 and Table 11. It was observed that conductivity was highest for the x = 0.1 sample at 24.1 S cm<sup>-1</sup> at 800 °C and 35.3 S cm<sup>-1</sup> at 700 °C, with both the higher and lower Si doped samples recording lower values. The initial improved conductivity on Si doping may either be attributed to the change from a

tetragonal to a cubic system, leading to an improvement in conduction pathways, or be due to changes in the Fe oxidation state.

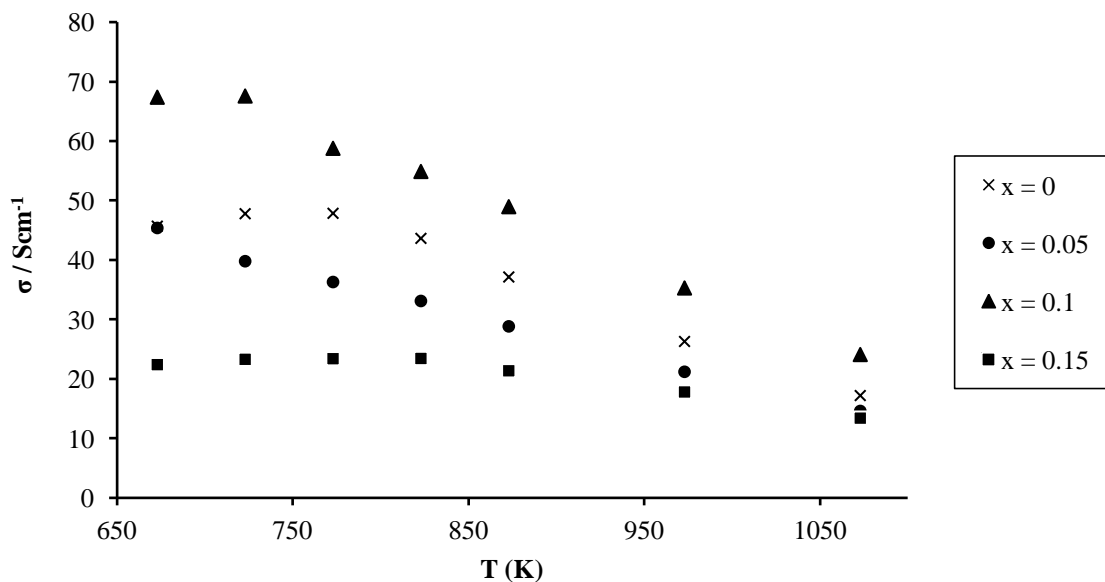


Figure 29. Plot of conductivity against temperature for the series  $SrFe_{1-x}Si_xO_{3-\delta}$  in air

Si mol %	0	5	10	15
800 °C (S cm <sup>-1</sup> )	17.2	14.6	24.1	13.4
700 °C (S cm <sup>-1</sup> )	26.3	21.2	35.3	17.8
600 °C (S cm <sup>-1</sup> )	37.2	28.8	49.0	21.4
500 °C (S cm <sup>-1</sup> )	47.9	36.3	58.8	23.4
400 °C (S cm <sup>-1</sup> )	45.7	45.4	67.4	22.4

Table 11. Conductivity data for  $SrFe_{1-x}Si_xO_{3-\delta}$  in air

As the Si doping is increased further, the lowering of the conductivity is postulated as being due to the increasing concentration of the silicate oxyanion interrupting the Fe-O conduction network. All samples showed an increase in conductivity to 400 °C, a relatively stable conductivity in the temperature range 400 - 600 °C, and a decrease at higher temperatures. The loss of oxygen above 400 °C is most likely accountable for this drop in conductivity above these temperatures as the average oxidation state of Fe is reduced, although it is partially counterbalanced through the semiconductor behaviour leading to increasing hole mobilities with increasing temperatures. Overall, these conductivities compare favourably with literature examples, for example LSCM has been shown to have total conductivity at 900 °C in air of  $38.6 \text{ S cm}^{-1}$  [49].

#### **5.3.2.2. 5% $\text{H}_2/\text{N}_2$ Atmosphere**

Table 12 and Figure 30 display the conductivity data for the series under 5%  $\text{H}_2/\text{N}_2$ . In these conditions, the reduction of the average oxidation state of iron towards  $\text{Fe}^{3+}$  above 400 °C causes a large drop in the conductivities of the samples analysed. Once again, the  $x = 0.1$  sample shows the highest level of conductivity with the lowest results posted for  $x = 0$  and 0.05 samples. This in part can be attributed to the  $x = 0$  and 0.05 samples not being fully stabilised cubic systems and so forming the brownmillerite-type phase ( $\text{SrFe}_{1-x}\text{Si}_x\text{O}_{2.5}$ ) on reduction. On increasing the temperature further, an increase in conductivity was observed for all samples, which may result from mixed  $\text{Fe}^{3+}/\text{Fe}^{2+}$  valence, although the conductivities were still lower than the values in air. This behaviour can be seen in literature examples of MIEC systems such as  $\text{Sr}_2\text{Fe}_{1.5}\text{Mo}_{0.5}\text{O}_{6-\delta}$  [177].

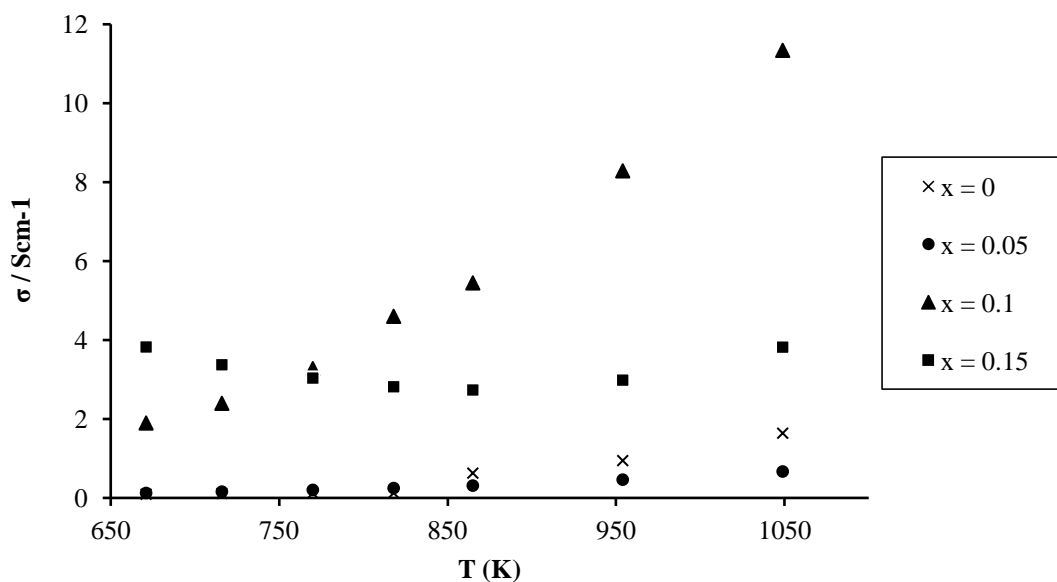


Figure 30. Plot of conductivity against temperature for the series  $SrFe_{1-x}Si_xO_{3-\delta}$  in  $5\%H_2/N_2$

Si mol %	0	5	10	15
800 °C (S cm <sup>-1</sup> )	1.6	0.7	11.3	3.8
700 °C (S cm <sup>-1</sup> )	0.9	0.5	8.3	3.0
600 °C (S cm <sup>-1</sup> )	0.6	0.3	5.4	2.7
500 °C (S cm <sup>-1</sup> )	0.1	0.2	3.3	3.0
400 °C (S cm <sup>-1</sup> )	0.1	0.1	1.9	3.8

Table 12. Conductivity data for  $SrFe_{1-x}Si_xO_{3-\delta}$  in  $5\%H_2/N_2$

In this respect, it is interesting to note that doped samples that were held at 800 °C for 30 minutes, before having conductivity measurements taken on decreasing temperature,

showed significantly higher electronic conductivities than the samples measured on increasing temperatures. This may be due either to the partial reduction of  $\text{Fe}^{3+}$  to  $\text{Fe}^{2+}$  or to the precipitation of iron metal out of the structure which could be providing additional conducting species (as seen in literature examples involving Ni and Ru), although there was no clear evidence for this by XRD [178]. Again the  $x = 0.1$  sample displayed the highest conductivity, reaching  $11.34 \text{ S cm}^{-1}$  at  $800 \text{ }^\circ\text{C}$  and displaying a large drop on decreasing the temperature. The undoped sample showed little variation in conductivity and did not display the same large drop with decreasing temperature.

Overall the lower conductivities under 5%  $\text{H}_2/\text{N}_2$  than air may hinder the use of Si-doped strontium ferrites as a stand-alone anode material; however they may function well as cermets with nickel or other metals. The increase in disordering of the oxygen vacancies upon the introduction of silicon should result in enhanced oxide ion conductivity over the undoped sample and hence further increase their suitability as anode cermet oxides.

### **5.3.3. Area Specific Resistance**

Area specific resistance studies were carried out on the series  $\text{SrFe}_{1-x}\text{Si}_x\text{O}_{3-\delta}$  in both air and 5%  $\text{H}_2/\text{N}_2$  atmospheres. As described above, a composite of the perovskite and CGO10 was deposited on dense CGO10 pellets, and fired at  $1000 \text{ }^\circ\text{C}$  for 1 hour before having electrodes attached.

### 5.3.3.1. Air Atmosphere

Si mol %	0	5	10	15
700 °C ASR ( $\Omega \text{ cm}^2$ )	1.65	1.19	0.90	1.88
800 °C ASR ( $\Omega \text{ cm}^2$ )	0.25	0.14	0.08	0.28

Table 13. ASR values for the series  $\text{SrFe}_{1-x}\text{Si}_x\text{O}_{3-\delta}$  in air

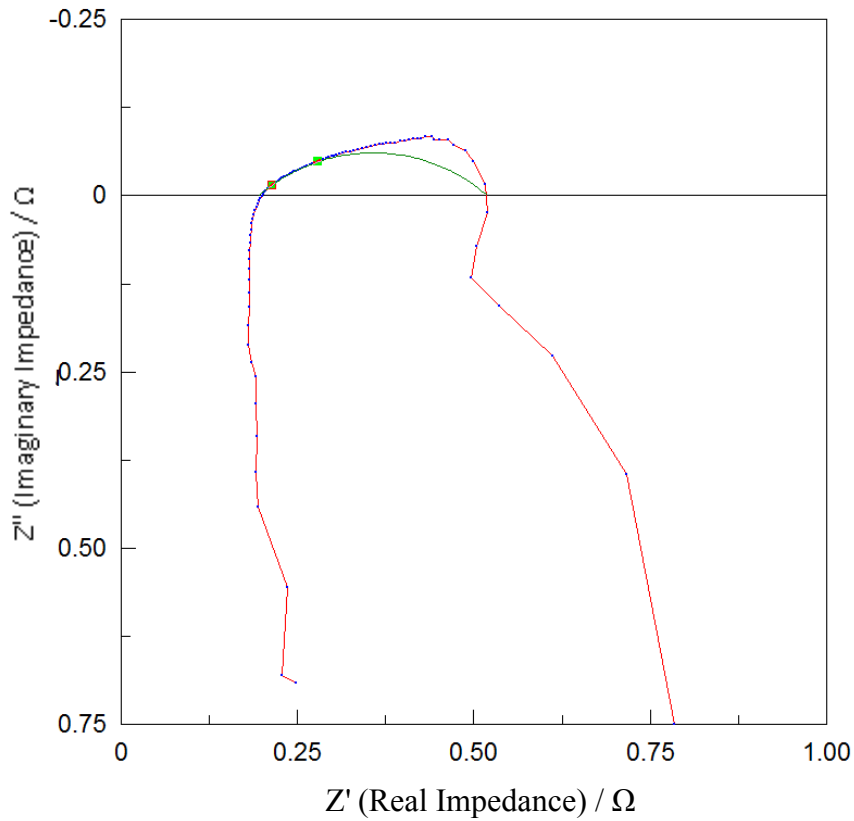


Figure 31. Nyquist plot for  $\text{SrFe}_{0.9}\text{Si}_{0.1}\text{O}_{3-\delta}$  at 800 °C in air, including fitting

Values for ASR in air can be seen in Table 13 and a Nyquist plot for the 10% Si sample at 800°C is shown in Figure 31. A considerable improvement was obtained for the 5 and

10% mol doped samples over the undoped  $\text{SrFeO}_{3-\delta}$ , with values of 0.14 and 0.08  $\Omega \text{ cm}^2$  respectively against 0.25  $\Omega \text{ cm}^2$  at 800 °C. Once again, the 15% mol doped sample displayed a drop in performance from that of both the 10% mol doped and undoped sample, with a value of 0.28  $\Omega \text{ cm}^2$  at 800 °C. This may be due to the disruption of the electron conductivity pathway or the possible presence of amorphous Si-containing impurities at this higher Si level, causing increased resistances. The loss of oxygen at higher temperatures may explain the significant improvement in ASR at elevated temperatures; loss of oxygen leads to an increase in oxide ion mobility through the increase in the concentration of oxide ion vacancies.

It should be noted that a perfect semicircle is not formed by the material, as represented on the Nyquist plot. This is due to the different resistances of the bulk material and the grain boundary, with the two semicircles representing each being difficult to distinguish. However, as both parts in combination represent the overall resistance, the intercept points still hold true.

### 5.3.3.2. 5% $\text{H}_2/\text{N}_2$ Atmosphere

Si mol %	0	5	10	15
600 °C ASR ( $\Omega \text{ cm}^2$ )	1.88	1.51	0.17	0.24

*Table 14. ASR values for the series  $\text{SrFe}_{1-x}\text{Si}_x\text{O}_{3-\delta}$  in 5% $\text{H}_2/\text{N}_2$*

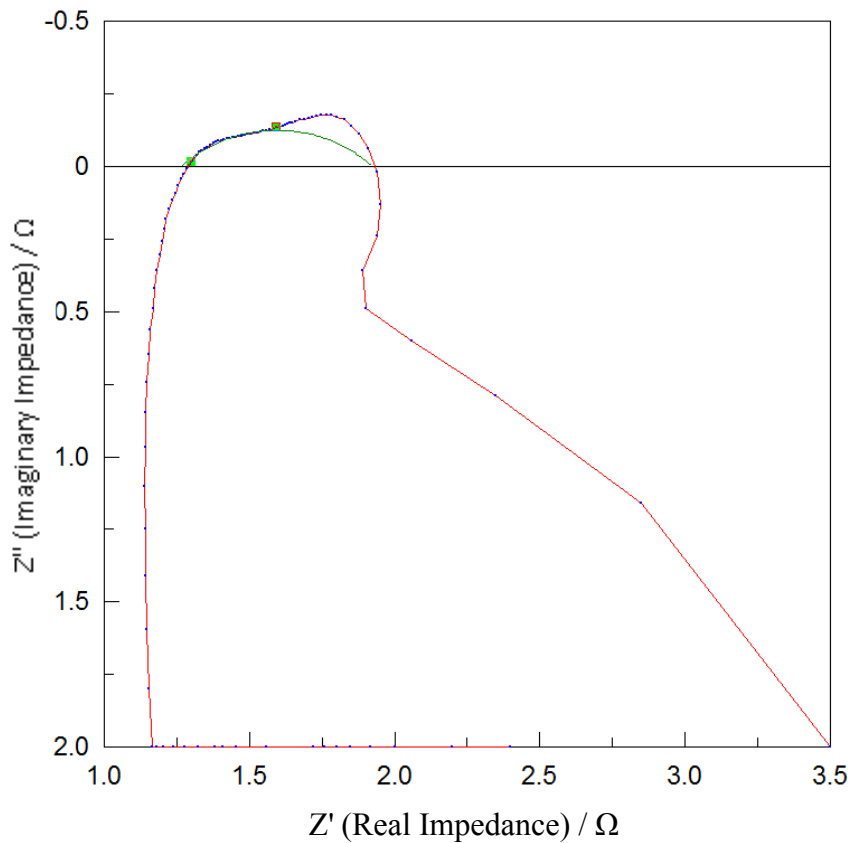


Figure 32. Nyquist plot for  $\text{SeFe}_{0.9}\text{Si}_{0.1}\text{O}_{3-\delta}$  at 600 °C in 5% $\text{H}_2/\text{N}_2$ , including fitting

Values for ASR against temperature in 5% $\text{H}_2/\text{N}_2$  can be seen in Table 14. As before, an improvement was noticed for the 5 and 10% mol doped samples over the undoped  $\text{SrFeO}_{3-\delta}$ , with values of 1.51 and 0.17  $\Omega \text{ cm}^2$  against 1.88  $\Omega \text{ cm}^2$  at 600 °C. While the 15% mol doped sample displayed a drop in performance compared to the 10% mol doped sample, but it was significantly improved compared to the 5% mol doped and undoped samples, with a value of 0.24  $\Omega \text{ cm}^2$  at 600 °C. The reduced performance of the 5% Si mol doped sample against the 15% mol doped sample may be due to the lower Si content not fully stabilising the cubic phase and on reduction, allowing the ordered  $\text{Sr}_2\text{Fe}_2\text{O}_5$  phase to partially form. The ASR performance was seen to improve at higher temperatures in air, for example the 10% mol doped sample had values of 0.90 vs 0.08  $\Omega$

cm<sup>2</sup> for 700 vs 800 °C. If this was to hold true for reducing atmospheres then the performance of the 10 and 15% mol doped materials may far surpass the air performance based on the figures obtained at 600 °C. However, since the Ce within the CGO10 electrolyte reduces above 600 °C, such higher temperature measurements in 5% H<sub>2</sub>/N<sub>2</sub> could not be performed and so further studies are warranted analysing the performance of these systems utilising a YSZ electrolyte.

Again, as can be seen in Figure 32, two separate curves contribute to the overall resistance of the sample, with the grain boundary and the bulk resistances being difficult to distinguish from one another.

#### 5.3.4. Dilatometry

Dilatometry studies were carried out on the series SrFe<sub>1-x</sub>Si<sub>x</sub>O<sub>3-δ</sub> with x = 0, 0.05 and 0.10 in air. The results are shown in Table 15 and Figure 33, Figure 34 and Figure 35.

Si mol %	0	5	10
TEC in temperature band 20 - 480 °C (x 10 <sup>-6</sup> /K)	19.3	18.6	14.8
TEC in temperature band 480 - 1000 °C (x 10 <sup>-6</sup> /K)	37.4	34.5	32.3

Table 15. TEC data for the series SrFe<sub>1-x</sub>Si<sub>x</sub>O<sub>3-δ</sub>

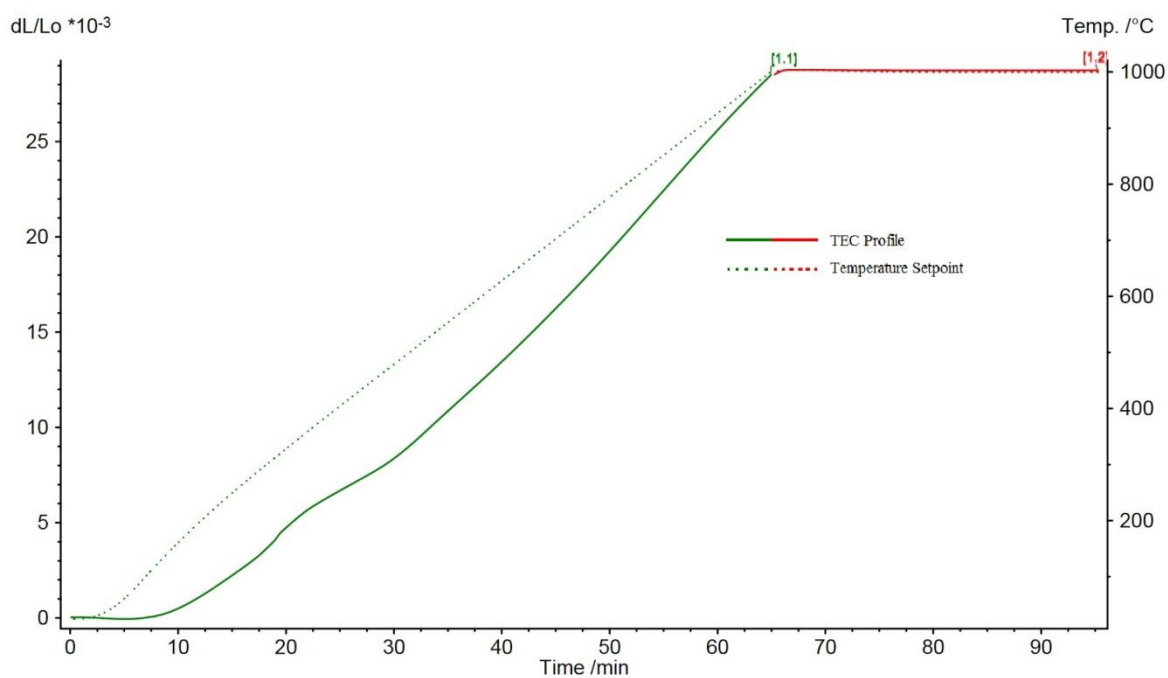


Figure 33. Dilatometry data for  $\text{SrFeO}_{3-\delta}$  from 20 - 1000 °C at 15 °C min<sup>-1</sup> in air. Solid line is TEC profile, dashed line is temperature profile

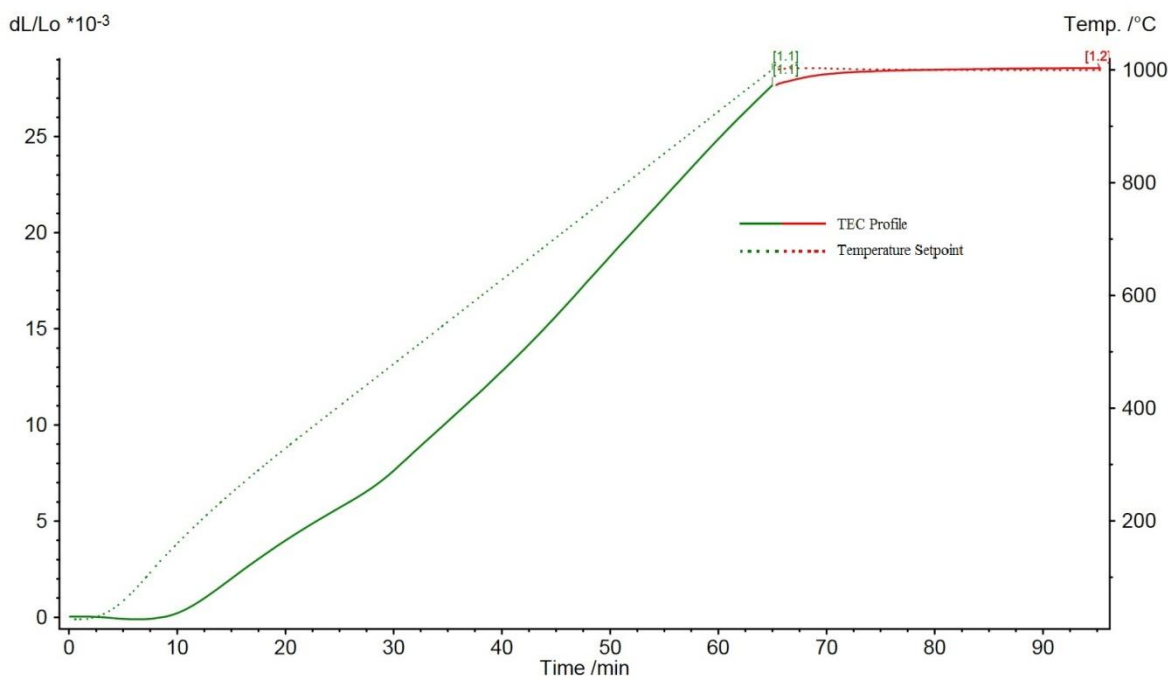


Figure 34. Dilatometry data for  $\text{SrFe}_{0.95}\text{Si}_{0.05}\text{O}_{3-\delta}$  from 20 - 1000 °C at 15 °C min<sup>-1</sup> in air. Solid line is TEC profile, dashed line is temperature profile

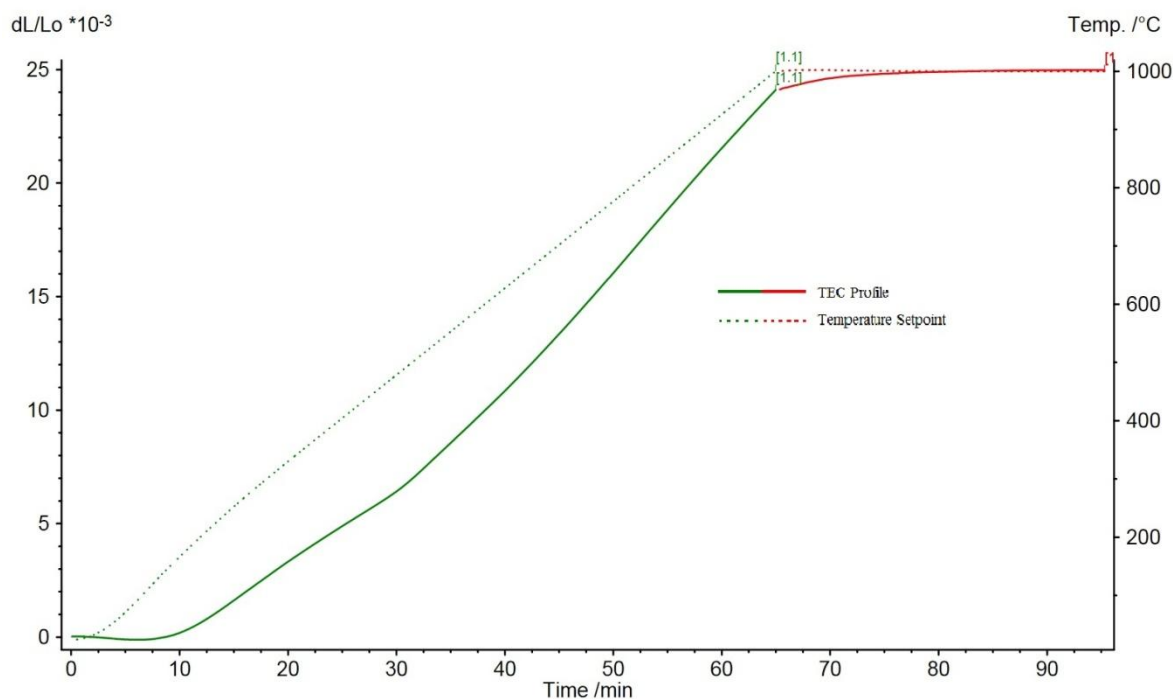


Figure 35. Dilatometry data for  $\text{SrFe}_{0.9}\text{Si}_{0.1}\text{O}_{3-\delta}$  from 20 - 1000 °C at  $15\text{ }^\circ\text{C min}^{-1}$  in air. Solid line is TEC profile, dashed line is temperature profile

As expected, a reduction in the thermal expansion coefficient (TEC) is seen in the doped sample versus the undoped; this has previously been reported to occur for other doped  $\text{SrFeO}_{3-\delta}$  series, such as  $\text{SrFe}_{1-x}\text{M}_x\text{O}_{3-\delta}$  ( $\text{M} = \text{Ga}, \text{Al}, \text{Ti}$ ) and other related materials [175, 179–181]. The TECs recorded here are in line with literature values for these other doped strontium ferrite series. Both the doped and undoped dilatometric curves display a non-linear behaviour above approximately 480 °C, which may be attributed to the loss of oxygen and subsequent reduction of  $\text{Fe}^{4+}$  to the larger  $\text{Fe}^{3+}$  causing an increase in the TEC. The reduction in TEC on Si doping can then be related to the lower average Fe oxidation state, as on heating the level of oxygen loss and hence reduction is lower. The observed reduction in TEC for the 10% Si doped sample over the undoped sample from  $19.3$  to  $14.8 \times 10^{-6} / \text{K}$  below 480 °C, and from  $37.4$  to  $32.3 \times 10^{-6} / \text{K}$  above 480 °C,

would assist in making  $\text{SrFe}_{0.9}\text{Si}_{0.1}\text{O}_{3-\delta}$  a more suitable SOFC material as it has a closer match to the TEC of existing SOFC materials. However the higher temperature TECs are still probably too high, limiting  $\text{SrFe}_{0.9}\text{Si}_{0.1}\text{O}_{3-\delta}$  to lower temperature use. Alternatively, by utilising a composite with the electrolyte material the difference in TEC values could be bridged for use at higher temperatures. Overall, the data suggests that intermediate temperature operation in the region of 500 - 600 °C would be a suitable use for the 10% Si material alone as it would take maximum advantage of the lower TEC while still being at temperatures high enough to allow internal reforming of hydrocarbon fuels.

Future work focussing on detailing the precise temperature of the loss of oxygen would be of interest. This could be achieved through having a slower rate of heating between 450 - 500 °C, for example, which would give much more accurate information as to when the loss occurs, allowing more details about the material to be documented.

### **5.3.5. Fuel Cell Testing**

A symmetrical pellet cell [79] of  $\text{SrFe}_{0.9}\text{Si}_{0.1}\text{O}_{3-\delta}$  was prepared and run as per Chapter 3, on pellets of electrolyte material formed using a 13mm die set. The internal diameter of the firing tube that the pellets were cemented onto was 12mm, giving an active area of approximately 1.1 cm<sup>2</sup>. The test setup can be seen in Figure 11. The initial results appeared promising for novel materials, with little gas leaking or short circuiting of the cell evident and OCVs in the region of 0.9 V. Unfortunately on all cell tests the OCV did not translate to a reasonable cell performance, with the voltage dropping rapidly when attempting to draw a current from the cell, and also the OCVs dropping off with 30

minutes, down to less than 100 mV. This behaviour was very similar to the cells fabricated in Chapter 4. Examples of cell voltages obtained from attempts to draw power from the cell can be seen in Figure 36.

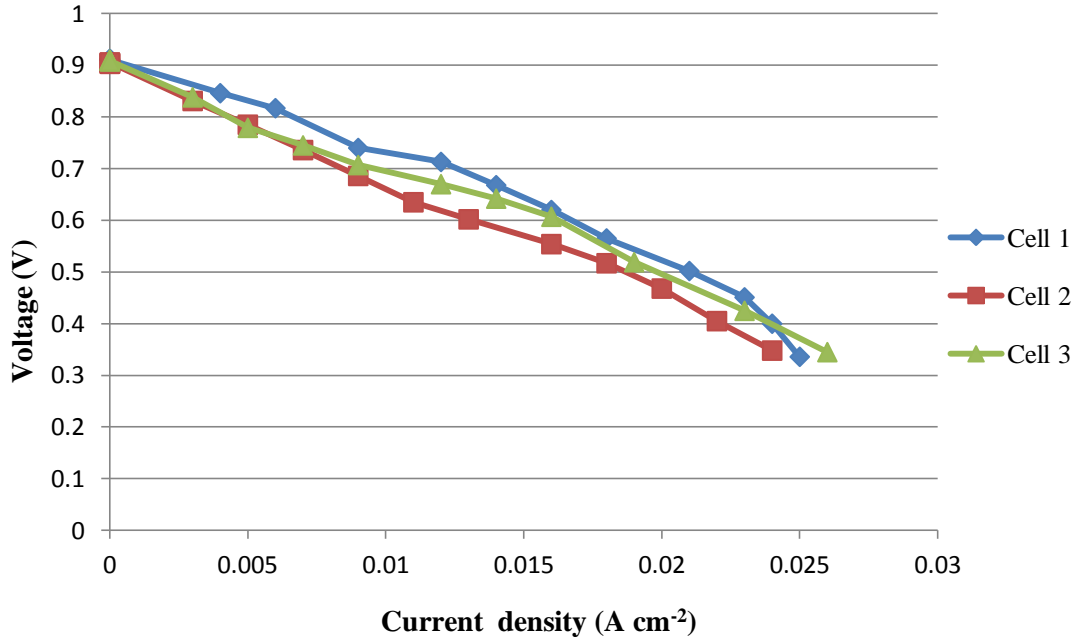


Figure 36. Voltages and currents for symmetrical pellet cells of  $\text{SrFe}_{0.9}\text{Si}_{0.1}\text{O}_{3-\delta}$  on YSZ at  $800^\circ\text{C}$  moving from OCV to 0.85 V voltage demand

The testing profile for the results seen in Figure 36 involved running the cell at OCV before attempting to draw a voltage of 0.85 V. Data were logged at 5 Hz. The settings used were chosen due to the lower OCVs displayed by the cells. This was speculated to be due to the cells being electrolyte-supported, causing higher ohmic resistances than cells with thinner electrolyte layers. Again, on attempting to draw power from the cell, the voltage falls below the set-point without significant current being produced. However, as the cells are electrolyte supported, questions over cells short-circuiting

should be alleviated, and achieving OCVs over 0.9 V also indicates little gas crossover. Further work is needed to optimise the cell production to obtain improved, repeatable performance, as per Chapter 4.

## 5.4. Conclusions

In this work it has been shown that Si can be successfully incorporated into the perovskite structure. The solubility limit for  $\text{SrFe}_{1-x}\text{Si}_x\text{O}_{3-\delta}$  was found to be  $x = 0.15$ ; above this level of Si, impurities were detected. The 5% mol Si doped sample did not fully stabilise the cubic phase in a reducing atmosphere. The presence of tetrahedral silicate oxyanions has therefore been shown to assist in stabilising oxygen vacancy disorder in  $\text{SrFeO}_{3-\delta}$  at higher temperatures, which has a positive influence on the electrochemical performance of the series leading to a lowering of area specific resistance. In addition, the thermal expansion coefficient for the doped samples under 500 °C was closer to that of many standard SOFC materials, possibly facilitating easier incorporation, although at temperatures significantly above this it was still too high with regards to conventional fuel cell electrolytes.

*Work within this Chapter was carried out in conjunction with Dr Jose Porras and has been published in the Journal of Materials Chemistry A, Volume 3, Issue 38, Pages 11834 - 11841, 2013.*

## **Chapter 6. Synthesis and characterisation of V doped**

### **Sr<sub>0.8</sub>Ti<sub>0.6</sub>Nb<sub>0.4</sub>O<sub>3-δ</sub> for SOFC Applications**

#### **6.1. Introduction**

Replacing elements within known structures with small quantities of other elements is a standard approach for altering or enhancing material properties. Within the family of perovskite materials, A-site deficient compounds are one subcategory of materials, many of which have gained attention in part due to promising thermal stability, electrical characteristics and chemical compatibility with other materials potentially used within SOFC systems. Examples of A-site deficient perovskite materials include (La<sub>0.75</sub>Sr<sub>0.25</sub>)<sub>0.95</sub>Cr<sub>0.5</sub>Mn<sub>0.5</sub>O<sub>3-δ</sub> (LSCM) (Sr<sub>1-x</sub>La<sub>x</sub>)<sub>1-y</sub>Ti<sub>1-z</sub>O<sub>3</sub> and La<sub>0.4</sub>Sr<sub>0.4</sub>Ga<sub>x</sub>Ti<sub>1-x</sub>O<sub>3-x/2</sub> amongst others [39, 42, 44, 182, 183]. Synthesising A-site deficient perovskite materials can be achieved very simply, as in the case of LSCM, by using non-stoichiometric quantities of reactants. However, it is also possible to form deficiencies though doping with one or more cations of a different charge to the cation they are replacing. Such work often centres on charge balancing the crystal structure by doping on both the A- and B-sites. Doping with species of different charge in order to form A-site deficient materials has been well documented in the past with series such as the perovskites Sr<sub>1-x/2</sub>Ti<sub>1-x</sub>Nb<sub>x</sub>O<sub>3-δ</sub>, Sr<sub>0.86</sub>Y<sub>0.08</sub>TiO<sub>3-δ</sub> and others [35, 38, 135, 146, 184, 185]. The presence of A-site vacancies can also in turn promote oxygen vacancies which improve oxide transportation and so can assist in the performance of MIEC materials, such as the double perovskite material series La<sub>2-x</sub>NiTiO<sub>6-δ</sub> [186].

In addition, the related tungsten bronze phase  $\text{Sr}_{0.6}\text{Ti}_{0.2}\text{Nb}_{0.8}\text{O}_{3-\delta}$  and its variants has been investigated after it was identified as an impurity in the perovskite system  $\text{Sr}_{1-x/2}\text{Ti}_{1-x}\text{Nb}_x\text{O}_{3-\delta}$  if  $x > 0.4$  [45]. These and other related tungsten bronze materials displayed promising conductivities but did show minor chemical compatibility issues with commonly-utilised electrolyte material YSZ at elevated temperatures [47].

However, both  $\text{Sr}_{1-x/2}\text{Ti}_{1-x}\text{Nb}_x\text{O}_{3-\delta}$  and  $\text{Sr}_{0.6}\text{Ti}_{0.2}\text{Nb}_{0.8}\text{O}_{3-\delta}$  display Warburg type behaviour when studied using AC impedance, implying slow oxygen transport due to a diffusion limited process [47]. Investigation into this and other series have confirmed that this diffusion limited process is also at fault for the slow reoxidisation of reduced samples by studying porous samples which do not display the same behaviour [187]. While oxygen diffusion-limited processes were shown to be possible to avoid by creating a much more porous sample [188] it still will impede the performance within a SOFC by reducing the available triple phase boundary as slow oxygen ion mobility impedes the overall electrochemical reactions. The tungsten bronze-type series displayed improved reoxidisation kinetics and hence inferred greater oxide ion conduction than the perovskite series; however, the level was still comparatively low for SOFC electrode materials. There is consequently a need to investigate strategies to improve the oxide ion conductivity.

Doping with vanadium has been shown to increase the catalytic activity towards steam reforming within perovskite anode materials while reducing carbon deposition [189] and is more stable in its lower oxidation states than niobium which may assist in increasing the performance of a material doped with vanadium on the niobium site in a reducing

atmosphere [37, 190]. In particular, lowering the oxidation state of vanadium upon reduction would promote oxygen loss and may improve oxide ion conductivity and redox properties at SOFC operating temperatures. For these reasons, V doping into  $\text{Sr}_{0.8}\text{Ti}_{0.6}\text{Nb}_{0.4}\text{O}_{3-\delta}$  was investigated, forming  $\text{Sr}_{0.8}\text{Ti}_{0.6}\text{Nb}_{0.4-x}\text{V}_x\text{O}_{3-\delta}$ , as this particular material was shown to be the limit of niobium doping in  $\text{Sr}_{1-x/2}\text{Ti}_{1-x}\text{Nb}_x\text{O}_{3-\delta}$  while retaining the perovskite structure, with the tungsten bronze phase present as an impurity at higher levels. This large incorporation of Nb within the perovskite unit cell allows for the greatest range in V doping and so the greatest opportunity to study the effects upon the material characteristics. During the course of these vanadium doping studies, it was shown that the unit cell was also able to accommodate a greater proportion of vanadium than niobium, with phase pure  $\text{Sr}_{0.75}\text{Ti}_{0.5}\text{V}_{0.5}\text{O}_{3-\delta}$  being successfully synthesised and analysed. In addition, limited synthesis and analysis of the tungsten bronze series  $\text{Sr}_{0.6}\text{Ti}_{0.2}\text{Nb}_{0.8-x}\text{V}_x\text{O}_3$  was carried out in order to determine the effect of doping vanadium into this system.

## 6.2. Experimental

Stoichiometric quantities of high purity powders of  $\text{SrCO}_3$ ,  $\text{Nb}_2\text{O}_3$  and  $\text{V}_2\text{O}_5$  were ground intimately before heating to 1100 °C for 12 hours. Samples were then ball milled (Fritsch Pulverisette 7 Planetary Mill for 1 hour at 350 rpm) and heated to 1300 - 1400 °C for a further 12 hours. Powder X-ray diffraction (Bruker D8 autosampler diffractometer using  $\text{Cu K}_{\alpha 1}$  radiation) was carried out to ensure phase purity and calculate cell parameters. Unit cell refinement was carried out using GSAS and EXPGUI [123, 124].

For 4-probe DC conductivity measurements, powders were ball milled (Fritsch Pulverisette 7 Planetary Mill for 1 hour at 350 rpm with 2 milling beads) before being pressed as pellets of 13mm diameter and sintering at 1350 °C for 12 hours. Platinum electrodes were then attached using platinum paste (Metalor) and fired at 800 °C for 1 hour to bond the Pt. 4 probe DC conductivity measurements were then taken in H<sub>2</sub>/N<sub>2</sub> ascending from 300 °C to 800 °C, before reducing at 930 °C for 1 hour and then taking measurements down from 800 °C to 300 °C.

For ASR measurements, ink suspensions were prepared containing 1:1 wt% of electrolyte and electrode materials with 20 %wt Decoflux (Zschimmer and Schwarz) to act as a dispersant and binder. Samples were then ball milled (Fritsch Pulverisette 7 Planetary Mill for 1 hour at 350 rpm with 2 milling beads) and coated onto dense Zr<sub>0.85</sub>Y<sub>0.15</sub>O<sub>1.925</sub> (YSZ8, UCM Advanced Ceramics) pellets (sintered at 1500 °C for 12 hours) to form a mirrored cell and then fired at 1000 °C for 1 hour. Pt paste was then applied to both sides to act as a current collector and bonded at 800 °C for 1 hour. ASR values were obtained in both cathodic (air) and anodic (5% H<sub>2</sub>/N<sub>2</sub>) conditions at temperatures up to and 800 °C. Impedance data were collected between 5 Hz - 13 MHz at open circuit voltage (OCV) with an A.C. signal amplitude of 100 mV (HP 4912A Frequency Analyser). The spectra was plotted using ZView software to give an estimate of the resistance and capacitance of the different cell component materials [127].

Samples prepared for dilatometry measurements were ball milled as powders (Fritsch Pulverisette 7 Planetary Mill for 1 hour at 350 rpm with 2 milling beads) before being pressed into thick pellets of 10 mm diameter and approximately 10 mm length. These

were sintered at 1350 °C for 12 hours and then polished to form smooth, flat ends. Dilatometry data were obtained using a Netzsch 409C dilatometer, running a profile from 25 °C to 1000 °C at 15 °C min<sup>-1</sup> in an air atmosphere.

## **6.3. Results and Discussion**

### **6.3.1. Synthesis and Structure Determination**

The unit cell for Sr<sub>0.8</sub>Ti<sub>0.6</sub>Nb<sub>0.4</sub>O<sub>3-δ</sub> has previously been shown to be cubic and all data obtained here confirms this [146]. X-ray diffraction data showed that it was possible to completely replace Nb<sup>5+</sup> with V<sup>5+</sup> within the perovskite structure for Sr<sub>0.8</sub>Ti<sub>0.6</sub>Nb<sub>0.4-x</sub>V<sub>x</sub>O<sub>3-δ</sub>, and phase pure samples were prepared for values of x between 0 and 0.4 at 0.05 intervals. In addition, the V level and A-site deficiency was further increased by increasing the vanadium doping to give Sr<sub>0.75</sub>Ti<sub>0.5</sub>V<sub>0.5</sub>O<sub>3-δ</sub> without impurities being detected. Figure 38, Figure 39, Figure 40 and Figure 41 show a selection of XRD patterns for this series. These are clean, with well-defined peaks, showing no impurities present.

x	a (Å)	V (Å <sup>3</sup> )
0	3.9298(1)	60.690(1)
0.05	3.9237(1)	60.406(1)
0.1	3.9192(1)	60.200(1)
0.15	3.9122(1)	59.876(1)
0.2	3.9110(1)	59.820(1)
0.25	3.9090(1)	59.732(1)
0.35	3.9019(1)	59.407(1)
0.4	3.9008(1)	59.357(1)

Table 16. Unit cell size and cell volume for  $Sr_{0.8}Ti_{0.6}Nb_{0.4-x}V_xO_{3-\delta}$

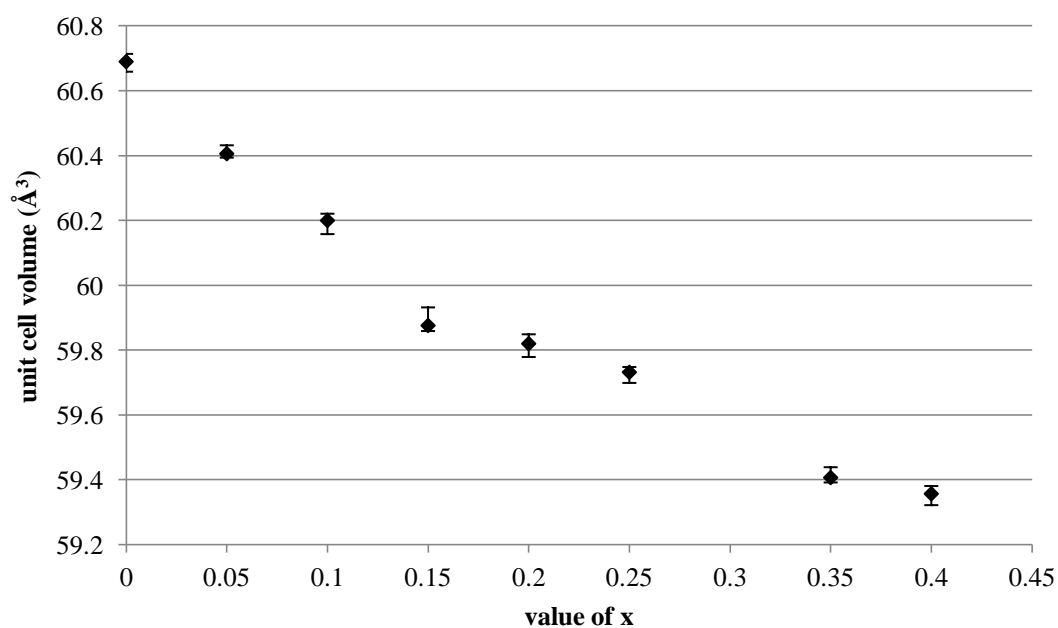


Figure 37. Graph showing unit cell volume (Å<sup>3</sup>) for  $Sr_{0.8}Ti_{0.6}Nb_{0.4-x}V_xO_{3-\delta}$  against V content

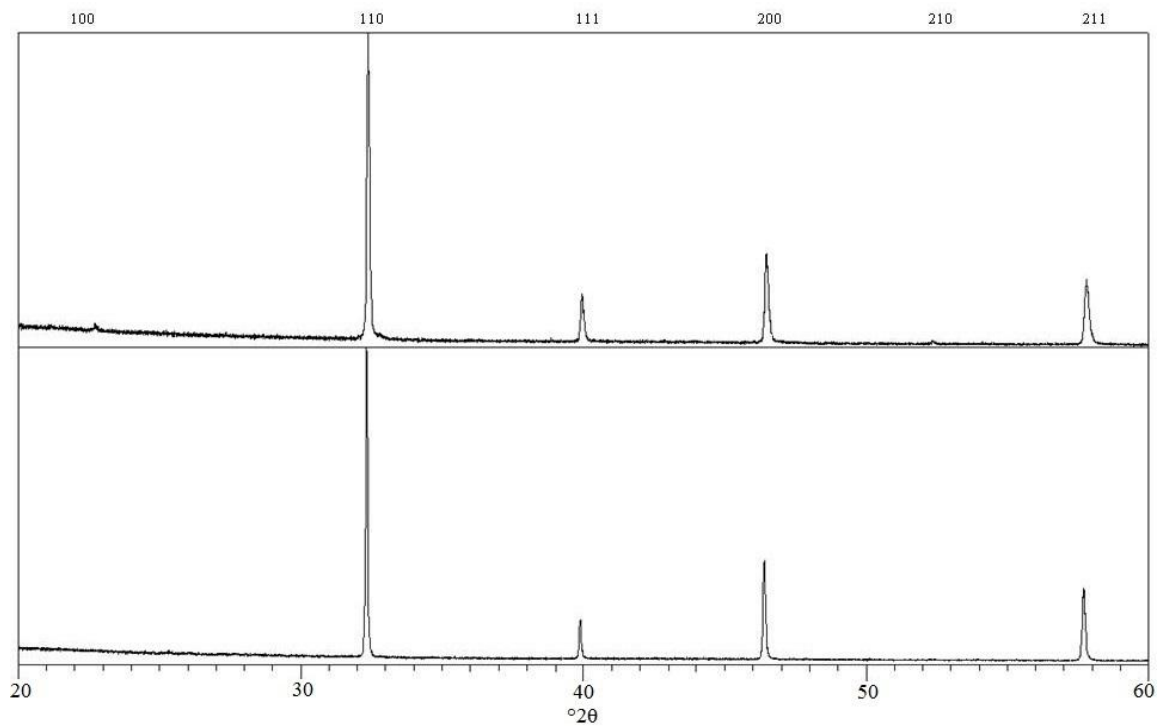


Figure 38. XRD pattern for  $Sr_{0.8}Ti_{0.6}Nb_{0.2}V_{0.2}O_{3-\delta}$  in air (bottom) and annealed in 5% $H_2/N_2$  at 600 °C for 24 hours (top)

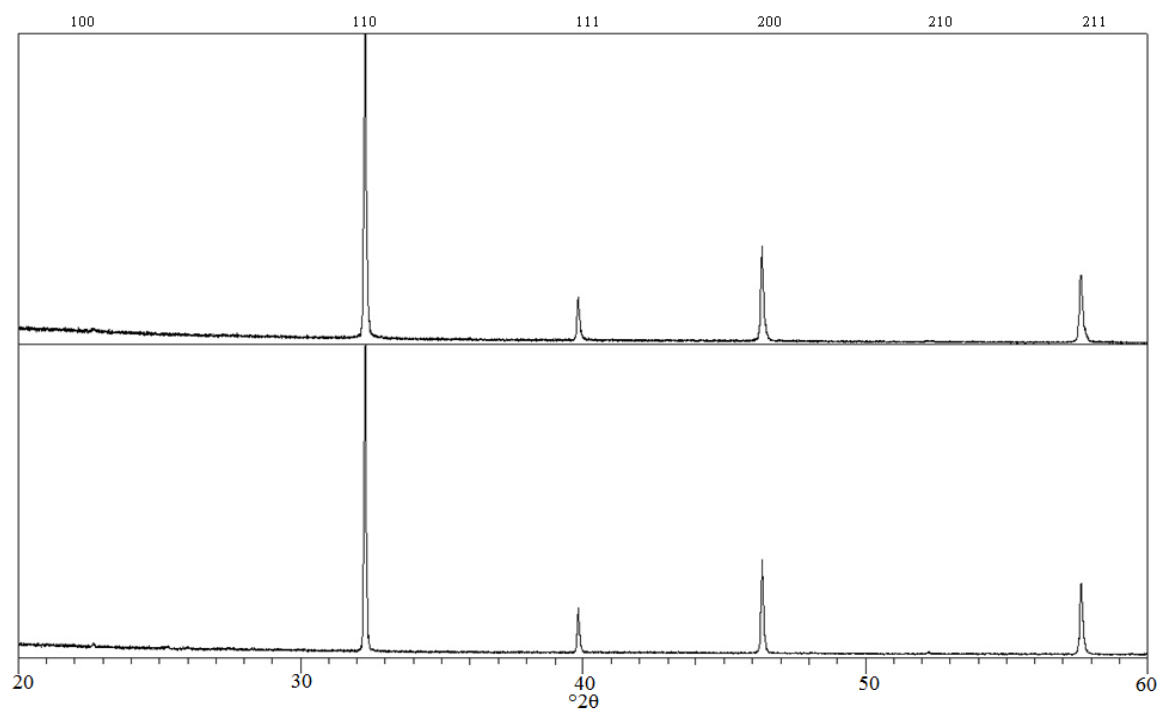


Figure 39. XRD pattern for  $Sr_{0.8}Ti_{0.6}Nb_{0.15}V_{0.25}O_{3-\delta}$  in air (bottom) and annealed in 5% $H_2/N_2$  at 600 °C for 24 hours (top)

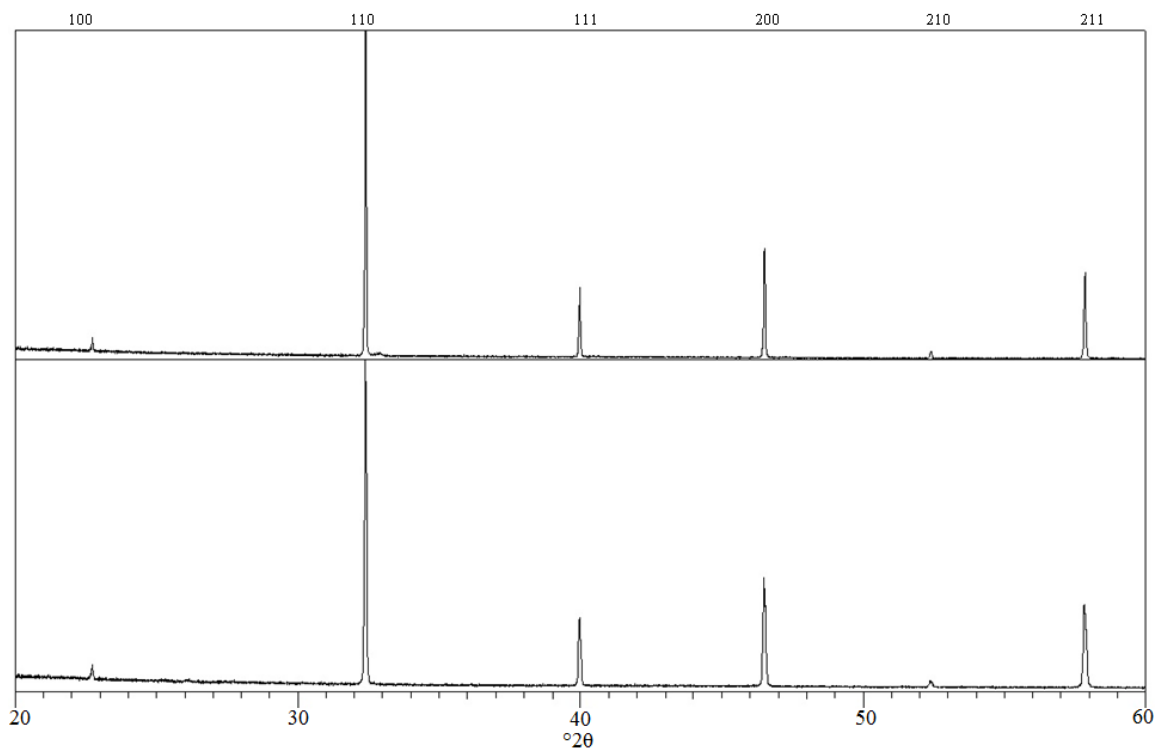


Figure 40. XRD pattern for  $Sr_{0.8}Ti_{0.6}V_{0.4}O_{3-\delta}$  in air (bottom) and annealed in 5%  $H_2/N_2$  at 600 °C for 24 hours (top)

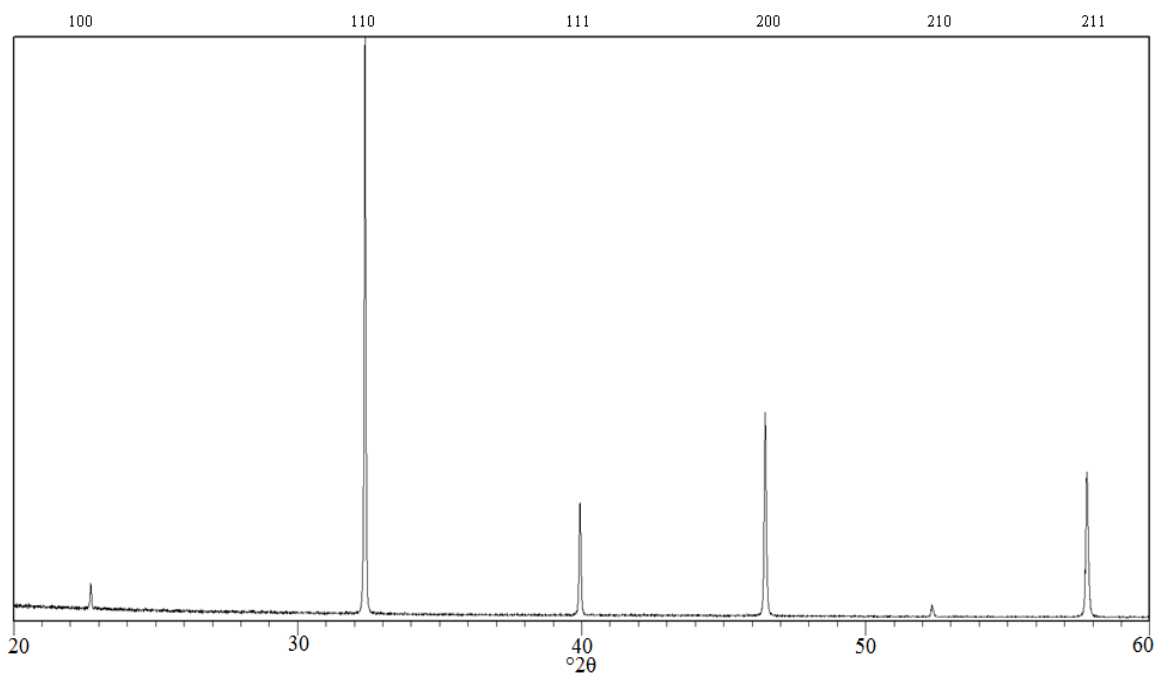


Figure 41. XRD pattern for  $Sr_{0.75}Ti_{0.5}V_{0.5}O_{3-\delta}$  in air showing single phase purity

Cell parameters for the unreduced series are shown in Table 16. As niobium is replaced by vanadium the unit cell size decreases. This is fully expected as the  $V^{5+}$  cation is smaller than  $Nb^{5+}$  (0.54 versus 0.64Å) which would predict a reduction in unit cell size on V incorporation, and even if vanadium is reduced down to  $V^{4+}$  (0.58Å) the unit cell is still expected to contract [174]. The one anomalous point at  $x = 0.3$  may be caused by very small levels of impurities being present in this particular phase.

The sample  $Sr_{0.75}Ti_{0.5}V_{0.5}O_{3-\delta}$  showed an increased unit cell size over the  $Sr_{0.8}Ti_{0.6}V_{0.4}O_{3-\delta}$  sample, with values of  $a = 3.9071\text{Å}$  and  $V = 59.644\text{Å}^3$ . This increase was not expected as the  $V^{5+}$  cation is smaller than the  $Ti^{4+}$  it is replacing (0.54 versus 0.605Å). In addition, the increase in A-site vacancies necessitated by the need for charge balancing the replacement of  $Ti^{4+}$  with  $V^{5+}$  might be expected to bring about a further reduction in unit cell size. Further studies are required to investigate the origin of this increase, but it may relate to the influence of some partial A-site vacancy ordering as a result of the high levels of vacancies.

A selection of phase pure materials from the series was reduced at 930 °C for 24 hours in an atmosphere of 5% $H_2/N_2$ . The unit cell size and volumes calculated for several samples can be seen in Table 17 and Figure 42, and Figure 38, Figure 39, Figure 40 and Figure 41 display XRD patterns for several reduced species against their unreduced counterparts.

x	a (Å)	V (Å <sup>3</sup> )
0.15	3.9030(1)	59.456(1)
0.2	3.9050(1)	59.547(1)
0.25	3.9071(1)	59.644(1)
0.4	3.9018(1)	59.401(1)

Table 17. Unit cell size and cell volume for  $Sr_{0.8}Ti_{0.6}Nb_{0.4-x}V_xO_{3-\delta}$  reduced at 930 °C in 5% $H_2/N_2$

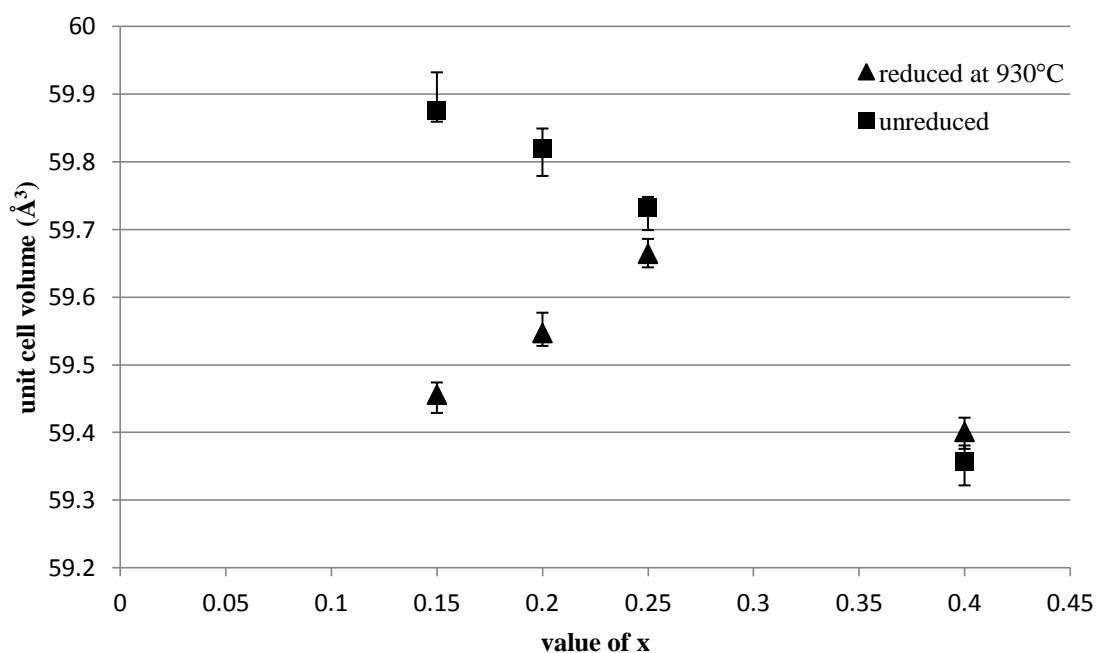


Figure 42. Graph showing unit cell volume (Å<sup>3</sup>) for  $Sr_{0.8}Ti_{0.6}Nb_{0.4-x}V_xO_{3-\delta}$  (unreduced and reduced at 930 °C) against V content

For the samples  $x = 0.15, 0.2$  and  $0.25$ , the unit cell size increases with increasing vanadium content which can be explained by the reduction of some of the  $V^{5+}$  counteracting the size difference between  $Nb^{5+}$  and  $V^{5+}$  ( $0.64\text{Å}$  vs  $0.54\text{Å}$ ), with

vanadium reducing more readily than niobium. However, when vanadium fully replaces niobium it can be seen that the unit cell size decreases again. It should be noted that the only sample in which the unit cell volume of the reduced sample is larger than that of the unreduced sample is  $x = 0.4$ . This runs contrary to expectations as it would be anticipated that the reduction of  $\text{Nb}^{5+}/\text{V}^{5+}$  to  $\text{Nb}^{4+}/\text{V}^{4+}$  would lead to an expansion in unit cell due to the increase in cationic radius, and directly contradicts previous findings on the series  $\text{Sr}_{1-x/2}\text{Ti}_{1-x}\text{Nb}_x\text{O}_{3-\delta}$  showing an increase in unit cell size on reduction [35, 146, 187]. It may be that due to the larger reduction, the larger level of oxide ion vacancies (which contribute to a cell size reduction) may balance the effect of the larger  $\text{V}^{4+}$  cation size. In addition, it should be noted that on closer inspection, all of the spectra for the reduced samples contain a very small secondary shoulder peak which can be seen to be forming at a slightly higher  $2\theta$  value than the large peak at  $\sim 32^\circ$  which is not present on the undoped sample, possibly indicating the partial breakdown of the perovskite structure or some degree of oxide ion vacancies ordering, for example forming tetrahedral clusters around the vanadium cation. Unfortunately this peak is too small to gather any further detailed information.

### 6.3.2. 4-Probe DC Conductivity

4 probe DC conductivity measurements were carried out on the series  $\text{Sr}_{0.8}\text{Ti}_{0.6}\text{Nb}_{0.4-x}\text{V}_x\text{O}_{3-\delta}$  ( $\leq x \leq 0.4$ ), with the focus on conductivities in a reducing atmosphere. To achieve this, samples were reduced at  $930^\circ\text{C}$  for 30 minutes before analysis. In addition, a sample of  $\text{Sr}_{0.75}\text{Ti}_{0.5}\text{V}_{0.5}\text{O}_{3-\delta}$  was also analysed. Figure 43 and Table 18 display conductivities of samples for a range of temperatures. As anticipated, the unreduced

samples displayed very low conductivities in air. This trend was also shown at lower temperatures temperature in 5% $H_2/N_2$ .  $Sr_{0.8}Ti_{0.6}Nb_{0.2}V_{0.2}O_{3-\delta}$  was shown to have the highest consistent conductivities of the group with values of 2.34 and 5.63  $S\ cm^{-1}$  at 800  $^{\circ}C$  and 300  $^{\circ}C$  respectively.

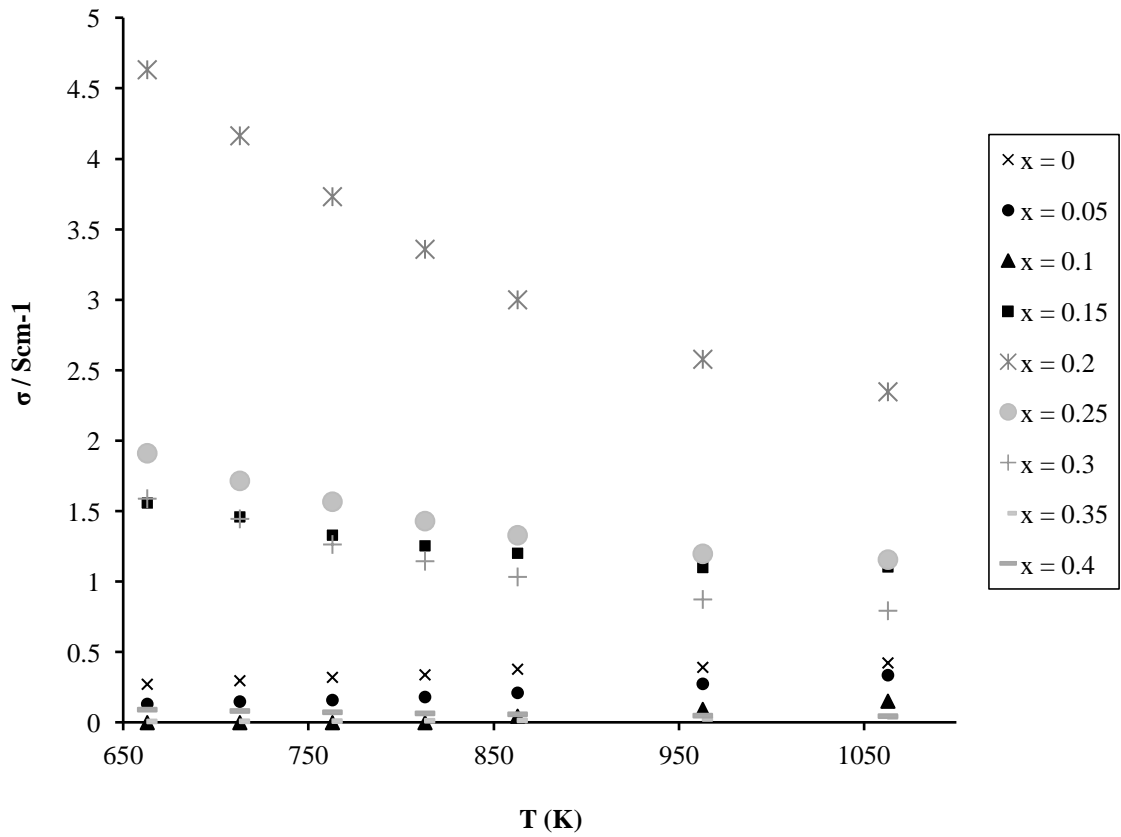


Figure 43. Plot of conductivity against temperature for the series  $Sr_{0.8}Ti_{0.6}Nb_{0.4-x}V_xO_{3-\delta}$  in 5% $H_2/N_2$

x	0	0.05	0.10	0.15	0.20	0.25	0.30	0.35	0.40
800 °C (S cm <sup>-1</sup> )	0.46	0.34	0.15	1.10	2.34	1.16	0.79	0.04	0.04
700 °C (S cm <sup>-1</sup> )	0.42	0.28	0.09	1.10	2.58	1.20	0.87	0.02	0.05
600 °C (S cm <sup>-1</sup> )	0.33	0.21	0.05	1.20	3.00	1.33	1.03	0.02	0.06
300 °C (S cm <sup>-1</sup> )	0.18	0.12	0.00	1.79	5.63	2.61	2.16	0.01	0.11

*Table 18. 4-probe DC conductivity data for the series  $Sr_{0.8}Ti_{0.6}Nb_{0.4-x}V_xO_{3-\delta}$  in 5% $H_2/N_2$  post reduction at 930 °C*

Upon increasing proportion of vanadium, the general conductivity behaviour moved from that of a semiconductor-like material to that of a metal-like material, albeit showing low electronic conductivity. This was indicated by the tendency for metallic materials to display a reduction in conductivity with increasing temperature and for the reverse to hold true for semiconductors. This behaviour may be attributed to the reduction of  $V^{5+}$  to  $V^{4+}$ . However, above  $x = 0.3$  the conductivity drops to a very low level, with the  $x = 0.35$  and 0.4 samples along with the  $Sr_{0.75}Ti_{0.5}V_{0.5}O_{3-\delta}$  sample displaying values at least one order of magnitude lower than the 0.2 sample.

### **6.3.3. Area Specific Resistance**

Since  $Sr_{0.8}Ti_{0.6}Nb_{0.2}V_{0.2}O_{3-\delta}$  was shown to have the highest conductivity in reducing conditions, a sample was investigated further as an anode material. A layer of  $Sr_{0.8}Ti_{0.6}Nb_{0.2}V_{0.2}O_{3-\delta}$  was coated onto a dense pellet of 8%mol YSZ. Values for ASR

were recorded at 700 and 800 °C in both air and 5% $H_2/N_2$ , with the latter being recorded post reduction at 930 °C. The results are shown in Table 19 and Nyquist plots for samples analysed at 800°C in both air and 5%  $H_2/N_2$  are in Figure 44 and Figure 45.

	5% $H_2/N_2$	Air
800 °C ( $\Omega\text{ cm}^2$ )	1.20	16.16
700 °C ( $\Omega\text{ cm}^2$ )	2.93	60.23

*Table 19. ASR data for the material  $Sr_{0.8}Ti_{0.6}Nb_{0.2}V_{0.2}O_{3-\delta}$  in both air and 5% $H_2/N_2$*

As expected, the performance of the material in air is far worse than that in 5% $H_2/N_2$ ; however, neither of the conditions produced particularly favourable results with respect to conventional anode materials, with the value of 1.2  $\Omega\text{ cm}^2$  being about an order of magnitude higher than a Ni/YSZ composite. As it can be seen, the drop in performance at lower temperatures is much more pronounced in the air samples.

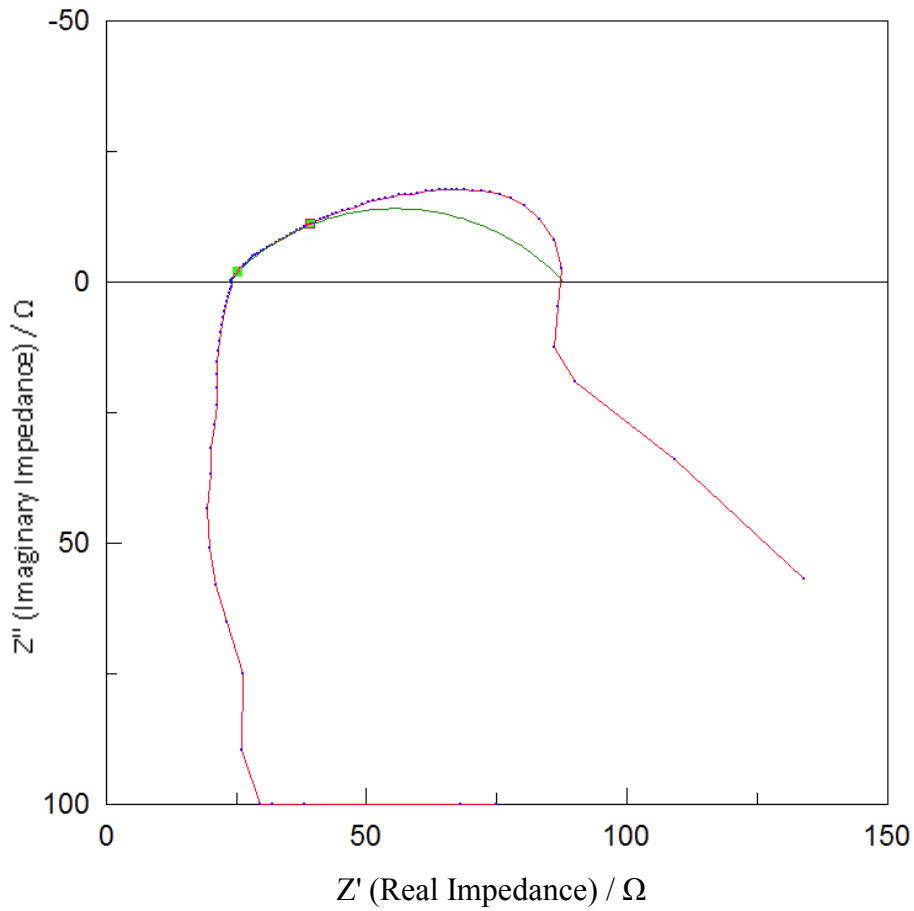


Figure 44. ASR Nyquist plot for  $Sr_{0.8}Ti_{0.6}Nb_{0.2}V_{0.2}O_{3-\delta}$  at 800 °C in air, including fitting

As in Figure 31 and Figure 32 in Chapter 5, the bulk and grain boundary resistances can both be seen contributing to the overall resistance. However, it is interesting to note that the grain boundary resistance appears more pronounced in the sample analysed under reducing conditions, suggesting that either the effect of grain boundary resistance is increased on reduction or that the bulk resistance is decreased by a larger margin under reducing conditions.

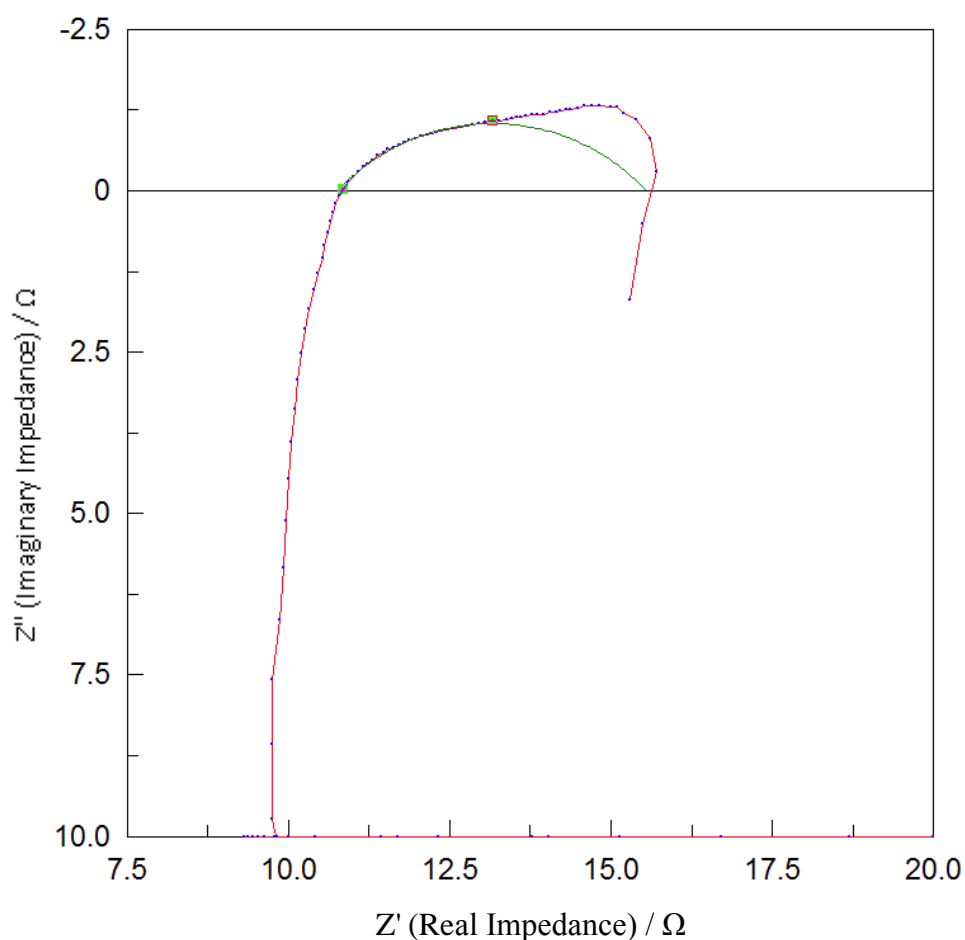


Figure 45. ASR Nyquist plot for  $Sr_{0.8}Ti_{0.6}Nb_{0.2}V_{0.2}O_{3-\delta}$  at 800 °C in 5% $H_2/N_2$ , including fitting

#### 6.3.4. Reoxidation Studies

Samples of  $Sr_{0.8}Ti_{0.6}Nb_{0.4-x}V_xO_{3-\delta}$  as prepared for 4-probe DC conductivity were reduced at 930 °C for 30 minutes before being held at 800 °C. The gas supply was then isolated and the furnace chamber vented to the atmosphere to allow air inside. The conductivity of samples was then measured over a period of up to 25 minutes to ascertain the reoxidisation of the samples, as all samples showed very low conductivity before

reduction. This study was carried out to determine the ability of the sample to reoxidise, giving an indication of the ability of oxygen and oxide ions to diffuse through the sample. If reoxidisation occurs slowly, as with previous studies, a Warburg-type behaviour may again be suspected as responsible [47].

x \ time	0	0.05	0.1	0.15	0.2	0.35	0.4
0s	0.426	0.313	0.149	1.096	2.269	0.514	0.046
60s	0.423	0.311	0.151	0.485	2.100	0.149	0.039
120s	0.424	0.021	0.010	0.109	0.515	0.004	0.000
300s	0.426	0.001	0.000	0.000	0.040	0.000	0.000

Table 20. Conductivity ( $S\text{ cm}^{-1}$ ) against time (s) for samples of  $Sr_{0.8}Ti_{0.6}Nb_{0.4-x}V_xO_{3-\delta}$  exposed to air post reduction in 5% $H_2/N_2$

Table 20 and Figure 46 shows a selection of conductivities against time for selected samples of  $Sr_{0.8}Ti_{0.6}Nb_{0.4-x}V_xO_{3-\delta}$  exposed to air post reduction. As can be seen, all samples containing vanadium rapidly dropped towards negligible conductivity once exposed to an oxidising environment. This clearly contrasts with the vanadium-free sample of  $Sr_{0.8}Ti_{0.6}Nb_{0.4}O_{3-\delta}$  which remained at a fairly consistent conductivity despite the change in environment. It should be noted that the conductivity of this undoped sample remained at  $0.417\text{ S cm}^{-1}$  after 30 minutes of exposure to air at  $800\text{ }^\circ\text{C}$ , however the drop recorded may be due to temperature fluctuations caused by opening the furnace chamber to air.

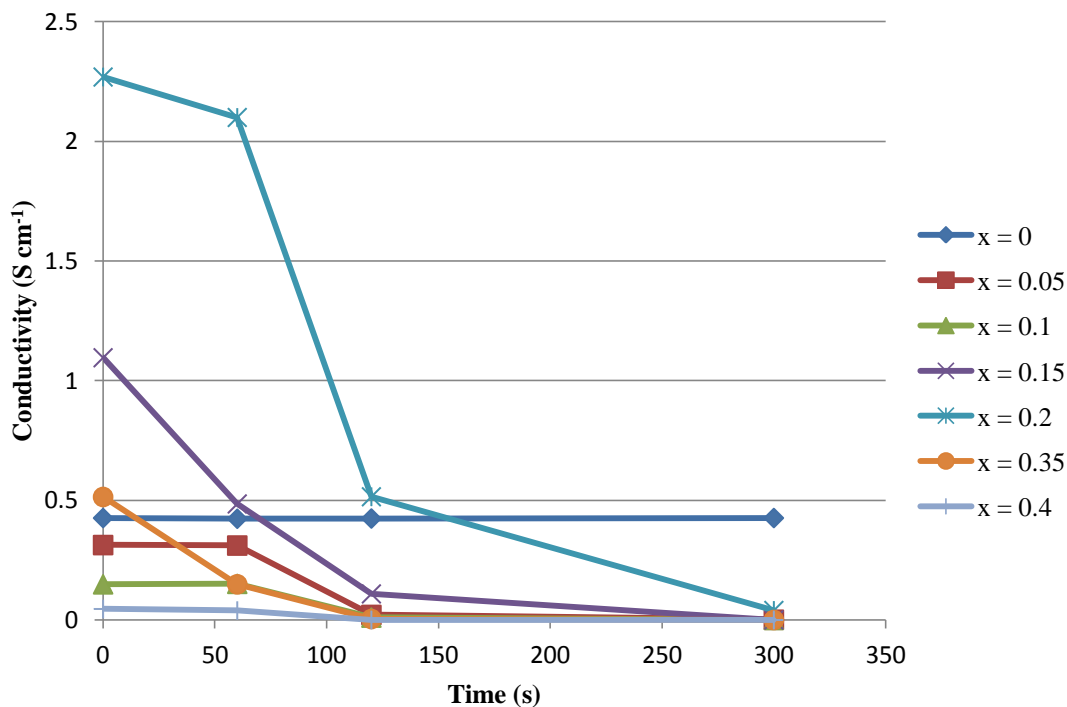


Figure 46. Conductivity against time for samples of  $Sr_{0.8}Ti_{0.6}Nb_{0.4-x}V_xO_{3-\delta}$  exposed to air at 800 °C post reduction in 5% $H_2/N_2$  at 930 °C

While these data cannot be used to directly measure oxygen transfer, it can be inferred that oxygen transfer is improved in the doped samples versus the undoped. However, the level of doping appears to have little influence on the rate of reoxidation, with all vanadium-containing samples dropping several orders of magnitude within 5 minutes.

### 6.3.6. Dilatometry

Dilatometry studies were carried out on both  $Sr_{0.8}Ti_{0.6}Nb_{0.4}O_{3-\delta}$  and  $Sr_{0.8}Ti_{0.6}Nb_{0.2}V_{0.2}O_{3-\delta}$  in air. The results are shown in Table 21, Figure 47 and Figure 48.

Sample	TEC ( $\times 10^{-6}$ /K)
$\text{Sr}_{0.8}\text{Ti}_{0.6}\text{Nb}_{0.4}\text{O}_{3-\delta}$	11.73
$\text{Sr}_{0.8}\text{Ti}_{0.6}\text{Nb}_{0.2}\text{V}_{0.2}\text{O}_{3-\delta}$	12.65

Table 21. TEC data for the materials  $\text{Sr}_{0.8}\text{Ti}_{0.6}\text{Nb}_{0.4}\text{O}_{3-\delta}$  and  $\text{Sr}_{0.8}\text{Ti}_{0.6}\text{Nb}_{0.2}\text{V}_{0.2}\text{O}_{3-\delta}$

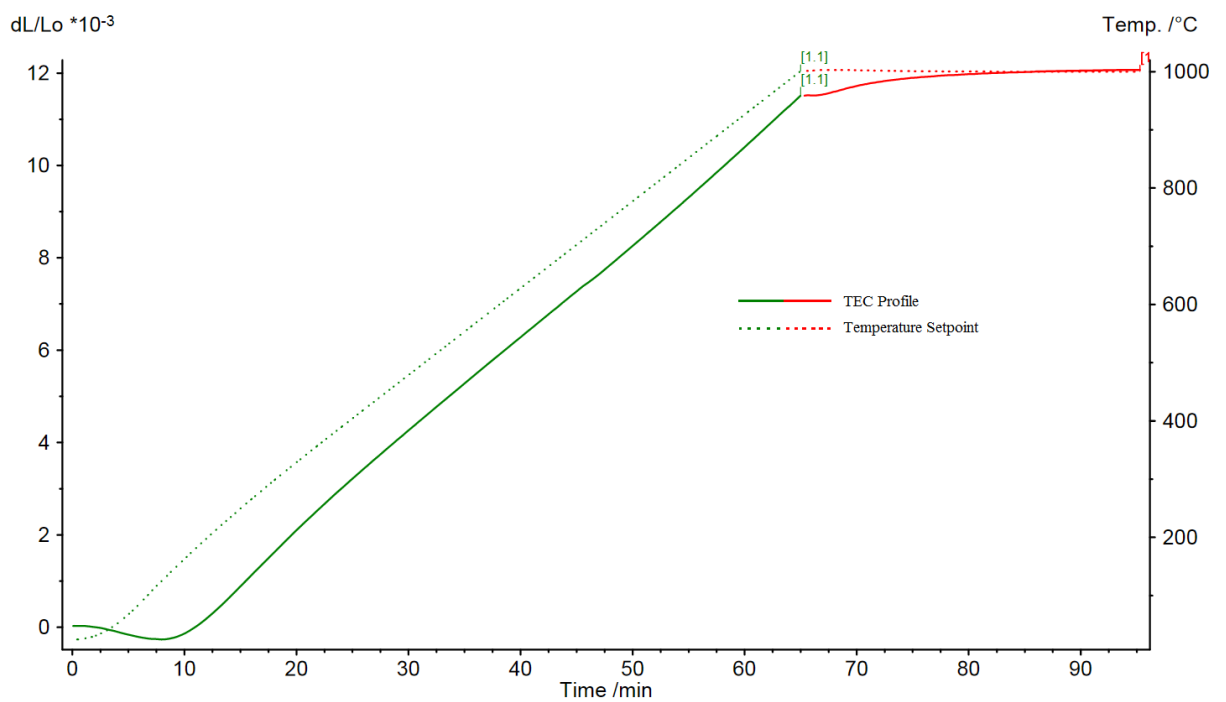


Figure 47. Dilatometry data for  $\text{Sr}_{0.8}\text{Ti}_{0.6}\text{Nb}_{0.4}\text{O}_{3-\delta}$  from 20 - 1000 °C at 15 °C min<sup>-1</sup> in air. Solid line is TEC profile, dashed line is temperature profile

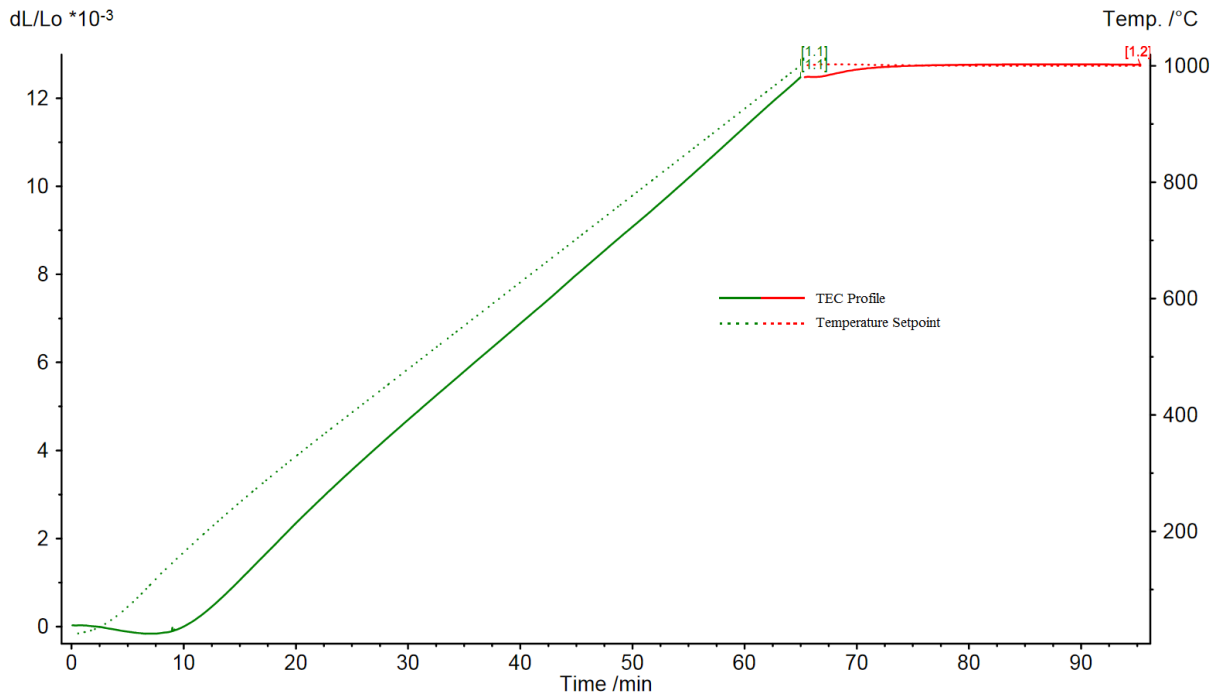


Figure 48. Dilatometry data for  $Sr_{0.8}Ti_{0.6}Nb_{0.2}V_{0.2}O_{3-\delta}$  from 20 - 1000 °C at 15 °C min<sup>-1</sup> in air. Solid line is TEC profile, dashed line is temperature profile

As can be seen, the TEC is larger for the vanadium doped samples than for the undoped. This is in line with expectations, as the vanadium-containing sample is much more prone to losing oxygen upon heating, leading to a slight average increase in B-site cation radius.

Both samples displayed a very slight increase in the rate of expansion above ~700 °C which may be attributed to the loss of oxygen leading to the reduction (and subsequent increase in radius) of the Nb/V on the B site. However, this increase in expansion rate is small, suggesting limited reduction in air.

## 6.4. Conclusions and Further Work

This work has demonstrated that it is possible to replace niobium with vanadium in the perovskite material  $\text{Sr}_{0.8}\text{Ti}_{0.6}\text{Nb}_{1-x}\text{V}_x\text{O}_{3-\delta}$  while retaining phase purity. The inclusion of some vanadium improves the reoxidation behaviour and the conductivity in reducing conditions over the undoped sample; however, over  $x = 0.2$  the performance decreased. Thermal expansion coefficients are a close match for existing SOFC materials such as YSZ ( $10.5 \times 10^{-6} / \text{K}$ ); however, further work needs to be carried out to ascertain the chemical compatibility with such systems. Additional work investigating V doping of other  $\text{Sr}_{1-x/2}\text{Ti}_{1-x}\text{Nb}_x\text{O}_{3-\delta}$  systems, or doping into  $\text{Sr}_{1-3x/2}\text{La}_x\text{TiO}_3$ , may also give further insight into some of the unexpected characteristics of  $\text{Sr}_{0.8}\text{Ti}_{0.6}\text{Nb}_{0.4-x}\text{V}_x\text{O}_{3-\delta}$ . In-situ studies of these materials as part of a solid oxide fuel cell should also provide valuable insights into material performance.

# **Chapter 7. Synthesis and characterisation of $\text{La}_{1-x}\text{Mn}_x\text{Mn}_{1-x}\text{Ti}_x\text{O}_{3-\delta}$ for SOFC applications**

## **7.1. Introduction**

In terms of stationary power applications, Solid Oxide Fuel Cells (SOFCs) have attracted considerable interest due to their high efficiencies and fuel flexibility. The most widely used system within the anode of SOFCs has been Ni dispersed into a matrix of electrolyte material such as CGO or YSZ [14, 191]. While demonstrating for the most part excellent performance, this cermet anode is not without its problems, in particular a tendency for coking at elevated temperatures, as well as sulphur poisoning when using hydrocarbon fuels such as natural gas. Consequently there has been considerable interest in the development of new anode materials as outlined in many review articles [160, 161]. In particular, mixed metal oxides that are redox stable are attracting growing interest, driven by the expectation that they will be less susceptible to the coking or sulphur poisoning problems associated with Ni [35, 38, 45, 46, 50, 61, 146, 148, 192–200]. In this respect, perovskite systems of the general formula  $\text{ABO}_3$  have attracted considerable interest including Ti, Cr/Mn, and Mo based systems [50, 61, 160, 161]. Doped titanate systems, based around  $\text{SrTiO}_3$ , were one of the first perovskite systems to be investigated for use within SOFC anodes [35]. Undoped  $\text{SrTiO}_3$  was found to be difficult to reduce, even at the high operating temperatures of a SOFC. This difficulty in reducing  $\text{SrTiO}_3$  led to low electronic conductivity. However, through doping on either the Sr or Ti sites, samples with conductivities up to  $10 \text{ S cm}^{-1}$  were obtained [45, 199],

with further improvements possible via pre-reduction at temperatures up to 1400 °C [38]. This reasonable electronic conduction was not reflected in oxide ion conductivity, which remained low. This was thought to be in part due to the lack of oxide ion vacancies in the material.

In separate studies, the perovskite series  $\text{LaMnO}_3$  has been investigated as a potential material for use within the cathode of SOFCs [34]. When doped with Sr this series has high levels of electronic conductivity and is stable at operating temperatures present within functioning fuel cells. The good electronic conductivity has been attributed to the mixed valency of manganese, present as both  $\text{Mn}^{3+}$  and  $\text{Mn}^{4+}$ . Manganese was found to readily reduce and so these materials were examined further for use within SOFC anodes, however the ease with which manganese is reduced directly correlates to redox stability [73, 74].

With a view to trying to improve the conducting properties and stability under reducing conditions, we have investigated a series of mixed Mn/Ti based perovskites. The starting point of the series examined is  $\text{LaMnO}_3$ , a traditional SOFC cathode material when doped with Sr.  $\text{LaMnO}_3$  itself has orthorhombic symmetry below 750K where it undergoes a phase change to a cubic system [201]. In order to create a potentially redox stable material capable of being used as a SOFC anode, the substitution of  $\text{Ti}^{4+}$  in place of  $\text{Mn}^{3+}$  has been examined, with charge balance achieved through introduction of  $\text{Mn}^{2+}$  on the  $\text{La}^{3+}$  site, giving the formula  $\text{La}_{1-x}\text{Mn}_x\text{Mn}_{1-x}\text{Ti}_x\text{O}_3$ . The introduction of a mixed manganese-titanium system is an attempt to improve the oxide ion conductivity over most titanates while retaining the redox stability of  $\text{SrTiO}_3$ , and also providing an n-type

electronic contribution under reducing conditions. This Chapter reports results from the synthesis of samples in the series  $\text{La}_{1-x}\text{Mn}_x\text{Mn}_{1-x}\text{Ti}_x\text{O}_3$ , investigating their conductivities in air and 5%  $\text{H}_2/\text{N}_2$  [202].

## 7.2. Experimental

High purity  $\text{La}_2\text{O}_3$ ,  $\text{SrCO}_3$ ,  $\text{MnO}_2$ ,  $\text{TiO}_2$  were used to prepare the samples of  $\text{La}_{1-x}\text{Mn}_x\text{Mn}_{1-x}\text{Ti}_x\text{O}_{3-\delta}$  ( $x = 0.2 - 0.5$ ). The powders were intimately ground and heated initially to 1100 °C for 12h. They were then ball-milled (350 rpm for 1 hour, Fritsch Pulverisette 7 Planetary Mill with 2 milling beads) and reheated to 1300 - 1350 °C for a further 12h. Powder X-ray diffraction (Bruker D8 diffractometer with  $\text{Cu K}\alpha_1$  radiation) was used to demonstrate phase purity. Unit cell parameter refinement was carried out using GSAS suite of programs [123, 124]. Samples were also exposed to 5%  $\text{H}_2/\text{N}_2$  for 24 hours at 800 °C to determine their stability in reducing conditions.

Pellets for conductivity measurements were prepared as follows: the powders were first ball-milled (350 rpm for 1 hour with 2 milling beads, Fritsch Pulverisette 7 Planetary Mill), before pressing as pellets of 13 mm diameter and sintering at 1300 - 1400 °C for 12h. Conductivities were then measured using the 4 probe DC method in both air and 5%  $\text{H}_2/\text{N}_2$ .

## 7.3. Results and Discussion

### 7.3.1. Synthesis and Structure Determination

Figure 49, Figure 50 and Figure 51 show the XRD patterns for several materials in the series  $\text{La}_{1-x}\text{Mn}_x\text{Mn}_{1-x}\text{Ti}_x\text{O}_{3-\delta}$ . Following the synthesis conditions outlined above, the XRD data showed near single phase samples for  $x \leq 0.4$ , with  $\text{La}_2\text{Ti}_2\text{O}_7$  impurities observed for higher Ti levels. Table 22 displays the unit cell parameters and volumes for the series. Small secondary peaks become more apparent at higher values of  $x$ , possibly indicating the formation of a more complex double perovskite system with some  $\text{LaMnO}_3$  or  $\text{MnTiO}_3$  impurity phases present.

x	0 [203]	0.2	0.3	0.4
a (Å)	5.582	5.4938	5.4988	5.5095
b (Å)	5.515	5.5327	5.5500	5.5417
c (Å)	7.763	7.8067	7.7826	7.8329
Volume (Å <sup>3</sup> )	238.98	237.29	237.51	239.15

Table 22. Unit cell parameters and cell volumes for the series  $\text{La}_{1-x}\text{Mn}_x\text{Mn}_{1-x}\text{Ti}_x\text{O}_3$

As it can be seen, the unit cell expands as  $x$  increases. This increase is unexpected; a decrease is anticipated due to the decrease in average cation size on the A-site, with  $\text{La}^{3+}$  having a larger cationic radius of 1.16 Å against  $\text{Mn}^{2+}$  at 0.96 Å, while the B-site cation

size varies much less with  $\text{Ti}^{4+}$  at 0.605 Å against  $\text{Mn}^{3+}$  at 0.58 Å and  $\text{Mn}^{4+}$  at 0.53 Å [174]. A possible explanation for this is that there is no manganese present on the A-site; in this scenario, charge balancing may have been achieved through cation vacancies on the A site, giving composites such as  $\text{La}_{1-x/3}\text{Mn}_{1-x}\text{Ti}_x\text{O}_3$ . This possibility is reinforced by noting that the literature values for undoped  $\text{LaMnO}_3$  show a larger unit cell than the doped samples, indicating possible vacancies within the unit cell of the doped samples.

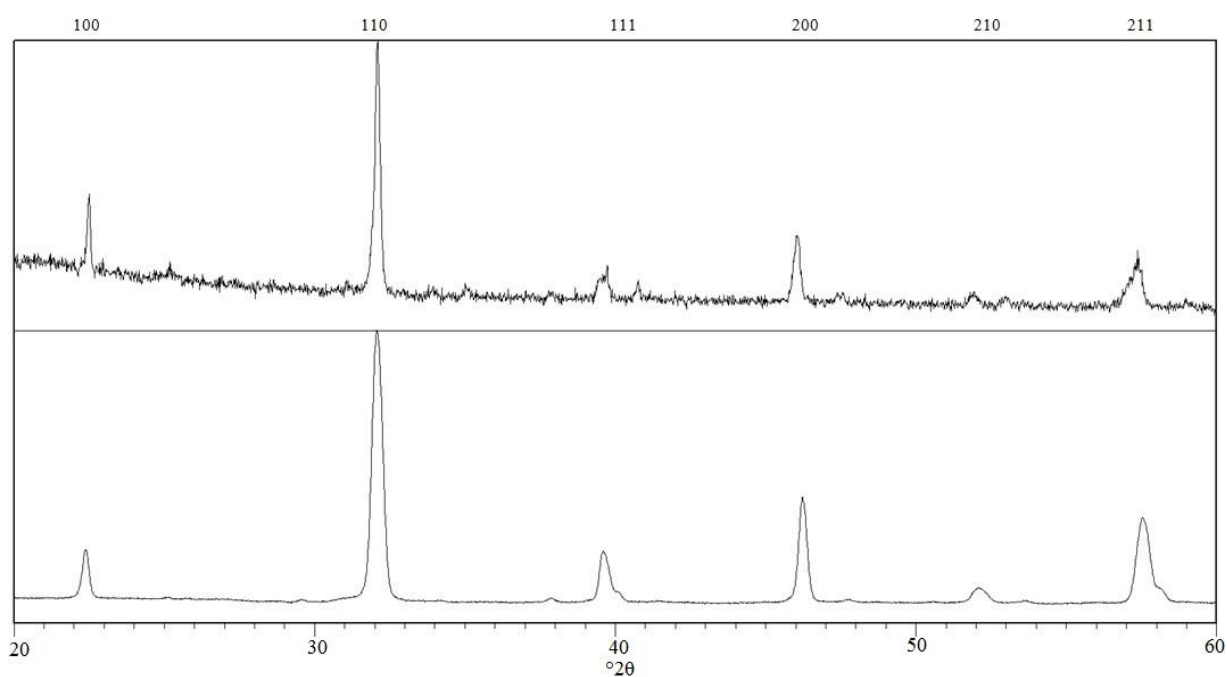


Figure 49. XRD pattern for  $\text{La}_{0.8}\text{MnTi}_{0.2}\text{O}_{3-\delta}$  in air (bottom) and annealed in 5%  $\text{H}_2/\text{N}_2$  at 800 °C for 24 hours (top)

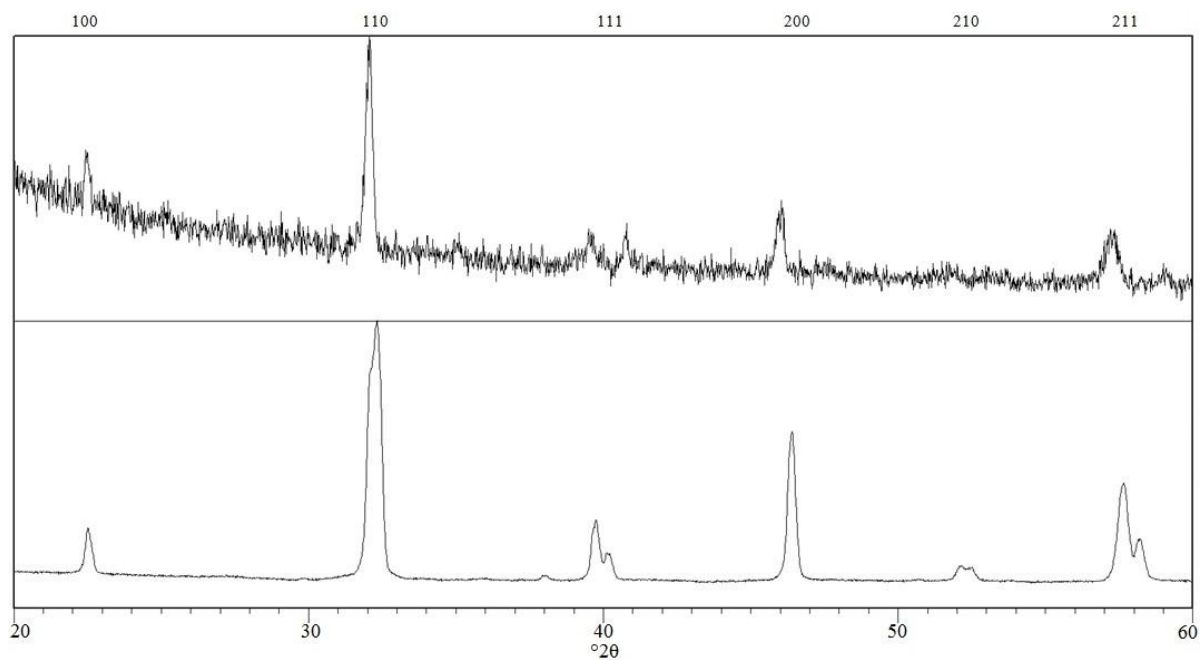


Figure 50. XRD pattern for  $La_{0.7}MnTi_{0.3}O_{3-\delta}$  in air (bottom) and annealed in 5% $H_2/N_2$  at 800 °C for 24 hours (top)

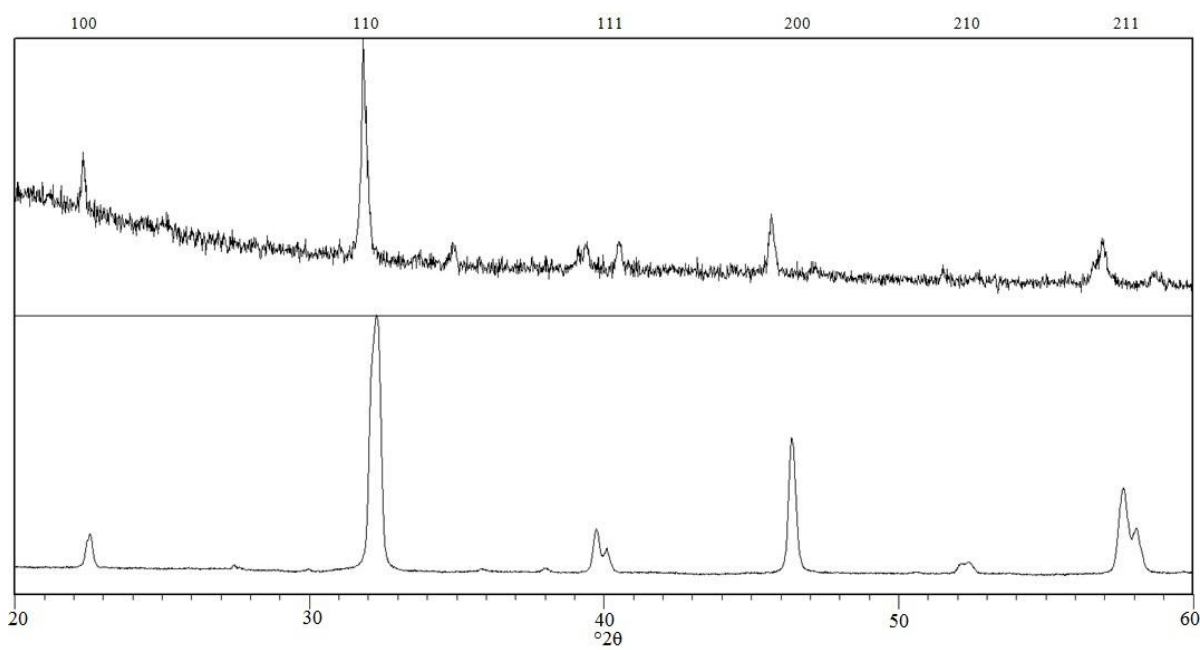


Figure 51. XRD pattern for  $La_{0.6}MnTi_{0.4}O_{3-\delta}$  in air (bottom) and annealed in 5% $H_2/N_2$  at 800 °C for 24 hours (top)

Another interesting detail to note is the small peak at a 2 theta value of  $\sim 38^\circ$ . This shows the presence of a small quantity of  $\text{LaMnO}_3$  as detailed in both the Crystallography Open Database and the literature, helping to verify the formation of an alternate perovskite system [204]. Many of the peaks for  $\text{LaMnO}_3$  and  $\text{LaTiO}_3$  overlap slightly with the main phase which helps to explain the shoulders and secondary peaks [205].

As expected, the peaks for the samples reduced in 5% $\text{H}_2/\text{N}_2$  shift to lower  $2\theta$  values, showing that some degree of expansion is taking place due to the reduction of one or more of the cation species present. The XRD patterns for the reduced samples also suggest that the phases are not fully stable under these conditions as extra peaks are seen. The peak that can be seen at  $\sim 35^\circ$  and the secondary peak at  $\sim 40.5^\circ$  in the reduced samples indicates the presence of  $\text{MnO}$  [206]. This becomes more pronounced as more Mn is present on the A-site, possibly suggesting the breakdown of the crystal structure or the presence of an amorphous, Mn-rich phase in the as-prepared samples, which crystallises on reduction.

## **7.3.2. Conductivity Measurements**

### **7.3.2.1. Air Atmosphere**

Conductivity measurements were performed on samples of  $\text{La}_{0.6}\text{MnTi}_{0.4}\text{O}_3$ ,  $\text{La}_{0.7}\text{MnTi}_{0.3}\text{O}_3$  and  $\text{La}_{0.8}\text{MnTi}_{0.2}\text{O}_3$  ( $x = 0.4, 0.3$  and  $0.2$ ). Initial measurements were taken in air, and these results showed semiconductor behaviour with conductivities in the

range 1.6 to 12.5 S cm<sup>-1</sup> at 850 °C; the conductivities were lowest for samples with higher Ti content, as shown in Table 23, Figure 52 and Figure 53.

x	0.2	0.3	0.4
Conductivity (S cm <sup>-1</sup> ) at 800 °C	11.91	7.62	1.44
Conductivity (S cm <sup>-1</sup> ) at 700 °C	10.42	6.60	1.13

Table 23. Conductivity data in air for the series  $La_{1-x}Mn_xMn_{1-x}Ti_xO_3$

In addition, the activation energies also increased across the series as the Ti content (x) increased,  $E_a = 46.5, 49.2, 59.5$  kJ mol<sup>-1</sup> for x = 0.2, 0.3, 0.4 respectively as calculated from Figure 53. The decrease in conductivity in air with increasing Ti content is to be expected due to the disruption of the Mn-O network. These activation energies are higher than other similar systems: for example, SrFeO<sub>3-δ</sub> doped with Mo shows values between 19 - 34 kJ mol<sup>-1</sup> in air, while for La<sub>0.75</sub>Sr<sub>0.25</sub>Cr<sub>0.5</sub>Mn<sub>0.5</sub>O<sub>3-δ</sub> has activation energies of 20.2 kJ mol<sup>-1</sup> in air and 54 kJ mol<sup>-1</sup> in H<sub>2</sub> [49, 176, 207].

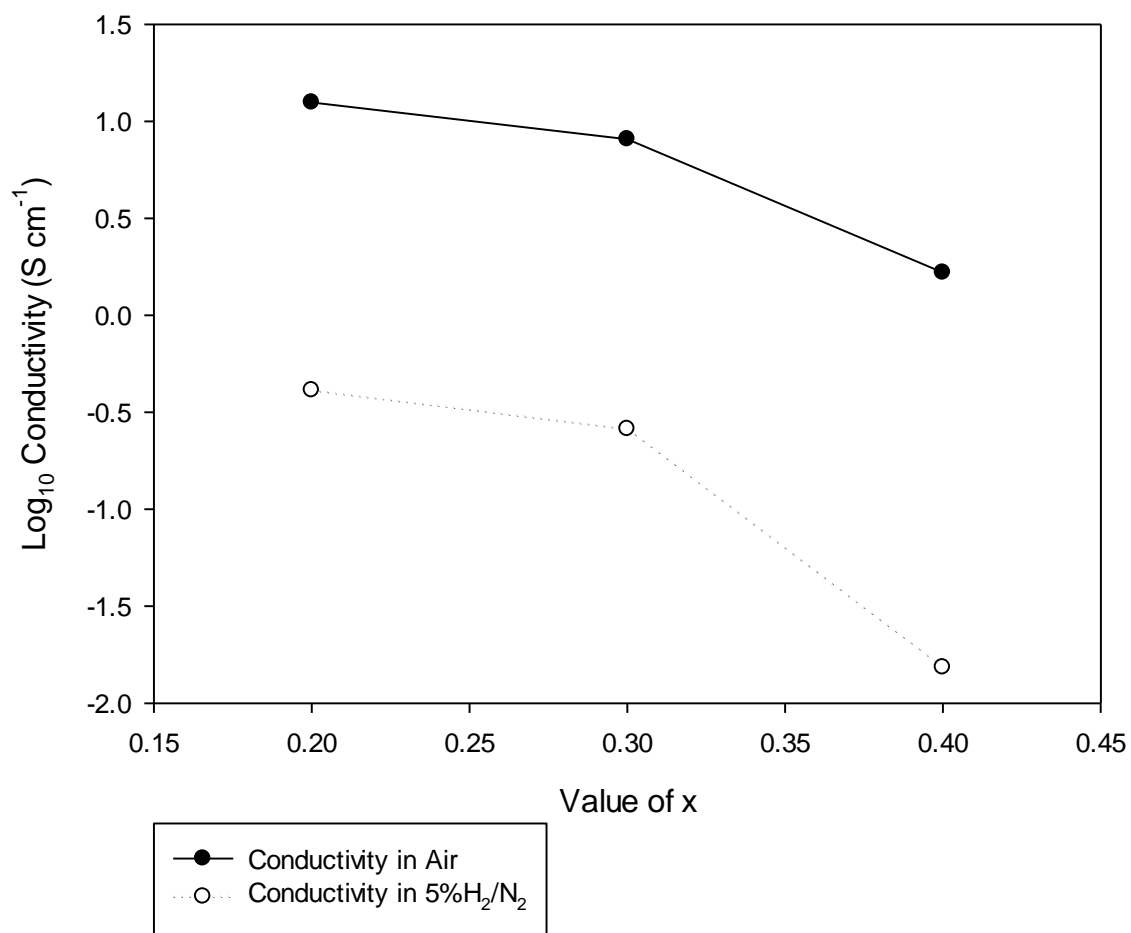


Figure 52. Variation in the conductivities of the series  $La_{1-x}Mn_xMn_{1-x}Ti_xO_{3-\delta}$  in air and 5% $H_2/N_2$  at 850 °C

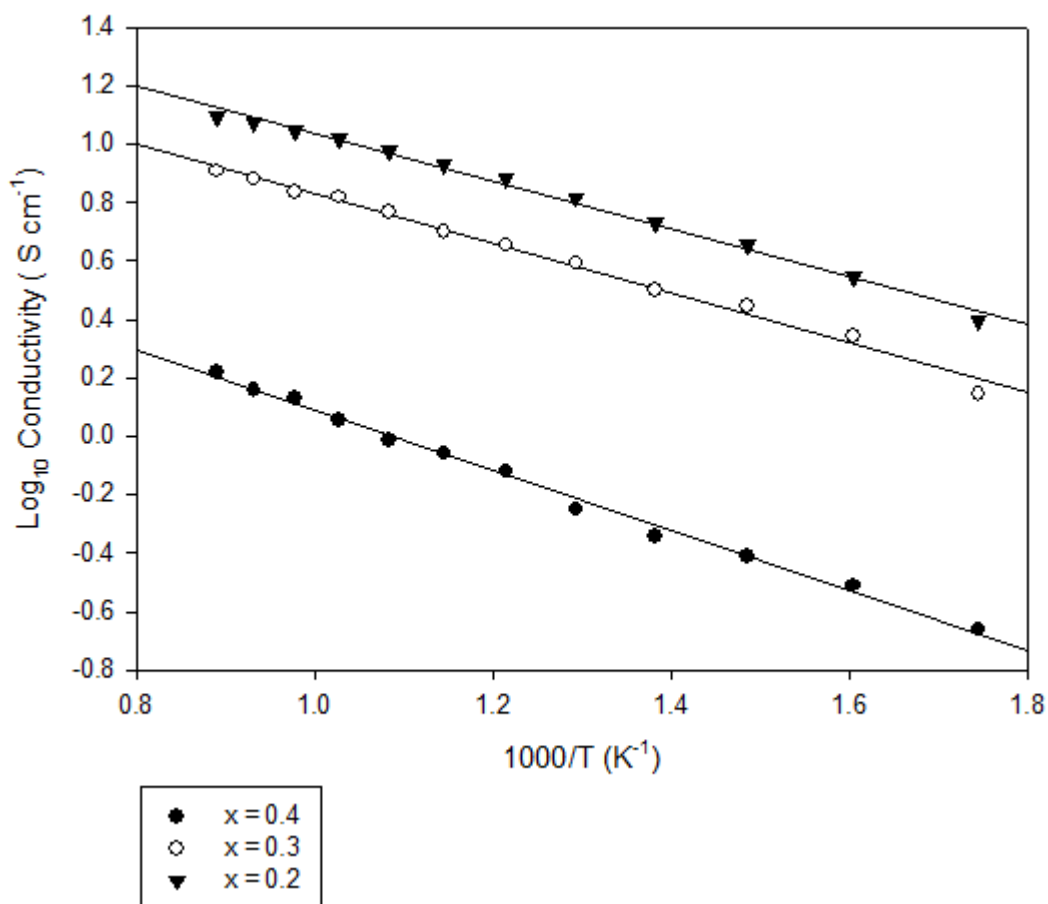


Figure 53.  $\text{Log}_{10} \sigma$  vs  $1000/T$  for the series  $\text{La}_{1-x}\text{Mn}_x\text{Mn}_{1-x}\text{Ti}_x\text{O}_{3-\delta}$  in air

### 7.3.2.2. Reducing Atmosphere

The conductivities were then measured under 5%  $\text{H}_2/\text{N}_2$ . Samples were heated in this atmosphere up to 850 °C and held for 1 hour before making measurements on cooling. The data showed that the electronic conductivities of all three samples dropped by several orders of magnitude, to be in the range of 0.015 to 0.4  $\text{S cm}^{-1}$ .

x	0.2	0.3	0.4
Conductivity (S cm <sup>-1</sup> ) at 800 °C	0.33	0.20	0.01
Conductivity (S cm <sup>-1</sup> ) at 700 °C	0.22	0.11	0.01

Table 24. Conductivity data in 5%H<sub>2</sub>/N<sub>2</sub> for the series La<sub>1-x</sub>Mn<sub>x</sub>Mn<sub>1-x</sub>Ti<sub>x</sub>O<sub>3</sub> in 5%H<sub>2</sub>/N<sub>2</sub>

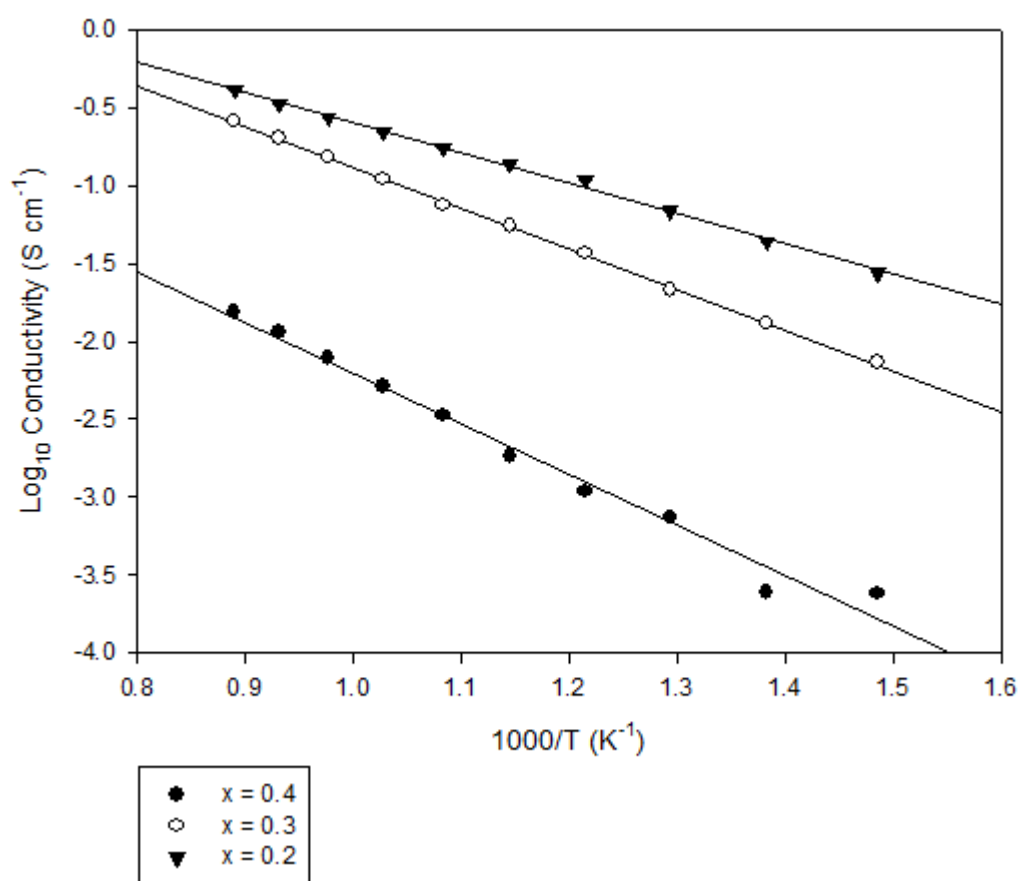


Figure 54. Graph of Log<sub>10</sub>  $\sigma$  vs 1000/T of series La<sub>1-x</sub>Mn<sub>x</sub>Mn<sub>1-x</sub>Ti<sub>x</sub>O<sub>3- $\delta$</sub>  in 5%H<sub>2</sub>/N<sub>2</sub>

As before, the lowest conductivities were observed for the samples with the higher Ti content. The range of difference between the samples is again apparent, with over an

order of magnitude difference between the  $x = 0.2$  and  $0.3$  and the  $x = 0.4$  samples at higher temperatures. The activation energies displayed the same trend once more, rising as  $x$  increases; with  $E_a = 188.0, 154.3, 114.8 \text{ kJ mol}^{-1}$  for  $x = 0.4, 0.3, 0.2$  respectively at  $800 \text{ }^\circ\text{C}$ , considerably higher than alternative materials [49]. Thus in addition to the lower conductivities, the activation energies are considerably higher than in air, especially for the high Ti content samples. The samples were analysed by XRD after the measurement, which confirmed that partial decomposition had occurred. In addition, the observed conductivities are too low for SOFC anode applications regardless of material redox stabilities.

#### **7.4. Conclusions**

In this work, a new series of perovskite systems has been synthesised,  $\text{La}_{1-x}\text{Mn}_x\text{Mn}_{1-x}\text{Ti}_x\text{O}_{3-\delta}$  ( $x \leq 0.4$ ), stable under SOFC cathode operating conditions and displaying partial decomposition in SOFC anode operating conditions. While reasonable conductivities were observed in air, the conductivities decreased substantially in reducing environments, indicating that these systems are not suitable for anode applications.

*Work within this Chapter has been published in the International Journal of Low-Carbon Technologies, Volume 7, Issue 1, Pages 60-62, 2011.*

## **Chapter 8. Conclusions and Further Work**

Current research suggests that perovskite materials have the potential to display suitable properties and characteristics as electrode materials for use within SOFCs. The doping of several systems proved moderately successful, with improvements over the original, undoped materials being recorded.

Oxyanion doping has proved a particularly viable strategy towards improving the performance of transition metal containing perovskite materials. In the present case of doping into  $\text{SrFeO}_{3-\delta}$ , this can partially be attributed to the stabilisation of the cubic phase in reducing environments, leading to a large increase in conductivity. Further work on this particular series could include more complete testing within a SOFC, further compatibility studies with existing electrolyte materials or doping with alternative oxyanions to study the effect on material characteristics in more detail. This oxyanion doping strategy has also proved successful in material systems other than perovskites, such as Ruddlesden Popper phases [64, 65, 67, 68, 171, 173, 208]. There is therefore wide scope for further work in this field, with a large range of materials potentially suitable for oxyanion doping.

For the  $\text{Sr}_{0.8}\text{Ti}_{0.6}\text{Nb}_{0.4}\text{O}_{3-\delta}$  materials, vanadium doping was shown to have a positive effect on conductivity. The best performance was in the material  $\text{Sr}_{0.8}\text{Ti}_{0.6}\text{Nb}_{0.2}\text{V}_{0.2}\text{O}_{3-\delta}$ , where the electronic conductivity in 5% $\text{H}_2/\text{N}_2$  was shown to be fairly stable across a range of temperatures from 800 to 300 °C, in the region of 2 - 6  $\text{S cm}^{-1}$ , after reduction at 930 °C. The undoped sample had previously shown good stability in reducing

conditions, albeit with a resistance to reoxidation caused by slow oxygen transport [146]. The V doped samples, in contrast, displayed far faster reoxidation, even with as little as 5% vanadium on the B-site, suggesting higher oxide ion conductivity. Thermal expansion coefficients were shown to be comparable with existing electrolyte materials such as YSZ, however further work on chemical compatibility with these existing SOFC materials is needed. Additional work investigating V doping of other  $\text{Sr}_{1-x/2}\text{Ti}_{1-x}\text{Nb}_x\text{O}_{3-\delta}$  systems may also give further insight into some of the unexpected cell parameter changes of  $\text{Sr}_{0.8}\text{Ti}_{0.6}\text{Nb}_{0.4-x}\text{V}_x\text{O}_{3-\delta}$ .

The  $\text{La}_{1-x}\text{Mn}_x\text{Mn}_{1-x}\text{Ti}_x\text{O}_{3-\delta}$  series of materials proved less successful. It proved difficult to obtain phase pure samples in many cases, with small secondary peaks visible at higher x values. In addition, after reduction at 800 °C in 5% $\text{H}_2/\text{N}_2$  it can be seen that the structure is degraded, indicating instability under these conditions. Nevertheless, reasonable conductivities were obtained in air, with the highest values recorded for the x = 0.2 sample. Some questions remain over whether there is indeed the incorporation of Mn onto the A-site, with the possibility of the formation of A-site deficient structures instead. This would require further verification by other techniques such as combined X-ray and neutron diffraction studies in order to accurately determine site occupancies.

The extrusion work also proved problematic, with issues surrounding repeatability and cell performance. While the work carried out appears to indicate the successful formation of tubes, these suffered from irregularities in wall thickness. In addition, many variations around material layering and cell preparation failed to produce a successful cell. In order for additional work to be viable, the extrusion die may need redesigning to allow greater

rigidity and so more regular tube sizes, and layering techniques would require further investigation to provide more repeatable results.

Moving forward, work into perovskite-based SOFCs could be driven forward through further fabrication of cells in order to form stacks, allowing increased testing profiles to be carried out on completed cells to better characterise the materials and properties. A wider selection of fuels, including the ability to introduce potential contaminants and poisons into the fuel mix, would also allow much greater in-situ analysis of materials under various performance conditions. The ability to introduce known contaminants into fuel streams, or even to run directly off the national gas grid, has the potential to prove the suitability of novel materials and demonstrate in-situ performance.

If in-situ analysis of novel materials was to progress on a larger scale, the ability to fabricate planar cells would simplify the process and, if a uniform cell size was established, cell sealing could be made more straightforward which would allow faster changeover of cells analysed. It would also facilitate more straightforward stack building if gasket materials and cell interconnects could be established, allowing far greater range and duration of testing protocols. This work could compliment work on m-SOFCs which could provide faster verification of suitability of materials due to their better thermal characteristics.

Integration of SOFCs into buildings as part of CHP systems would allow in-situ testing of systems and principals for widespread use of fuel cell systems as part of a microgeneration energy solution. Development of protocols for start-up, shut down and

load cycling, amongst other things, could help to build up the requirements for future progress in the area. In addition, data could be transmitted and processed in real time, allowing remote monitoring of the system and easing the expansion of such a program by facilitating centralised system control and development.

Many of these goals could be achieved through the creation of a spin-out company, supported directly by universities, allowing for transfer of knowledge and access to facilities while enabling the pursuit of more business- and production-oriented development. This would allow greater autonomy and the potential to build business arrangements with larger companies better positioned in the market to roll out future technologies, possibly to a degree above and beyond that which a university could support directly. In addition, by focussing less on the development of novel materials, cells and systems, and more on marketisation, it would have the potential to increase the speed at which products become commercially viable.

## **Chapter 9. Publications**

T. W. Pike, P. R. Slater, *International Journal of Low Carbon Technologies*, Volume 7, Issue 1, Pages 60-62 (2011).

J. Porras-Vazquez, T. Pike, C. A. Hancock, J.F. Marco, F. J. Berry, P. R. Slater, *Journal of Materials Chemistry A*, Volume 3, Issue 38, Pages 11834 - 11841 (2013).

## **Chapter 10. References**

1. A. B. Lovins, *Reinventing Fire: Bold Business Solutions for the New Energy Era*, Chelsea Green Publishing, 2011.
2. F. K. Boese, a. Merkel, D. Stahl, H. Stehle, *Solar Energy* **26**, 1–7 (1981).
3. *World Wind Association Half-year Report* (2013).
4. J. Bennetsen, *Construction* **VI** (2012).
5. Geothermal Energy Association Report, 2013.
6. J. Levene, B. Kroposki, G. Sverdrup, 2006.
7. J. R. Varcoe, R. C. T. Slade, *Fuel Cells* **5**, 187–200 (2005).
8. C. Zuo, S. Zha, M. Liu, M. Hatano, M. Uchiyama, *Advanced Materials* **18**, 3318–3320 (2006).
9. V. M. Goldschmidt, *Skifter Norske Videnskaps-Akademi i Oslo, I. Mat.-.Nat* **K1** (1926).
10. C. Li, K. C. K. Soh, P. Wu, *Journal of Alloys and Compounds* **372**, 40–48 (2004).
11. C. Greaves, A. J. Jacobson, B. C. Tofield, B. E. F. Fender, *Acta Crystallographica Section B* **31**, 641–646 (1975).

12. B. C. Tofield, C. Greaves, B. E. F. Fender, *Materials Research Bulletin* **10**, 737–745 (1975).
13. H. S. Spacil, Electrical device including nickel-containing stabilized zirconia electrode, United States, 1970.
14. D. Dees, T. Claar, T. Easler, *Journal of The Electrochemical Society* **134**, 2141–2146 (1987).
15. S. Taylor, Investigation Into The Improved Dispersion of Nickel Oxide Over the Surface of SOFC Tubular Anodes, University of Birmingham (2010).
16. Y. Matsuzaki, I. Yasuda, *Solid State Ionics* **132**, 261–269 (2000).
17. Z. Cheng, M. Liu, *Solid State Ionics* **178**, 925–935 (2007).
18. N. Akhtar, S. P. Decent, D. Loghin, K. Kendall, *Journal of Power Sources* **193**, 39–48 (2009).
19. A. Dhir, K. Kendall, *Journal of Power Sources* **181**, 297–303 (2008).
20. A. Dhir, Improved Microtubular Solid Oxide Fuel Cells, University of Birmingham (2008).
21. H. He, J. M. Hill, *Applied Catalysis A: General* **317**, 284–292 (2007).
22. H. Kan, S. H. Hyun, Y.-G. Shul, H. Lee, *Catalysis Communications* **11**, 180–183 (2009).
23. C. M. Grgicak, R. G. Green, J. B. Giorgi, *Journal of Power Sources* **179**, 317–328 (2008).
24. A. Lashtabeg, S. J. Skinner, *Journal of Materials Chemistry* **16**, 3161–3170 (2006).
25. Z. Lü, L. Pei, T. He, X. Huang, Z. Liu, Y. Ji, *Journal of Alloys and Compounds* **334**, 299–303 (2002).
26. H. Kim, C. Lu, W. L. Worrell, J. M. Vohs, R. J. Gorte, *Journal of The Electrochemical Society* **149**, A247 (2002).
27. A. Hornés, D. Gamarra, G. Munuera, J. C. Conesa, A. Martínez-Arias, *Journal of Power Sources* **169**, 9–16 (2007).
28. A. Sin, E. Kopnin, Y. Dubitsky, A. Zaopo, A. S. Aricò, D. La Rosa, L. R. Gullo, V. Antonucci, *Journal of Power Sources* **164**, 300–305 (2007).

29. J. C. Ruiz-Morales, J. Canales-Vazquez, D. Marrero-Lopez, J. Pena-Martinez, A. Tarancon, J. T. S. Irvine, P. Nunez, *Journal of Materials Chemistry* **18**, 5072–5077 (2008).
30. B. C. H. Steele, *Solid State Ionics* **129**, 95–110 (2000).
31. B. C. H. Steele, *Journal of Power Sources* **49**, 1–14 (1994).
32. H. Yokokawa, H. Tu, B. Iwanschitz, A. Mai, *Journal of Power Sources* **182**, 400–412 (2008).
33. B. Iwanschitz, L. Holzer, A. Mai, M. Schütze, *Solid State Ionics* **211**, 69–73 (2012).
34. C. S. Tedmon, H. S. Spacil, S. P. Mitoff, *Journal of The Electrochemical Society* **116**, 1170 (1969).
35. P. R. Slater, D. P. Fagg, J. T. S. Irvine, *Journal of Materials Chemistry* **7**, 2495–2498 (1997).
36. D. Fagg, S. Fray, J. Irvine, *Solid State Ionics* **72**, 235–239 (1994).
37. S. Hui, A. Petric, *Journal of The Electrochemical Society* **149**, J1–J10 (2002).
38. S. Hui, A. Petric, *Journal of the European Ceramic Society* **22**, 1673–1681 (2002).
39. D. Neagu, J. J. T. S. Irvine, *Chemistry of Materials* **23**, 1607–1617 (2011).
40. J. Perez-Flores, *Chemistry of Materials* **25**, 2484–2494 (2013).
41. X. Li, H. Zhao, X. Zhou, N. Xu, Z. Xie, N. Chen, *International Journal of Hydrogen Energy* **35**, 7913–7918 (2010).
42. E. Y. Konyshva, X. Xu, J. T. S. Irvine, *Advanced Materials* **24**, 528–32 (2012).
43. C. Navas, H. zur Loye, *Solid State Ionics* **93**, 171–176 (1996).
44. M. Mori, Z. Wang, T. Itoh, S. Yabui, K. Murai, T. Moriga, *Journal of Fuel Cell Science and Technology* **8**, 51014 (2011).
45. P. R. Slater, J. T. S. Irvine, *Solid State Ionics* **120**, 125–134 (1999).
46. P. R. Slater, J. T. S. Irvine, *Solid State Ionics* **124**, 61–72 (1999).
47. A. Kaiser, J. L. Bradley, P. R. Slater, J. T. S. Irvine, *Solid State Ionics* **135**, 519–524 (2000).
48. L. Adijanto, R. Küngas, J. Park, J. M. Vohs, R. J. Gorte, *International Journal of Hydrogen Energy* **36**, 15722–15730 (2011).

49. S. Tao, J. T. S. Irvine, *Journal of The Electrochemical Society* **151**, A252–A259 (2004).
50. S. Tao, J. T. S. Irvine, *Nature Materials* **2**, 320–323 (2003).
51. J. Liu, B. D. Madsen, Z. Ji, S. A. Barnett, *Electrochemical and Solid-State Letters* **5**, A122–A124 (2002).
52. X. J. Chen, Q. L. Liu, S. H. Chan, N. P. Brandon, K. A. Khor, *Journal of The Electrochemical Society* **154**, B1206 (2007).
53. J. E. Sunstrom, S. M. Kauzlarich, P. Klavins, *Chemistry of Materials* **4**, 346–353 (1992).
54. O. O. A. Marina, N. N. L. N. Canfield, J. W. J. Stevenson, *Solid State Ionics* **149**, 21–28 (2002).
55. D. N. Miller, J. T. S. Irvine, *Journal of Power Sources* **196**, 7323–7327 (2011).
56. V. A. Kolotygin, E. V. Tsipis, A. I. Ivanov, Y. A. Fedotov, I. N. Burmistrov, D. A. Agarkov, V. V. Sinitsyn, S. I. Bredikhin, V. V. Kharton, *Journal of Solid State Electrochemistry* **16**, 2335–2348 (2012).
57. S. Hui, A. Petric, *Solid State Ionics* **143**, 275–283 (2001).
58. A. Aguadero, C. de la Calle, J. A. Alonso, D. Pérez-Coll, M. J. Escudero, L. Daza, *Journal of Power Sources* **192**, 78–83 (2009).
59. L. Zhang, Q. Zhou, Q. He, T. He, *Journal of Power Sources* **195**, 6356–6366 (2010).
60. Y.-H. Huang, R. I. Dass, Z.-L. Xing, J. B. Goodenough, *Science* **312**, 254–257 (2006).
61. Y.-H. Huang, G. Liang, M. Croft, M. Lehtimäki, M. Karppinen, J. B. Goodenough, *Chemistry of Materials* **21**, 2319–2326 (2009).
62. Y. Matsuda, M. Karppinen, Y. Yamazaki, H. Yamauchi, *Journal of Solid State Chemistry* **182**, 1713–1716 (2009).
63. J. F. Shin, L. Hussey, A. Orera, P. R. Slater, *Chemical Communications* **46**, 4613–5 (2010).
64. J. F. Shin, K. Joubel, D. C. Apperley, P. R. Slater, *Dalton transactions* **41**, 261–6 (2012).
65. J. F. Shin, A. Orera, D. C. Apperley, P. R. Slater, *Journal of Materials Chemistry* **21**, 874 (2011).

66. C. A. Hancock, R. C. T. Slade, J. R. Varcoe, P. R. Slater, *Journal of Solid State Chemistry* **184**, 2972–2977 (2011).
67. J. M. Porras-Vazquez, P. R. Slater, *Fuel Cells* **12**, 1056–1063 (2012).
68. J. M. Porras-Vazquez, T. F. Kemp, J. V. Hanna, P. R. Slater, *Journal of Materials Chemistry* **22**, 8287 (2012).
69. Q. Liu, D. E. Bugaris, G. Xiao, M. Chmara, S. Ma, H.-C. zur Loye, M. D. Amiridis, F. Chen, *Journal of Power Sources* **196**, 9148–9153 (2011).
70. M. Retuerto, M. Li, Y. Go, A. Ignatov, *Inorganic Chemistry* , 12273–12280 (2012).
71. R. Martínez-Coronado, A. Aguadero, J. A. Alonso, M. T. Fernández-Díaz, *Materials Research Bulletin* **47**, 2148–2153 (2012).
72. R. Martínez-Coronado, J. A. Alonso, A. Aguadero, M. T. Fernández-Díaz, *Journal of Power Sources* **208**, 153–158 (2012).
73. J. Kuo, H. Anderson, D. Sparlin, *Journal of Solid State Chemistry* **83**, 52–60 (1989).
74. N. Q. Minh, *Journal of the American Ceramic Society* **76**, 563–588 (1993).
75. A. Hammouche, E. Siebert, A. Hammou, *Materials Research Bulletin* **24**, 367–380 (1989).
76. S. P. Jiang, *Journal of Materials Science* **43**, 6799–6833 (2008).
77. P. Plonczak, M. Gazda, B. Kusz, P. Jasinski, *Journal of Power Sources* **181**, 1–7 (2008).
78. H. Ullmann, N. Trofimenko, F. Tietz, D. Stover, *Solid State Ionics* **138**, 79–90 (2000).
79. D. M. Bastidas, S. Tao, J. T. S. Irvine, *Journal of Materials Chemistry* **16**, 1603–1605 (2006).
80. H. Ullmann, N. Naoumidis, D. Stöver, *Journal of the European Ceramic Society* **19**, 791–796 (1999).
81. J. Molenda, K. Świerczek, W. Zając, *Journal of Power Sources* **173**, 657–670 (2007).
82. R. Martínez-Coronado, A. Aguadero, C. de la Calle, M. T. Fernández, J. A. Alonso, *Journal of Power Sources* **196**, 4181–4186 (2011).
83. S. Zha, Z. Cheng, M. Liu, *ECS Transactions* **1**, 293–302 (2006).

84. P. Holtappels, F. W. Poulsen, M. Mogensen, *Solid State Ionics* **135**, 675–679 (2000).
85. N. Dai, J. Feng, Z. Wang, T. Jiang, W. Sun, J. Qiao, K. Sun, *Journal of Materials Chemistry A* **1**, 14147–14153 (2013).
86. a Chang, S. Skinner, J. Kilner, *Solid State Ionics* **177**, 2009–2011 (2006).
87. G. Kim, S. Wang, a. J. Jacobson, L. Reimus, P. Brodersen, C. a. Mims, *Journal of Materials Chemistry* **17**, 2500 (2007).
88. Y. Li, J. Cheng, J. Song, J. A. J. A. Alonso, M. T. Ferna, J. B. Goodenough, M. T. Fernández-Díaz, *Chemistry of Materials* **24**, 4114–4122 (2012).
89. G. Amow, I. J. Davidson, S. J. Skinner, *Solid State Ionics* **177**, 1205–1210 (2006).
90. P. Popper, S. N. Ruddlesden, *Transactions of the British Ceramic Society* **62**, 443–449 (1963).
91. B. Raveau, M. Hervieu, D. Pelloquin, C. Michel, R. Retoux, *Zeitschrift für anorganische und allgemeine Chemie* **631**, 1831–1839 (2005).
92. R. Chiba, F. Yoshimura, Y. Sakurai, *Solid State Ionics* **152-153**, 575–582 (2002).
93. H. Falcón, A. E. Goeta, G. Punte, R. E. Carbonio, *Journal of Solid State Chemistry* **133**, 379–385 (1997).
94. E. Konyshева, J. T. S. Irvine, *Journal of Materials Chemistry* **18**, 5147 (2008).
95. Z. Shao, S. M. Haile, *Nature* **431**, 170–3 (2004).
96. Z. Z. Shao, W. W. Yang, Y. Cong, H. Dong, J. Tong, G. Xiong, *Journal of Membrane Science* **172**, 177–188 (2000).
97. S. McIntosh, J. F. Vente, W. G. Haije, D. H. A. Blank, H. J. M. Bouwmeester, *Chemistry of Materials* **18**, 2187–2193 (2006).
98. M. L. McCartney, *Journal of the American Ceramic Society* **70**, 54–58 (1987).
99. S. P. S. Badwal, J. Drennan, *Journal of Materials Science* **22**, 3231–3239 (1987).
100. T. Ishihara, H. Matsuda, Y. Takita, *Journal of the American Chemical Society* **116**, 3801–3803 (1994).
101. P. R. Slater, J. T. S. Irvine, T. Ishihara, Y. Takita, *Solid State Ionics* **107**, 319–323 (1998).
102. T. Ishihara, H. Furutani, T. Yamada, Y. Takita, *Ionics* **3**, 209–213 (1997).

103. X. Zhang, S. Ohara, R. Maric, H. Okawa, *Solid State Ionics* **133**, 153–160 (2000).
104. R. Cook, R. MacDuff, A. Sammells, *Journal of the Electrochemical Society* **137**, 3309–3310 (1990).
105. X. Tan, W. Yin, B. Meng, X. Meng, N. Yang, Z. Ma, *Science in China Series B: Chemistry* **51**, 808–812 (2008).
106. T. Jardiel, B. Levenfeld, R. Jiménez, A. Várez, *Ceramics International* **35**, 2329–2335 (2009).
107. Y. Du, N. M. Sammes, *Journal of Power Sources* **136**, 66–71 (2004).
108. S. P. S. Badwal, F. T. Ciacchi, S. Rajendran, J. Drennan, *Solid State Ionics* **109**, 167–186 (1998).
109. T. Suzuki, M. H. Zahir, T. Yamaguchi, Y. Fujishiro, M. Awano, N. Sammes, *Journal of Power Sources* **195**, 7825–7828 (2010).
110. N. Drousiotis, M. H. D. Othman, U. Doraswami, Z. Wu, G. Kelsall, K. Li, *Electrochemistry Communications* **11**, 1799–1802 (2009).
111. X. . Chen, K. . Khor, S. . Chan, L. . Yu, *Materials Science and Engineering: A* **335**, 246–252 (2002).
112. Q. Zhu, B. Fan, *Solid State Ionics* **176**, 889–894 (2005).
113. E. Kendrick, A. Orera, P. R. Slater, *Journal of Materials Chemistry* **19**, 7955–7958 (2009).
114. J. E. H. Sansom, D. Richings, P. R. Slater, *Solid State Ionics* **139**, 205–210 (2001).
115. J. R. Tolchard, M. S. Islam, P. R. Slater, *Journal of Materials Chemistry* **13**, 1956–1961 (2003).
116. D. Marrero-López, M. C. Martín-Sedeño, J. Peña-Martínez, J. C. Ruiz-Morales, P. Núñez, M. A. G. Aranda, J. R. Ramos-Barrado, *Journal of Power Sources* **195**, 2496–2506 (2010).
117. P. Lacorre, F. Goutenoire, O. Bohnke, *Nature* **404**, 9–11 (2000).
118. S. Georges, O. Bohnké, F. Goutenoire, Y. Laligant, J. Fouletier, P. Lacorre, *Solid State Ionics* **177**, 1715–1720 (2006).
119. M. P. Pechini, US Patent 3.330.697, US Patent, 1967.
120. C. J. Brinker, G. W. Scherer, *Sol-Gel Science: The Physics and Chemistry of Sol-Gel Processing*, Academic Press, Inc., 1990, p. 908.

121. G. Frenzer, W. F. Maier, *Annual Review of Materials Research* **36**, 281–331 (2006).
122. H. M. Rietveld, *Journal of Applied Crystallography* **2**, 65–71 (1969).
123. A. C. Larson, R. B. Von Dreele, *Los Alamos National Laboratory Report LAUR* **86** (2000).
124. B. Toby, *Journal of Applied Crystallography* **34**, 210–213 (2001).
125. P. Zoller, John Wiley & Sons, Inc., 2002.
126. C. Hancock, Anion Substitution in Perovskite Related Materials for Fuel Cell Applications, University of Birmingham (2013).
127. D. Johnson, ZView: a Software Program for IES Analysis, Version 2.8, Scribner Associates, Inc. Southern Pines, NC, 2008.
128. J. Kiiarsepp, H. Reshetnyak, H. Annuka, J. Kübarsepp, *International Journal of Refractory Metals and Hard Metals* **12**, 341–348 (1994).
129. S. Lee, J.-M. Kim, H. S. Hong, S.-K. Woo, *Journal of Alloys and Compounds* **467**, 614–621 (2009).
130. H. S. Hong, U.-S. Chae, S.-T. Choo, *Journal of Alloys and Compounds* **449**, 331–334 (2008).
131. J. J. Benbow, J. Bridgwater, Paste Flow and Extrusion, Clarendon Press, 1993.
132. N. Bailly, S. Georges, E. Djurado, *Solid State Ionics* **222-223**, 1–7 (2012).
133. M. J. Jørgensen, M. Mogensen, *Journal of The Electrochemical Society* **148**, A433–A442 (2001).
134. A. Martínez-Amesti, A. Larrañaga, L. M. Rodríguez-Martínez, A. T. Aguayo, J. L. Pizarro, M. L. N6, A. Laresgoiti, M. I. Arriortua, *Journal of Power Sources* **185**, 401–410 (2008).
135. P. Blennow, K. K. Hansen, L. R. Wallenberg, M. Mogensen, *Solid State Ionics* **180**, 63–70 (2009).
136. D. Stolten, B. Emonts, Fuel Cell Science and Engineering, Stolten, Emonts, Editors Wiley-VCH Verlag GmbH & Co. KGaA, Weinheim, Germany, 2012; <http://doi.wiley.com/10.1002/9783527650248>.
137. M. Suzuki, H. Sasaki, S. Ootoshi, A. Kajimura, M. Ippommatsu, *Solid State Ionics* **62**, 125–130 (1993).

138. W. Zhou, Z. L. Wang, *Scanning microscopy for nanotechnology: techniques and applications*, Springer, 2006.
139. K. Kendall, M. Palin, *Journal of Power Sources* **71**, 268–270 (1998).
140. N. M. Sammes, Y. Du, R. Bove, *Journal of Power Sources* **145**, 428–434 (2005).
141. M. D. Gross, J. M. Vohs, R. J. Gorte, *Electrochimica Acta* **52**, 1951–1957 (2007).
142. Y. Du, N. M. Sammes, G. A. Tompsett, *Journal of the European Ceramic Society* **20**, 959–965 (2000).
143. T. Suzuki, T. Yamaguchi, Y. Fujishiro, M. Awano, *Journal of Power Sources* **160**, 73–77 (2006).
144. K. S. Howe, E. R. Clark, J. Bowen, K. Kendall, *International Journal of Hydrogen Energy* **38**, 1731–1736 (2013).
145. C. Mallon, K. Kendall, *Journal of Power Sources* **145**, 154–160 (2005).
146. J. T. S. Irvine, P. R. Slater, P. A. Wright, *Ionics* **2**, 213–216 (1996).
147. Y.-H. Huang, R. I. Dass, J. C. Denyszyn, J. B. Goodenough, *Journal of The Electrochemical Society* **153**, A1266–A1272 (2006).
148. J. C. Ruiz-Morales, J. Canales-Vázquez, C. Savaniu, D. Marrero-López, W. Zhou, J. T. S. Irvine, *Nature* **439**, 568–71 (2006).
149. J. Yoo, A. Verma, S. Wang, A. J. Jacobson, *Journal of the Electrochemical Society* **152**, A497 (2005).
150. Y. Niu, W. Zhou, J. Sunarso, L. Ge, Z. Zhu, Z. Shao, *Journal of Materials Chemistry* **20**, 9619 (2010).
151. A. Evdou, V. Zaspalis, L. Nalbandian, *Fuel* **89**, 1265–1273 (2010).
152. M. Hervieu, C. Michel, D. Pelloquin, a. Maignan, B. Raveau, *Journal of Solid State Chemistry* **149**, 226–235 (2000).
153. S. Ayyappan, V. Menivannan, G. N. Subbanna, C. N. R. Rao, *Solid State Communications* **87**, 551–552 (1993).
154. P. R. R. Slater, C. Greaves, *Physica C: Superconductivity* **223**, 37–45 (1994).
155. J. P. Hodges, S. Short, J. D. Jorgensen, X. Xiong, B. Dabrowski, S. M. Mini, C. W. Kimball, *Journal of Solid State Chemistry* **151**, 190–209 (2000).

156. V. V. Vashuk, L. V. Kokhanovskii, I. I. Yushkevich, *Inorganic Materials* **36**, 79–83 (2000).
157. M. V Patrakeevev, I. A. Leonidov, V. L. Kozhevnikov, V. V Kharton, *Solid State Sciences* **6**, 907–913 (2004).
158. V. Damljanović, C. Ulrich, C. Bernhard, B. Keimer, P. Mandal, A. Krimmel, A. Loidl, *Physical Review B* **73**, 172502 (2006).
159. M. Schmidt, S. J. Campbell, *Journal of Solid State Chemistry* **156**, 292–304 (2001).
160. A. Orera, P. R. Slater, *Chemistry of Materials* **22**, 675–690 (2010).
161. A. J. Jacobson, *Chemistry of Materials* **22**, 660–674 (2010).
162. D. Kuščer, D. Hanzel, *Journal of the American Ceramic Society* **54**, 1148–1154 (2001).
163. C. Greaves, P. Slater, *Journal of Materials Chemistry* **800**, 17–21 (1991).
164. C. Greaves, P. R. Slater, *Physica C: Superconductivity* **175**, 172–178 (1991).
165. Y. Miyazaki, H. Yamane, N. Ohnishi, T. Kajitani, K. Hiraga, Y. Morii, S. Funahashi, T. Hirai, *Physica C: Superconductivity* **198**, 7–13 (1992).
166. A. Maignan, M. Hervieu, C. Michel, B. Raveau, *Physica C: Superconductivity* **208**, 116–120 (1993).
167. D. Pelloquin, M. Hervieu, C. Michel, N. Nguyen, B. Raveau, *Journal of Solid State Chemistry* **134**, 395–408 (1997).
168. C. C. Appel, N. Bonanos, *Journal of the European Ceramic Society* **19**, 847–851 (1999).
169. M. Aoki, Y.-M. Chiang, I. Kosacki, L. J.-R. Lee, H. Tuller, Y. Liu, *Journal of the American Ceramic Society* **79**, 1169–1180 (1996).
170. C. A. Hancock, P. R. Slater, *Dalton transactions* **40**, 5599–603 (2011).
171. J. M. Porrás-Vázquez, T. Pike, C. A. Hancock, J. F. Marco, F. J. Berry, P. R. Slater, *Journal of Materials Chemistry A* **3**, 11834–11841 (2013).
172. Multistat Software, Version 1.5, Scribner Associates, Inc. Southern Pines, NC, .
173. J. M. Porrás-Vázquez, E. R. Losilla, P. J. Keenan, C. a Hancock, T. F. Kemp, J. V Hanna, P. R. Slater, *Dalton transactions* **42**, 5397–405 (2013).

174. R. D. Shannon, *Acta Crystallographica Section A: Crystal Physics* **32**, 751–767 (1976).
175. M. V. Patrakeev, V. V. Kharton, Y. A. Bakhteeva, A. L. Shaula, I. a. Leonidov, V. L. Kozhevnikov, E. N. Naumovich, A. a. Yaremchenko, F. M. B. Marques, *Solid State Sciences* **8**, 476–487 (2006).
176. G. Xiao, Q. Liu, S. Wang, V. G. Komvokis, M. D. Amiridis, A. Heyden, S. Ma, F. Chen, *Journal of Power Sources* **202**, 63–69 (2012).
177. J. Feng, G. Yang, N. Dai, Z. Wang, W. Sun, D. Rooney, J. Qiao, K. Sun, *J. Mater. Chem. A* **2**, 17628–17634 (2014).
178. W. Kobsiriphat, B. D. Madsen, Y. Wang, M. Shah, L. D. Marks, S. A. Barnett, *Journal of The Electrochemical Society* **157**, B279–B284 (2010).
179. V. V. Kharton, E. V. Tsipis, A. a. Yaremchenko, I. P. Marozau, A. P. Viskup, J. R. Frade, E. N. Naumovich, *Materials Science and Engineering: B* **134**, 80–88 (2006).
180. V. V. Kharton, A. A. Yaremchenko, A. L. Shaula, A. P. Viskup, F. M. B. Marques, J. R. Frade, E. N. Naumovich, J. R. Casanova, I. P. Marozau, *Defect and Diffusion Forum* **226-228**, 141–160 (2004).
181. V. V. Kharton, A. L. Shaula, F. M. M. Snijkers, J. F. C. Cooymans, J. J. Luyten, a. a. Yaremchenko, A. a. Valente, E. V. Tsipis, J. R. Frade, F. M. B. Marques, J. Rocha, *Journal of Membrane Science* **252**, 215–225 (2005).
182. D. Neagu, J. T. S. Irvine, *Chemistry of Materials* **22**, 5042–5053 (2010).
183. V. Kharton, A. Viskup, A. Kovalevsky, *Solid State Ionics* **133**, 57–65 (2000).
184. D. J. Cumming, J. A. Kilner, S. Skinner, *Journal of Materials Chemistry* **21**, 5021 (2011).
185. P. Blennow, A. Hagen, K. Hansen, L. Wallenberg, M. Mogensen, *Solid State Ionics* **179**, 2047–2058 (2008).
186. J. C. Pérez-Flores, D. Pérez-Coll, S. García-Martín, C. Ritter, G. C. Mather, J. Canales-Vázquez, M. Gálvez-Sánchez, F. García-Alvarado, U. Amador, *Chemistry of Materials* **25**, 2484–2494 (2013).
187. J. Karczewski, B. Riegel, M. Gazda, P. Jasinski, B. Kusz, *Journal of Electroceramics* **24**, 326–330 (2009).
188. W. Ito, T. Nagai, T. Sakon, *Solid State Ionics* **178**, 809–816 (2007).
189. P. Vernoux, M. Guillodo, J. Fouletier, A. Hammou, *Solid State Ionics* **135**, 425–431 (2000).

190. N. Danilovic, J.-L. Luo, K. T. Chuang, A. R. Sanger, *Journal of Power Sources* **194**, 252–262 (2009).
191. O. Yamamoto, Y. Takeda, R. Kanno, M. Noda, *Solid State Ionics* **22**, 241–246 (1987).
192. K. R. Kendall, C. Navas, J. K. Thomas, H.-C. zur Loye, *Solid State Ionics* **82**, 215–223 (1995).
193. J. Canales-Vázquez, S. W. Tao, J. T. S. Irvine, *Solid State Ionics* **159**, 159–165 (2003).
194. J. Karczewski, B. Riegel, S. Molin, a. Winiarski, M. Gazda, P. Jasinski, L. Murawski, B. Kusz, *Journal of Alloys and Compounds* **473**, 496–499 (2009).
195. E. Kendrick, M. Islam, P. Slater, *Solid State Ionics* **176**, 2975–2978 (2005).
196. F. Bidrawn, G. Kim, N. Aramrueang, J. M. Vohs, R. J. Gorte, *Journal of Power Sources* **195**, 720–728 (2010).
197. a Ovalle, J. Ruizmorales, J. Canalesvazquez, D. Marrerolopez, J. Irvine, *Solid State Ionics* **177**, 1997–2003 (2006).
198. M. J. Escudero, J. T. S. Irvine, L. Daza, *Journal of Power Sources* **192**, 43–50 (2009).
199. Q. X. Fu, F. Tietz, D. Stöver, *Journal of The Electrochemical Society* **153**, D74–D83 (2006).
200. J. C. Ruiz-Morales, J. Canales-Vázquez, C. Savaniu, D. Marrero-López, P. Núñez, W. Zhou, J. T. S. Irvine, *Physical Chemistry Chemical Physics* **9**, 1821–1830 (2007).
201. J. Rodriguez-Carvajal, M. Hennion, *Physical Review B* **57**, 3189–3192 (1998).
202. T. W. Pike, P. R. Slater, *International Journal of Low-Carbon Technologies* **7**, 60–62 (2011).
203. S. Husain, R. J. Choudhary, R. Kumar, **58**, 1045–1049 (2002).
204. Y. Guo, X. Zhang, R. Wappling, R. Wäppling, *Journal of Alloys and Compounds* **306**, 133–140 (2000).
205. M. Kestigian, R. Ward, *Journal of the American Chemical Society* **76**, 6027 (1954).
206. K. Fujino, S. Sasaki, Y. Takéuchi, R. Sadanaga, *Acta Crystallographica Section B* **37**, 513–518 (1981).

207. A. A. Markov, I. A. Leonidov, M. V. Patrakeev, V. L. Kozhevnikov, O. A. Savinskaya, U. V. Ancharova, A. P. Nemudry, *Solid State Ionics* **179**, 1050–1053 (2008).
208. J. F. Shin, P. R. Slater, *Journal of Power Sources* **196**, 8539–8543 (2011).